Distributed Entrainment Sink Approach (DESA) - a New Method for Modelling Mixing and Transport in the Intermediate Field

by

K. W. Choi

Joseph H.W. Lee

Report No.: CEHL-R07-01

Croucher Laboratory of Environmental Hydraulics
Department of Civil Engineering
The University of Hong Kong

October 2007

Contents

List of Figures

List of Tables

Chapter 1

Introduction

For environmental risk assessment it is necessary to predict the impact of effluent discharges for a wide range of discharge and ambient conditions. For many densely populated coastal cities in Asian Pacific countries, this prediction poses particular technical challenges. The effluent discharges are often located in relatively shallow waters of 5 - 20 m depth, not far (e.g. 5-10 km) from sensitive receivers such as beaches and fisheries. Sound management decisions on the appropriate degree of treatment must be based on impact assessment models that can cater for both the near field and intermediate/far field.

In the vicinity of the discharge ("near field"), the buoyant jet trajectory and mixing can be well-predicted by a validated integral model that predicts the turbulent entrainment as a function of source characteristics, ambient velocity and stratification (Fig. 1.1). Near field models can resolve down to scales of the order of the jet diameter; typical time and length scales of the plume rise are in the order of minutes and water depths respectively. On the other hand, in the "far field", the effluent is passively transported by ambient currents and further diluted by turbulent diffusion; typical time and length scales are in the order of hours and kilometres. In the near-far field transition ("intermediate field"), the dynamics depends on the interaction of the near field plume mixing and the ambient flow, which can result in changes in background concentration, gravitational spreading, and modifications in ambient stratification.

The large disparity of time and length scales in the near and far fields is well known, and effluent mixing and transport beyond the near field has been explored in several studies. As an extreme case, the effluent buoyant jet is modelled as a freshwater source in a single grid cell in the far field model (Blumberg *et al.* 1996). The plume trap height and dilution is computed as a function of ambient velocity and density profile derived from the far field model. Zhang and Adams (1999) studied near-far field coupling by employing the 3D circulation model ECOMsi and the near field model RSB. Four methods for interfacing the near and far field models were considered: 1) introduce the discharge flow and pollution load (tracer mass flux) as source terms at the discharge point; 2) introduce source flow at discharge point, and release the pollution load at the trap height predicted by RSB; 3) introduce both the diluted flow and the pollution load at the predicted trap height; and 4) only introduce the pollution load at the predicted trap height. Among these four methods, the last one is the most commonly adopted approach in practice. As the near field model RSB provides only a predicted plume trap height, dilution and width for each ambient condition, the interaction of the near field mixing with the ambient flow cannot be accounted for by this approach. In addition, the correct re-production of plume trap height and dilution is dependent on grid resolution, and the parameterization of the horizontal and vertical diffusivities (Zhang and Adams 1999). More important, these near-far field

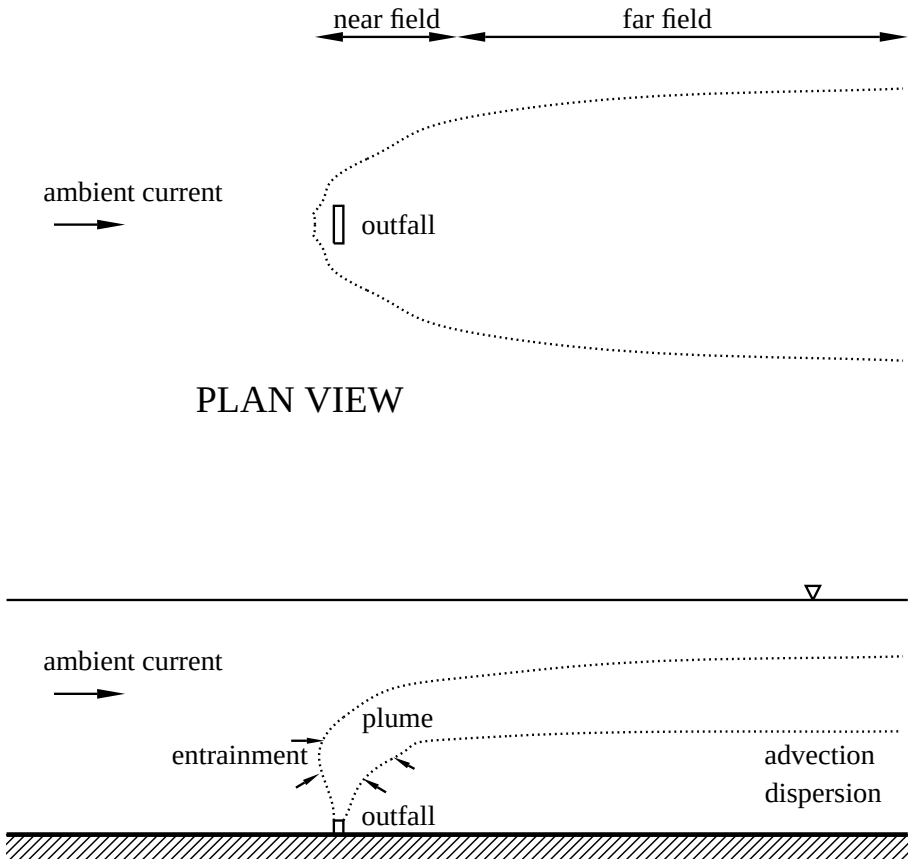

Figure 1.1: Mixing and transport of coastal outfall discharge.

coupling methods have not been validated against basic laboratory experimental data.

Kim *et al.* (2002) coupled a jet integral model with a particle tracking model to simulate the mixing of a single buoyant jet discharge. Far field mixing and transport are simulated by particles introduced at the equilibrium rise height or the end of the computed initial mixing zone. The model results were compared with laboratory experiments for a non-stratified crossflow. The flow field or velocity distribution was not generated by 3D flow model, but interpolated from the integral jet model predictions. Although the two models are linked, there is negligible dynamic interaction between them. More recently, Bleninger and Jirka (2004) proposed a methodology to couple the near-field CORMIX model and the Delft3D circulation model. An approach similar to Method 3 of Zhang and Adams (1999) is adopted, whereby the discharge volume and mass fluxes at the terminal height computed by CORMIX are incorporated into the far field model.

All of the above methods involve either "one-way coupling" or weakly "two-way coupling"; hence the dynamic effects of the plume mixing are not satisfactorily represented in the far field model. The interpretation of experimental data is also hampered by the lack of a general robust numerical prediction method for mixing in the intermediate field. For example, outfall diffuser design is often based on semi-empirical correlations of laboratory data of plane buoyant jets in linearly stratified fluid (Wallace and Wright 1984; Lee and Cheung 1986; Jirka and Lee 1994). Nevertheless, as the ambient stratification in the finite laboratory flume undergoes continuous modification by the introduction of the jet discharge, the effect of the limited flume length

and changing ambient density on the results has yet to be clarified. Further, near field plume models are valid only up to the base of the spreading layer. In many situations, a theoretical prediction of initial dilution necessitates a meaningful coupling of the vertical plume rise region with the horizontal buoyant spreading layer in the intermediate field. For example, Koh (1983) used an analytical model to show the upper layer thickness of a line plume in stagnant uniform fluid to be about 30 percent of the depth.

In this report, we present a general Distributed Entrainment Sink Approach (DESA) for the effective modelling of mixing and transport in the intermediate field. In Chapter 2, the general methodology of DESA is described. The details on how the near field mixing can be satisfactorily represented in the far field model (EFDC) by embedding the near field predictions by a Lagrangian plume model (JETLAG) at "grid cell" level is presented. Alternative coupling approaches based on "Source-only" methods are also discussed.

To demonstrate the applicability and accuracy of DESA for different effluent discharges, the numerical model predictions are compared with experimental data in representative laboratory experiments of prototype environmental transport problems. In Chapter 3, different types of 3D round jets discharged into various stagnant environment (uniform or stratified) are examined. In Chapter 4, 2D plane buoyant jets are considered to show the flexibility of the present coupling approach. We then study various discharges (line plume, round jet and inclined dense jet) in cross current in Chapter 5. In Chapter 6, various issues on the numerical implementation of DESA including the model grid discretization, source representation and time step requirement are discussed.

Chapter 2

Methodology

2.1 Coupling of near and far field model

In the intermediate field, the dynamics depends on the interaction of the near field plume mixing and the ambient flow, which can result in changes in background concentration, gravitational spreading, and modifications in ambient stratification. These phenomena have been observed in laboratory studies (e.g. Baines and Turner 1969; Wallace and Wright 1984; Lee and Cheung 1986; Wong 1986; Roberts 1979), but the interpretation of laboratory experimental data is hampered by the lack of a general robust numerical prediction method for mixing and transport in the intermediate field. For example, outfall diffuser design is often based on semi-empirical correlations of laboratory data of plane buoyant jets in linearly stratified fluid (Wallace and Wright 1984; Lee and Cheung 1986; Jirka and Lee 1994). Nevertheless, as the ambient stratification in the finite laboratory flume undergoes continuous modification by the introduction of the jet discharge, it is not clear whether these empirical correlations can be directly extrapolated to prototype scale.

All the previous approaches of near-far field coupling provide essentially either "one-way coupling" or weakly "two-way coupling"; hence the dynamic effects of the plume mixing or active mixing are not satisfactorily represented in the far field model. From the viewpoint of the surrounding water, the important near field flows are the bulk sink flows ("loss") due to the turbulent jet entrainment and the bulk source flows ("gain") due to the diluted discharges. In order to have a true two-way coupling, it is proposed to represent the discharge by introducing in the far field model: (i) a series of entrainment sinks along the predicted plume trajectory; and (ii) the diluted flow and pollution loading at the predicted terminal level of plume rise. The sources and sinks are determined from a near field model embedded within the far field model. The key difference between this new method (Distributed Entrainment Sink Approach, DESA) and the commonly employed "source only" methods is that the near field mixing is fully resolved by the sub-grid plume model; the bulk fluid and tracer mass transport induced by the effluent discharge as well as the influence of background concentrations or recirculation on the near field can be fully modelled in a dynamic manner. It ensures mass conservation in the system and models the interaction of plume entrainment and ambient flow in a way similar to the "filling box" mechanism described by Turner (1973). The diluted flow, which is usually at least 1-2 orders of magnitude greater than the discharge flow, and mass sources fill up the spreading layer at the terminal level, while the entrainment sinks draw the ambient fluids back into the plume. This interaction of the plume and the surrounding flow induces additional mixing beyond the near field. The effect of unsteady evolution of the ambient flow on the plume trajectory and dilution, as well as the changes in plume mixing on the ambient flow are fully accounted for.

In the following, we present a general Distributed Entrainment Sink Approach (DESA) for the effective modelling of mixing and transport in the intermediate field. The near field mixing is modelled by a Lagrangian plume model (JETLAG, Lee and Cheung 1990; Lee and Chu 2003), while the far field transport is simulated by the Environmental Fluid Dynamics Code (EFDC, Hamrick 1992). It is shown that the near field mixing can be satisfactorily represented in the far field model by embedding the near field predictions at "grid cell" level. The accuracy of the method is demonstrated by comparing the numerical model predictions with experimental data in representative laboratory experiments of prototype environmental transport problems.

2.2 Previous coupling by "Source only" methods

Before given the details of DESA, we would like to describe the alternative "source only" methods that can be used for coupling the effluent discharges into the far field models. They will be also considered when assessing the performance of DESA method. Those methods include:

a) Undiluted source introduced at discharge point (Actual Source (AS)): it is similar to the commonly used approach in engineering practice when only the far field model is used. Unlike some common practices where only the pollutant sources are included, both the volumetric and mass source terms are introduced at the discharge point in the continuity and mass transport equations (Fig. 2.1a);

b) Diluted source and mass source terms introduced at the terminal level determined by the embedded near field model (Diluted Source at Trapped Level (DSTL)): This method (approach 3 in Zhang and Adams 1999) does not account for the entrainment action on the far field flow. The near field model is driven by the updated ambient conditions from the far field model, while the location and strength of the source terms in the far field model are updated by the near field model (Fig. 2.1b). There is no reported work that employed this method; and

c) Undiluted source introduced at the location determined by the embedded near field model (Undiluted Source at Trapped Level (USTL)): It is similar to DSTL except that the undiluted source is applied to ensure exact water mass conservation (Fig. 2.1c).

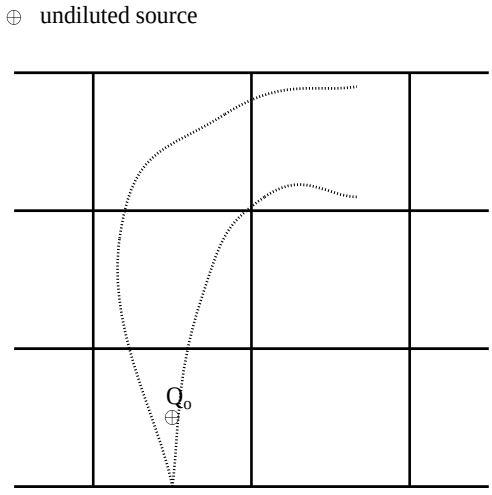

a) Actual Source (AS)

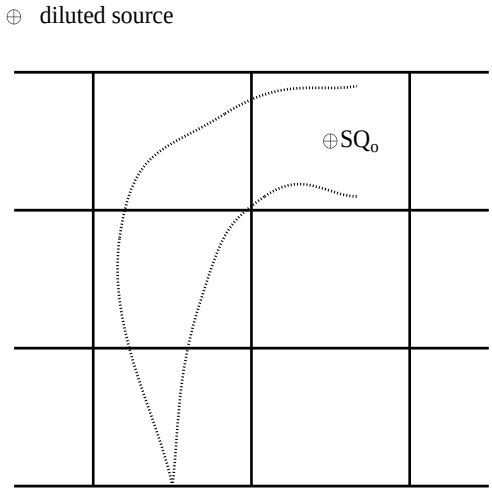

b) Diluted Source at Trapped Level (DSTL)

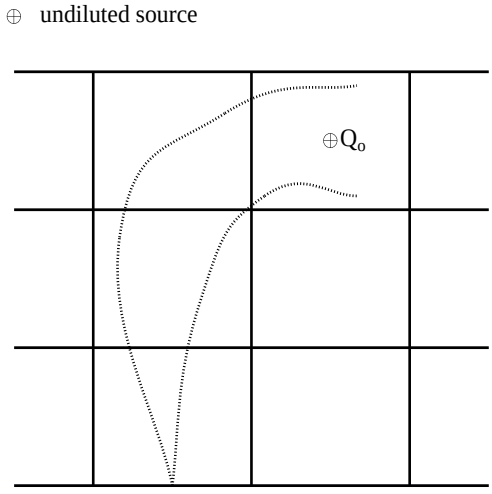

c) Undiluted Source at Trapped Level (USTL)

Figure 2.1: Alternative representation of near field mixing by "source-only" methods (S = average dilution).

2.3 Near field mixing

In our study, the Lagrangian model JETLAG (Lee and Cheung 1990, Lee and Chu 2003) is employed for plume modelling in the near field. JETLAG is a well-proven robust jet model that predicts the mixing of an arbitrarily-inclined round buoyant jet in a stratified crossflow, with a three-dimensional trajectory. It tracks the evolution of the average properties of a plume element by conservation of horizontal and vertical momentum, conservation of mass accounting for shear and vortex entrainment, and conservation of solute or tracer mass/heat. For a given set of ambient conditions (vertical profile of horizontal velocity, density, and tracer concentration), the jet trajectory, jet velocity and radius, and dilution (entrainment) can be predicted. The turbulent entrainment along the jet trajectory can then be obtained from the discharge point up to a terminal level (free surface, bottom, or trap level in the presence of ambient density stratification). The boundary conditions for the near field model depend on the far field flow, which can be obtained from a 3D circulation model.

The effect of the near field mixing on the far field flow can then be represented as follows (Fig. 2.2). The plume mixing is represented as a series of distributed sinks along the jet trajectory. Also, a source term representing the diluted flow and the discharged pollution loading (tracer mass flux) is introduced at the terminal level. These volumetric and mass source/sinks are introduced into the governing transport equations for the 3D far field model (see later discussion). We have the continuity equation as:

$$\frac{\partial U}{\partial x} + \frac{\partial V}{\partial y} + \frac{\partial W}{\partial z} = Q_s \tag{2.1}$$

and the solute mass transport equation (for both salinity and tracer) as

$$\frac{\partial (HC)}{\partial t} + \mathbf{V} \cdot \nabla (HC) = \frac{\partial}{\partial x}\left[A_H H \frac{\partial C}{\partial x}\right] + \frac{\partial}{\partial y}\left[A_H H \frac{\partial C}{\partial y}\right] + \frac{\partial}{\partial z}\left[K_H H \frac{\partial C}{\partial z}\right] + Q_c \tag{2.2}$$

where U, V and W are the turbulent-mean velocity components in the x, y, z-directions respectively;

$$\mathbf{V} \cdot \nabla (\quad) \equiv U \frac{\partial (\quad)}{\partial x} + V \frac{\partial (\quad)}{\partial y} + W \frac{\partial (\quad)}{\partial z};$$

H = water depth; C = solute concentration; A_H is the horizontal eddy diffusivity, K_H is the vertical eddy diffusivity, Q_s is the volumetric source/sink term representing the entrainment or diluted flows and Q_c is the source/sink term for the solute or tracer mass. Both of these terms can be obtained at "grid cell" level from the near field model.

As the ambient conditions provided by the far field model (vertical profile of upstream velocity, solute concentration and density) change, the near field plume behaviour changes correspondingly. The changes in jet trajectory and dilution will be reflected in the positions and strengths of the sources and sinks.

2.4 Far field transport

In the present study, the 3D flow model is based on the Environmental Fluid Dynamics Code (EFDC) for solving free surface flow and transport problems (Hamrick 1992). EFDC is a finite

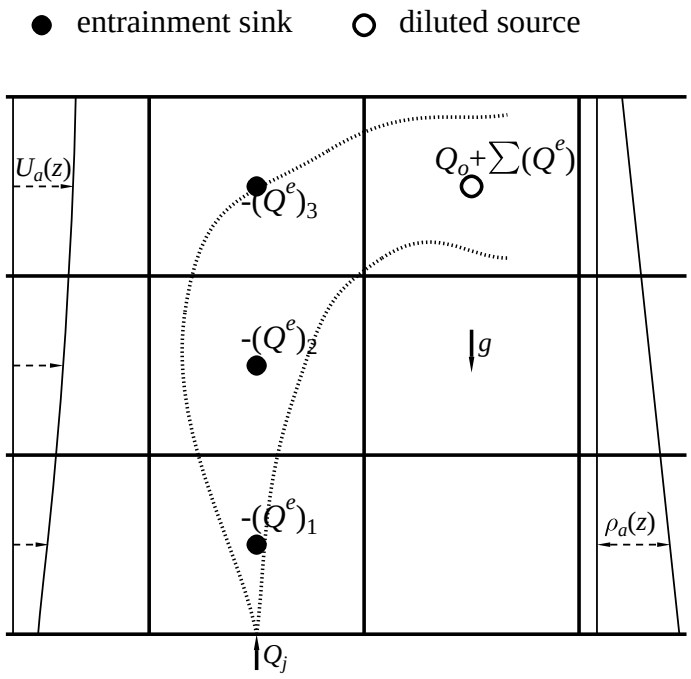

Figure 2.2: Representation of plume mixing by diluted source flow and entrainment sinks along the jet trajectory (DESA).

difference model that solves the shallow water equations using the Mellor and Yamada (1982) scheme for turbulent closure. The system of governing equations including the continuity, momentum and transport equations provides a closed system for the variables U, V, W, P, η, ρ, S and T, where ρ = fluid density, S = salinity, T = temperature and η is the free surface level above a reference datum. The pressure P is assumed to be hydrostatic and consists of barotropic (induced by external free surface gravity) and baroclinic (induced by the horizontal density gradient) components. The model uses a staggered grid for discretization and a sigma grid co-ordinate in vertical direction. The modal splitting technique is used to solve the discretized equations.

The horizontal turbulent diffusivity is given by:

$$A_H = C\Delta x\Delta y\sqrt{\left(\frac{\partial U}{\partial x}\right)^2 + \frac{1}{2}\left(\frac{\partial V}{\partial x}+\frac{\partial U}{\partial y}\right)^2 + \left(\frac{\partial V}{\partial y}\right)^2} \tag{2.3}$$

where C = Smagorinsky coefficient has a value in the range of C = 0.1 - 0.2. For all the test cases considered in this report, $C = 0.17$ is adopted except where specified otherwise.

Based on the second moment turbulence closure model developed by Mellor and Yamada (1982), the vertical turbulent viscosity and diffusivity can be related to the turbulent kinetic energy, $q^2/2$, a turbulence length scale, l, and a "turbulent" Richardson number

$$R_q = -\frac{gl^2}{q^2}\left(\frac{1}{\rho_o}\frac{\partial \rho}{\partial z}\right).$$

$q^2/2$ and l are determined by a pair of transport equations; the standard turbulence model constants for the EFDC model are adopted (Hamrick 1996). They are B_1, D_1, D_2 and D_3, the traditional values are applied, i.e. 16.6, 1.8, 1.33 and 0.53 respectively.

After introducing the plume-induced source/sink terms, the governing equations of the 3D circulation model (Eq. 1.1 for fluid mass, Eq. 1.2 for each tracer mass, plus the fluid momentum and turbulent transport equations) can be solved to yield the updated flow and scalar fields. With the computed flow and solute/tracer mass distributions in the far field, the near field plume model can then be driven by the updated ambient conditions to generate the new source and sink terms for the next time step. The coupling of the models is summarized by the flow chart shown in Fig. 2.3. Any changes in one model will immediately be passed to the other model; a two-way dynamic coupling between the near and far field models is ensured.

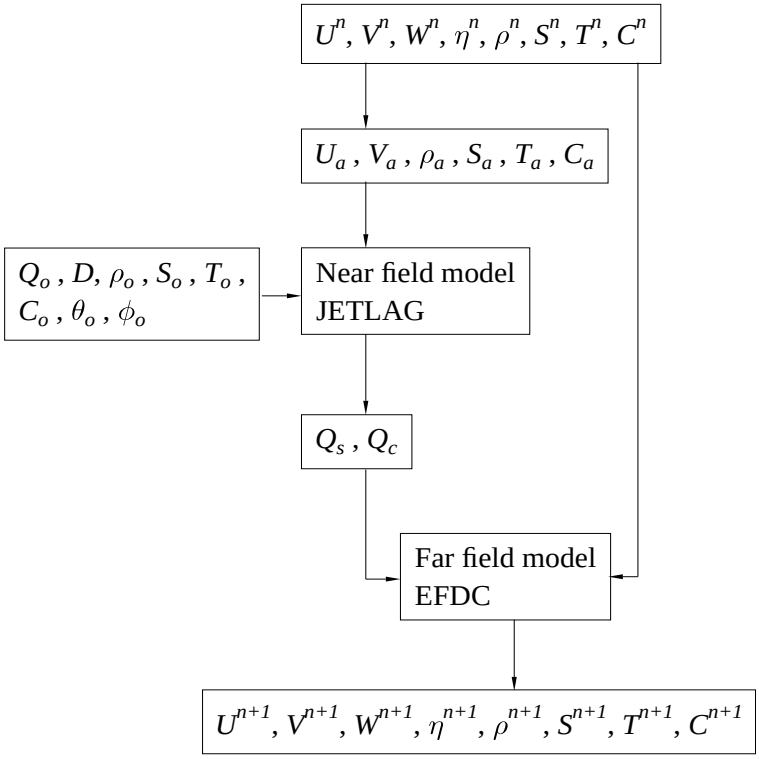

Figure 2.3: Flow chart showing the numerical implementation of the coupling between the near field and far field models.

2.5 Grid level linkage

In the Lagrangian model JETLAG, the position and average properties of a plume element is tracked (Lee and Cheung 1990, Lee and Chu 2003). The turbulent mass entrainment into a plume element, ΔM_p, consists of: (i) the shear entrainment computed as a function of the relative jet velocity in the direction of the jet axis, the radius and the thickness of the plume element, and (ii) the vortex entrainment due to the ambient crossflow, which is a function of the ambient density and velocity, the radius and the thickness of the plume element and the inclination of the plume element with respect to the ambient current (Fig. 2.4 and Fig. 2.5).

The added mass due to the entrainment flow will determine the Lagrangian evolution of the plume element geometry along the jet trajectory. In model implementation, the entrainment flow into each plume element is assigned to the corresponding far field model grid cell based on the location of the centre of the computed plume elements (Fig. 2.5 and Fig. 2.6). If the plume element is inclined and cuts through more than one vertical layers, the entrained and diluted flows are distributed into those vertical layers based on the binomial distribution around the layer containing the centre of the plume element. Fig. 2.7 shows if single source/sink term is applied instead of distributed source/sink terms, poorer computed results will be produced (see also later discussion on plane buoyant jet in stratified fluid in Chapter 4). The entrainment sink (Q_s^e) for each far field model grid cell can then be computed by summing up all the entrainment flows assigned to it, i.e.

$$Q_s = -Q_s^e = -\sum \left(\frac{\Delta M_p}{\rho_a \Delta t} \right) \tag{2.4}$$

and the corresponding tracer mass flux (Q_c^e) similarly computed as:

$$Q_c = -Q_c^e = -Q_s^e C_a \tag{2.5}$$

where ρ_a and C_a are the ambient density and solute concentration respectively, determined from the values of the eight neighbouring grid cells (Fig. 2.5).

The diluted flow and the corresponding tracer mass flux are then computed by summing the effluent and all the entrainment flows, i.e.

$$Q_s^d = Q_o + \sum Q_s^e \tag{2.6}$$

and

$$Q_c^d = Q_o C_o + \sum Q_c^e \tag{2.7}$$

where Q_o, C_o are the effluent discharge flow and tracer concentration respectively. The diluted flow is applied as a source term to the far field model grid cell that contains the centre of the plume element at the terminal level. Computing the diluted flow in this way ensures mass conservation, as the additional diluted flow is cancelled out by the negative entrainment flow. Fig. 2.8 & 2.9 show the computed plume by JETLAG, the corresponding source/sink terms and the computed horizontal velocities in the far field model grid under different ambient flow conditions. For vertical discharge into a stagnant ambient, there is only one source term in a water column. With different stopping criterion for the near-field simulation, the source term may be prescribed/assigned at different levels (Fig. 2.8). It can be seen that the induced flows in the immediate neighbourhood of the discharge are quite different for the two cases, but become quite similar at one grid cell away. If the plume trajectory is not vertical, as the diluted flow is much greater than the entrainment flow into each individual plume element, all grid cells containing the last plume element, where the diluted flow is allocated, will have a positive source term; hence there will be multiple source terms in a water column if the plume is bent-over (Fig. 2.9). The source/sink terms will interact with the ambient flow and alter the velocity distribution in the neighbourhood of the discharges.

The advantages of the proposed approach over previous "source only" methods can be summarized as follows: a) it fully accounts for the entrainment and dilution, hence the induced mixing, due to the buoyant discharge in the far field model; b) the complete 3D jet trajectory is represented instead of just a single discharge point; c) the use of the Lagrangian plume model

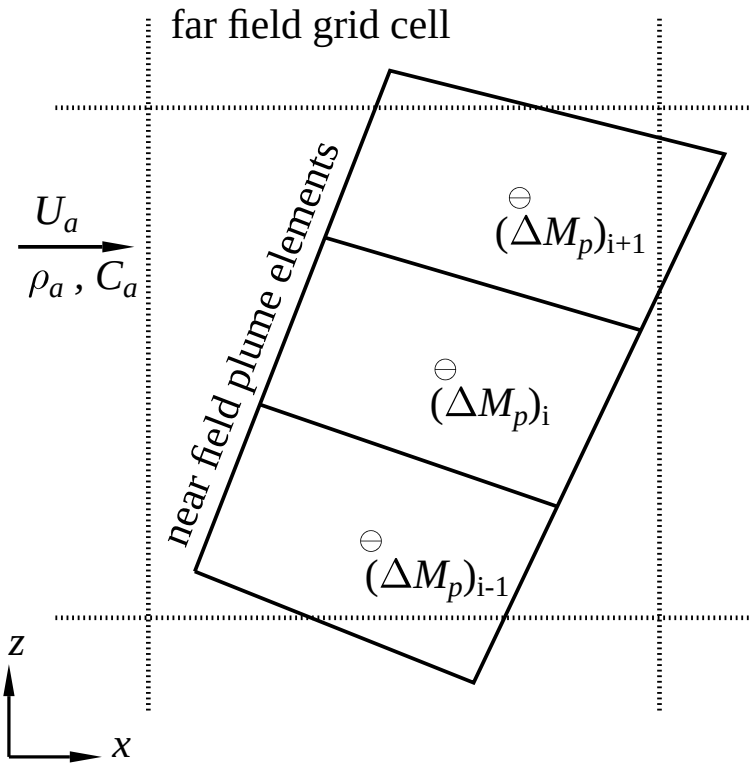

Figure 2.4: Linking near field plume elements to far field grid cell via entrainment sinks.

enables the near field simulation to be carried out independent of the far field model grid; and d) with a validated near field plume model, the DESA method can be applied to all types of buoyant discharges without the need to fine tune the far field model parameters.

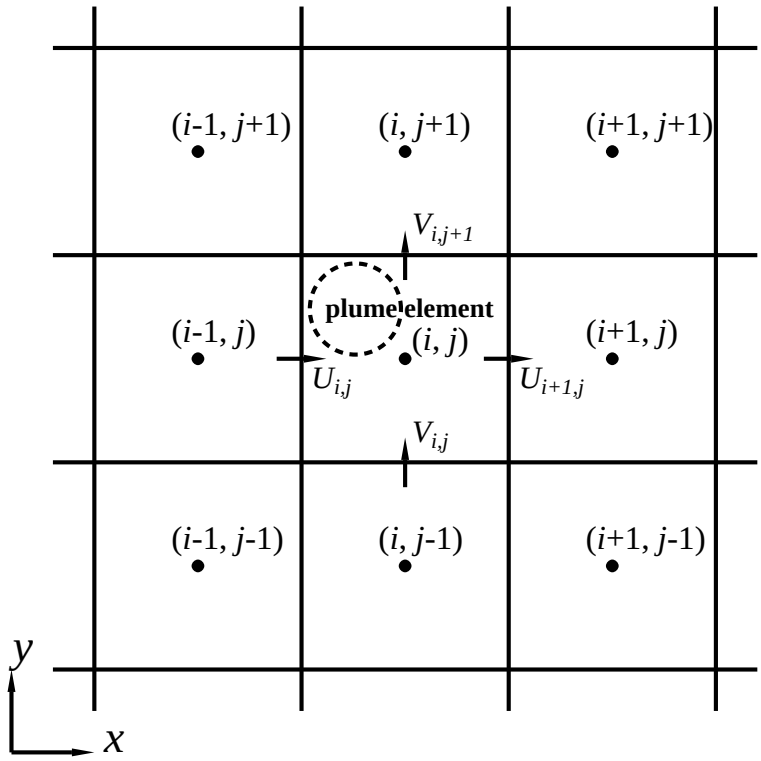

Figure 2.5: Determination of the ambient horizontal velocity and concentrations in the far field model.

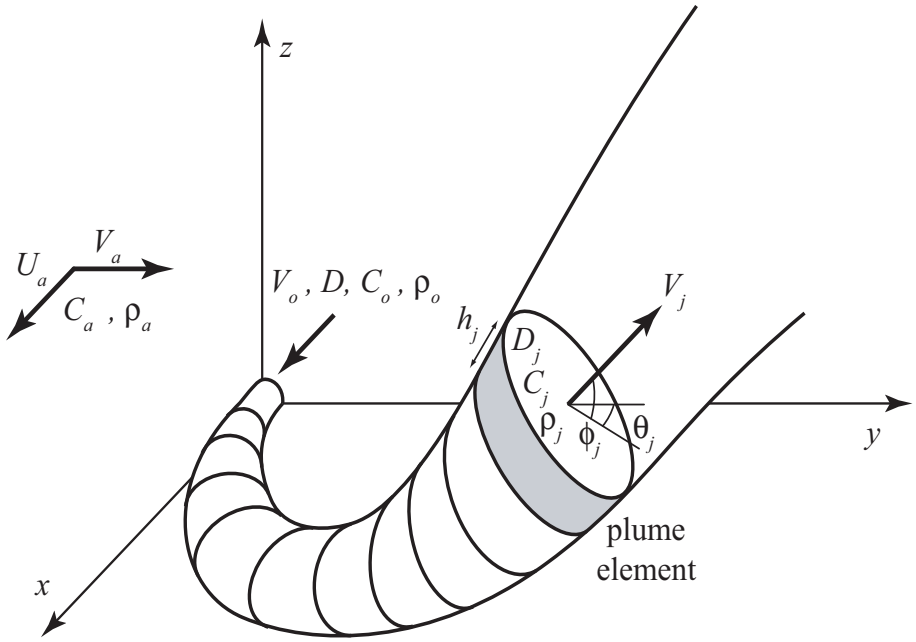

Figure 2.6: 3D jet trajectory predicted by the near field model under the influence of the ambient conditions computed in the far field model.

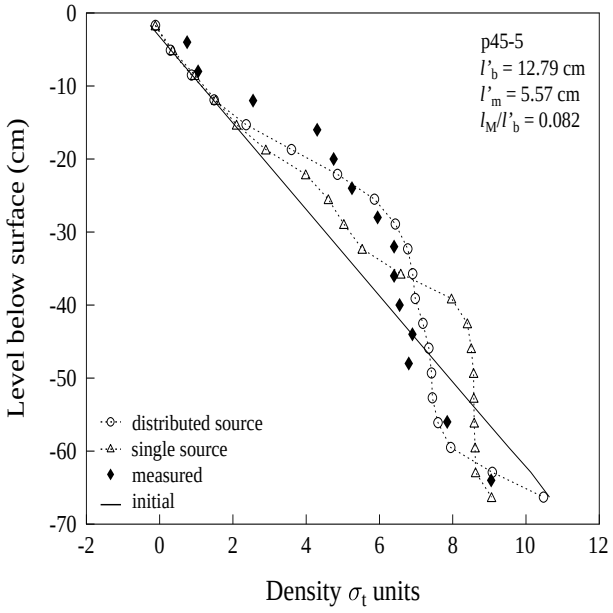

Figure 2.7: Ambient density profiles before and after a 45° "plume-like" discharge into a linearly stratified fluid.

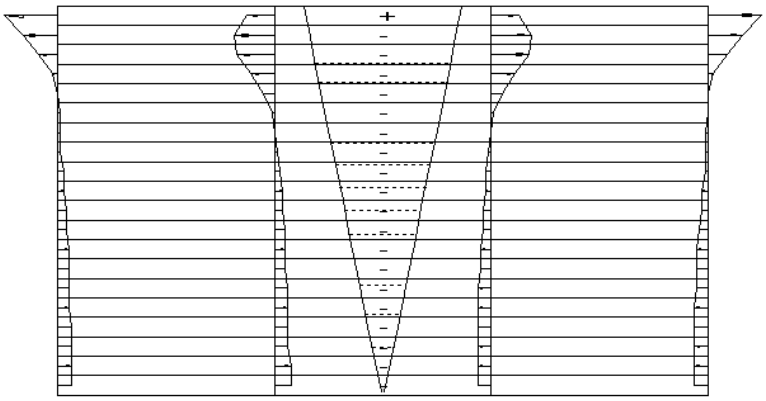

a) predicted near-field flow by DESA with source assigned at surface

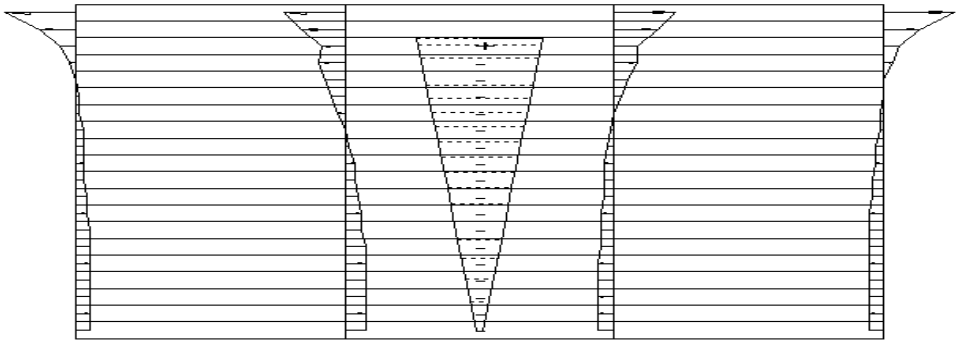

b) predicted near-field flow by DESA with source assigned at the level less than one plume radius below the surface

Figure 2.8: The computed plume and source (+) / sink (−) terms in the far field model for a vertical effluent discharge in stagnant ambient.

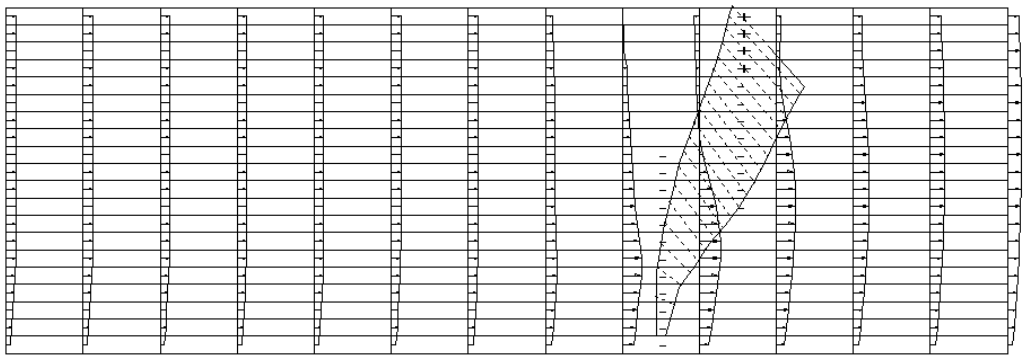

a) weak crossflow

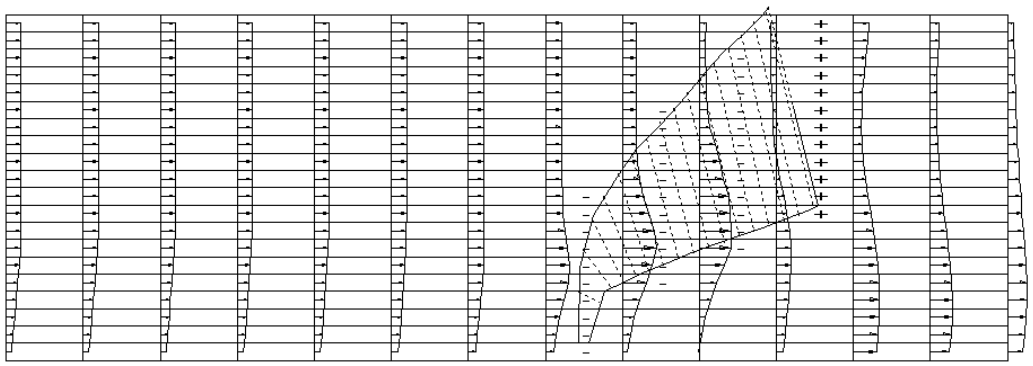

b) strong crossflow

Figure 2.9: The computed plume and source (+) / sink (−) terms in the far field model for a vertical effluent discharge in a crossflow.

Chapter 3

Round Buoyant Jet

3.1 Confined round buoyant in uniform stagnant water

Baines and Turner (1969) carried out laboratory experiments to study the effect of continuous convection from small sources of (negative) buoyancy on the properties of the environment when the region of interest is bounded. Fig. 3.1 shows a vertically sinking plume in an otherwise stagnant ambient fluid of initial uniform density ρ_a. The plume is discharged into a rectangular tank (57 cm x 45 cm in plan and 45 cm deep) and experiments have been carried out with a nozzle of diameter $D = 5$ mm placed at $H = 30$ cm or 40 cm above the bottom of the tank, with the initial level of fresh water about 0.5 cm above the discharge point. Different kinematic buoyancy flux $B_o = \frac{Q_o g \Delta\rho_o}{\rho_a(0)}$, where Q_o = discharge volume flux, were tested with an initial relative density difference $\frac{\Delta\rho_o}{\rho_a(0)} = 0.13$. The buoyant plume mixes with the ambient fluid by turbulent entrainment; when it sinks to the bottom the mixed fluid spreads sideways as a bottom layer, with negligible vertical mixing (damped by density difference). The thickness of this layer of mixed fluid increases in depth with time, and the front of this bottom layer advances with a velocity $\mathrm{d}z/\mathrm{d}t$. A 19 x 15 x 20 model grid closed at the four sides with horizontal grid size 3 cm by 3 cm and 20 uniform vertical layers and a time step $\Delta t = 0.04$ sec. (with maximum $Cr = \sqrt{gH}\Delta t/\Delta x \approx 2.66$) are used to simulate a round plume with buoyancy flux similar to those in the experiments. All simulations are cold-started.

As shown in Fig. 3.2, the model predicts ambient density profiles that change from an initially uniform concentration to a stable stratification due to the action of the plume. It is interesting to note that for $t > 12$ min, the ambient density profile is almost fixed in shape and changing at a uniform rate in time at all levels, with $d\rho/dt$ = constant - consistent with the self-similar asymptotic solution of Baines and Turner (1969). Fig. 3.3 shows that the predicted time variation of the interface by DESA method (defined by 0.1 $\Delta\rho_{max}$ contour, where $\Delta\rho_{max} = \rho_o$ - ρ), $z(t)$, is in excellent agreement with the following analytical solution (Eq. 6a of Baines and Turner (1969)) that is in excellent agreement with their experimental data:

$$\tau = 5\left(\frac{5}{18}\right)^{1/3}\left[\varsigma^{-2/3} - 1\right] \tag{2.1}$$

in which $\varsigma = \frac{z}{H}$ and $\tau = \frac{4}{\pi^{1/3}}\alpha^{4/3}\left(\frac{H}{R}\right)^2\frac{(B_o/2)^{1/3}}{H^{4/3}}t$ with α = entrainment constant = 0.1 and R is the equivalent radius for the rectangular tank. In contrast, this interaction of the plume rise with the changing ambient condition cannot be satisfactorily simulated by either the actual source (AS) method or the USTL methods (Fig. 3.3).

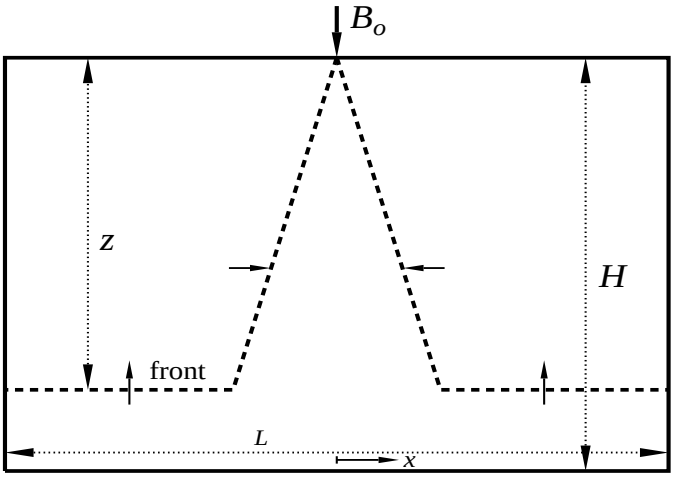

Figure 3.1: The schematic setup of the turbulent buoyant jet in a confined region experiment.

For this test case, the physical dimensions are rather small, and the horizontal size employed is only about $0.1H$. At the final stage of the jet, the plume elements are bigger than a horizontal grid cell. However, it is found the method of applying the sources and sinks at the centre of the plume elements still works satisfactorily. Fig. 3.4 and 3.5 also show that the vertical profiles obtained using a coarser grid (11 x 7 x 20) agree well with the finer grid model results.

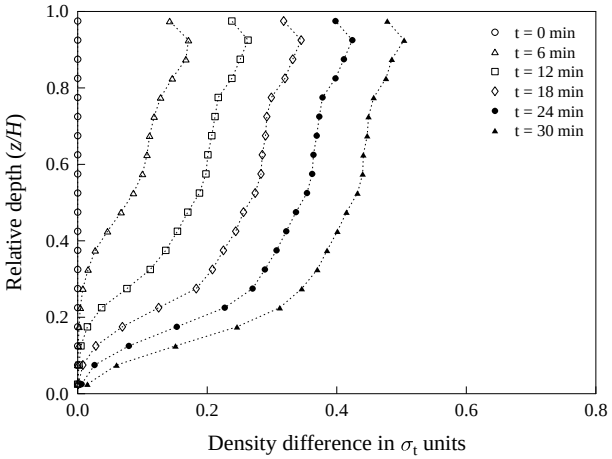

Figure 3.2: Predicted ambient density profiles at $x = 5\Delta x$ from the jet at different times after release of a buoyant source with $B_o = 154$ cm^4/sec^3.

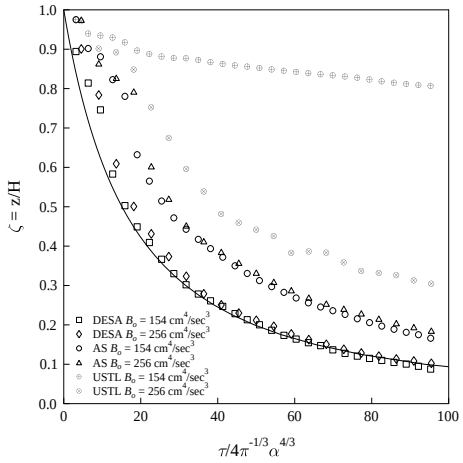

Figure 3.3: Computed time variation of dimensionless interface position (symbols). Solid line is best fit of experimental data represented by analytical solution of Baines and Turner (1969).

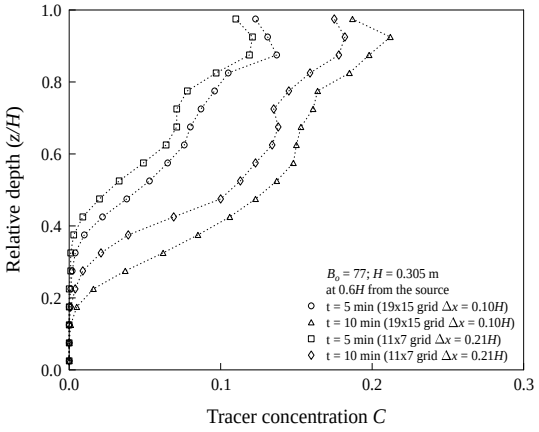

Figure 3.4: Predicted ambient density profiles at $x = 0.6H$ from the jet at different times after release of a buoyant source with $B_o = 77$ cm^4/sec^3.

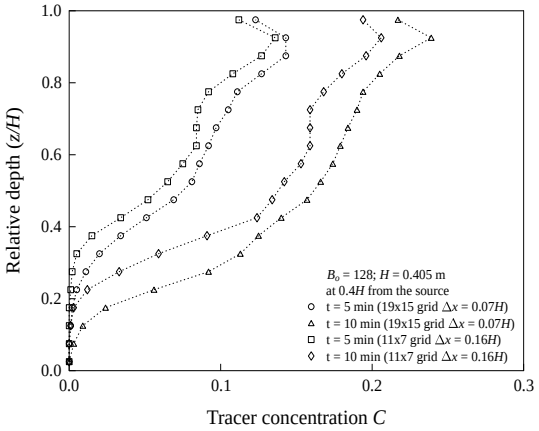

Figure 3.5: Predicted ambient density profiles at $x = 0.4H$ from the jet at different times after release of a buoyant source with $B_o = 154$ cm^4/sec^3.

3.2 Round buoyant jet in stagnant linearly density-stratified ambient fluid

The interaction between a buoyant jet and the ambient fluid can be illustrated for a round jet in otherwise stagnant linearly stratified fluid. The numerical prediction using the present method is compared with a well-documented experiment by Wong (1986). In his experiment, the (negatively) buoyant jet was created by discharging saline fluid downwards from a circular orifice into a linearly stratified receiving water in a 457 cm x 61 cm x 91 cm deep tank (Fig. 3.6). The key experimental parameters are: $D = 0.511$ cm, $V_o = 1.518$ m/s, source densimetric Froude number $F_o = \frac{V_o}{\sqrt{gD(\rho_o - \rho_a(0))/\rho_a(0)}} = 112$, where $\rho_a(0)$ is the ambient density at source level, and ambient stratification parameter $\epsilon = -\frac{g}{\rho_a(0)}\frac{d\rho_a}{dz} = 0.0762$ s^{-2}. A 21 x 3 x 20 model grid (with $\Delta x = 21.8$ cm by $\Delta y = 20.3$ cm and 20 uniform vertical layers) closed at the four sides is employed. The model is cold started and run for a duration of 15 minutes, similar to the length of experiment. A time step not greater than 0.25 second (with maximum Courant No. $Cr \approx 3.7$ and $u\Delta t/\Delta x \approx 0.03$) is needed for a stable solution.

Fig. 3.7 and Fig. 3.8 show the plan and section views of the unsteady buoyant spreading

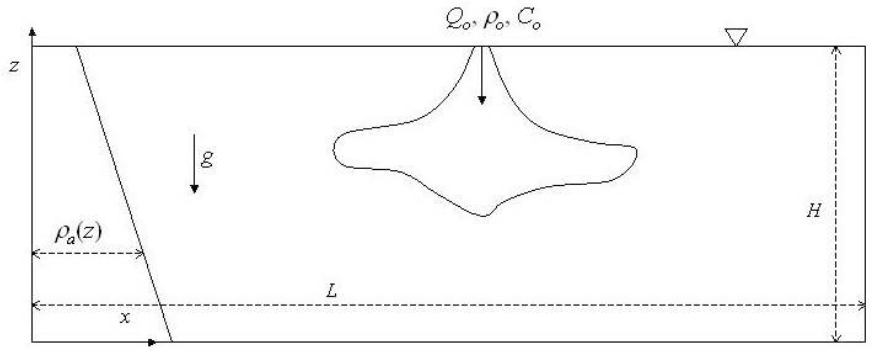

Figure 3.6: Vertical round buoyant jet in stagnant linearly density-stratified ambient fluid.

at selected times. It is seen that the mixed jet fluid finds its level of density and spreads at the trapping level as a buoyant intrusion layer, with a weak counterflow both above and below; both the tracer concentration and velocity profiles are relatively uniform within the layer. It is also noted that horizontal concentration gradients are negligible in the spreading layer; the layer thickness within $x = 1$ - $2\ Z_m$ is relatively constant as the front advances, where Z_m = maximum height of rise. The density intrusion displaces the surrounding fluid, and modifies the ambient density profile, resulting in increased density gradients both above and below the trapping level. The ambient density is increased above the layer and decreased below it. Fig. 3.9 shows the predicted change in vertical salinity profile (at $x = 3\ \Delta x = 1.24\ Z_m$ from source) is in excellent agreement with the experimental data. It also shows that there are very small differences between the results with different model grid sizes.

All three alternatives methods have been used to simulate the test case described above. Fig. 3.10 shows that these alternative near-far field coupling methods fail to reproduce the observed change in ambient stratification. In particular, the thickness of the spreading layer is grossly under-predicted by the Actual Source (AS) and Undiluted Source at Trapped Level

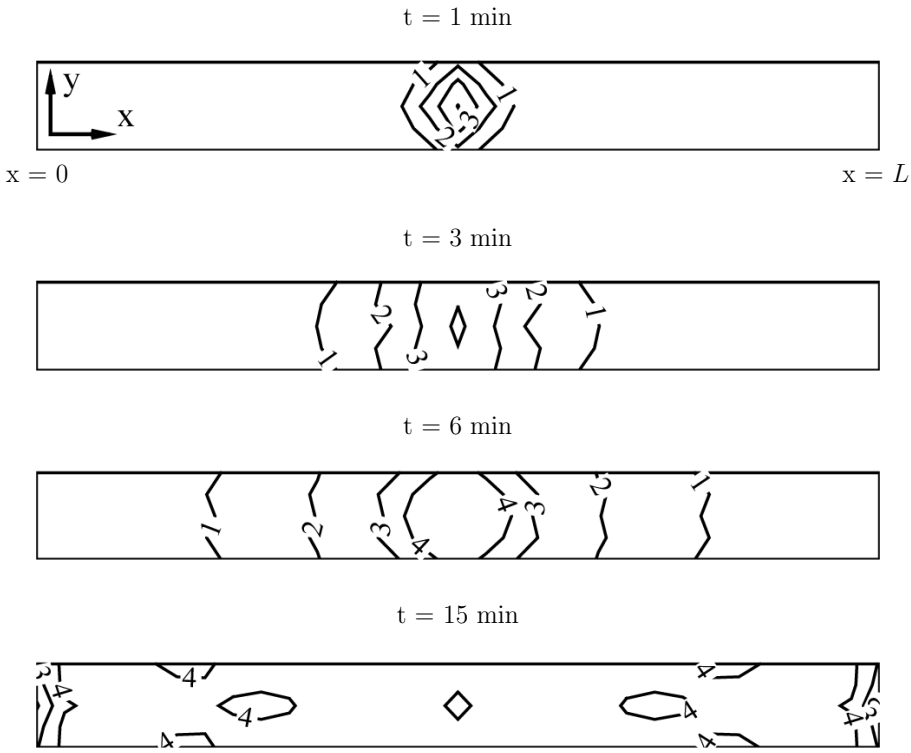

Figure 3.7: Computed tracer concentration distribution in the horizontal plane at the trapping level for a vertical round buoyant in stratified ambient (Run 1006-82 of Wong 1986) at selected times (contour in $0.01C_o$).

(USTL) approaches (see Fig. 2.1). For the Diluted Source at Trapped Level (DSTL) method, the extra water introduced cause excessive reduction in the ambient salt concentration. Both AS and USTL methods fail to reflect the change in ambient stratification even qualitatively. The effluent is trapped at a much lower level than the measured one. From the computed tracer distribution (of the 3D model), the minimum dilution can also be calculated from the predicted maximum concentration. Table 3.1 shows that the predicted dilution, trap level and spreading layer thickness (defined by 0.1 C_{max} in the profile) are in good agreement with data, while the alternative predictions can differ greatly from the observations. The computed results by JETLAG and DESA do not agree exactly because those from the latter are determined in the far field model and include the interaction effect of the jet and the ambient. It should be noted that in spite of the hydrostatic approximation, the jet overshoot or maximum height of rise can still be satisfactorily predicted. It should be noted that the AS method does not simulate the near field jet entrainment, while the DSTL method introduces excess flow and does not conserve mass.

Table 3.1: Predicted mixing and spreading layer characteristics of a vertical round buoyant jet in stagnant linearly stratified ambient fluid by dynamic coupling of near and far field models (DESA)

	Measured	JETLAG	DESA	AS	DSTL	USTL
Minimum dilution at trapping level S_m	25.5	23.4	20.9	4.7	73.1	3.7
Maximum height of rise Z_m (cm)	56.0	51.7	52.7	29.5	66.8	30.3
Level of minimum dilution in the spreading layer z_s (cm)	32.0	28.0	36.7	5.6	27.3	18.9
Spreading layer thickness h_s (cm)	20.5		27.1	25.1	74.3	16.1

t = 1 min

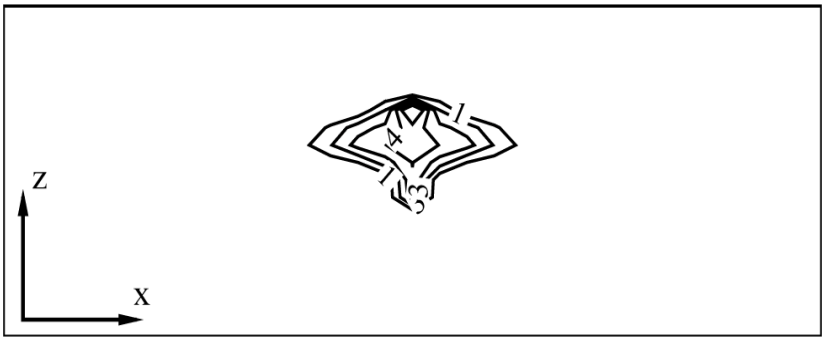

x = 0 x = L

t = 6 min

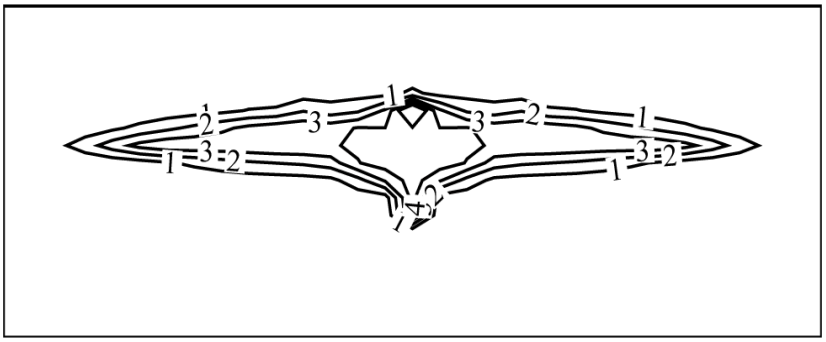

t = 15 min

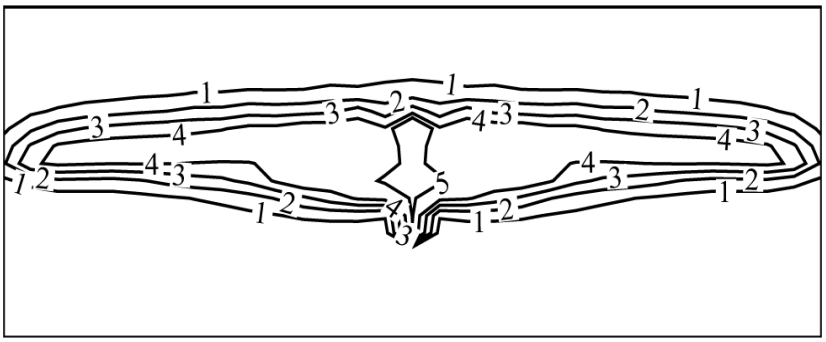

Figure 3.8: Computed tracer concentration distribution in the vertical section across the discharge point for a vertical round buoyant in stratified ambient (Run 1006-82 of Wong 1986) at selected times (contour in $0.01C_o$).

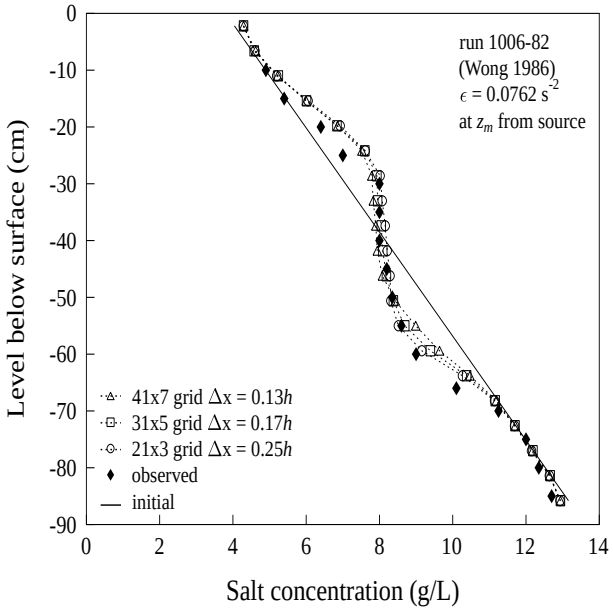

Figure 3.9: Ambient salt concentration profiles before and after a round jet discharge into a linearly stratified fluid (Wong 1986) with different model grid sizes.

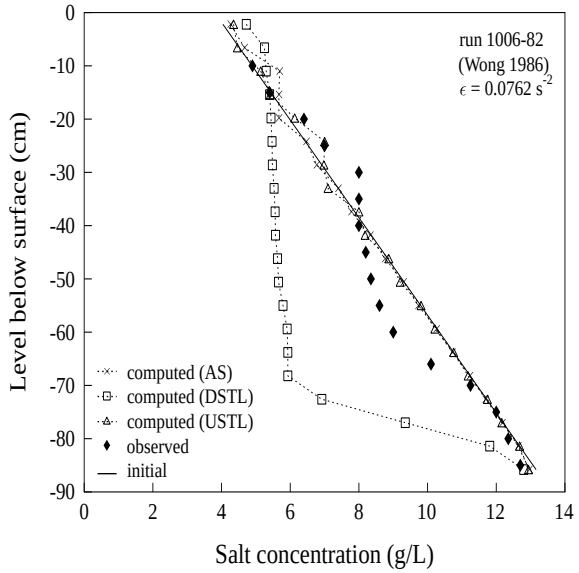

Figure 3.10: Ambient salt concentration profiles before and after a round jet discharge into a linearly stratified fluid (Wong 1986) with alternative coupling methods.

3.3 Round buoyant jet in uniform stagnant ambient fluid

DESA is a method that simulates the near-far field interaction by incorporating the jet entrainment into the far field model. A series of numerical experiments is carried out to simulate the behaviour of the vertical round buoyant jet in stagnant uniform water. For prototype scale cases, the discharge flow Q_o ranges from 0.003 to 0.06 m^3/s, while the initial reduced gravitational acceleration $g' = g\Delta\rho/\rho_a$ varies from 0.073 to 0.218 m/s^3. The water depth is kept constant at $H = 20$ m. For the laboratory scale cases, Q_o ranges from 0.004 to 0.28 L/s, g' ranges from 0.01 to 0.85 m/s^3 and H varies from 0.13 to 0.30 m. Fro all cases, a 33 x 33 x 20 non-uniform model grid (with $\Delta x = \Delta y$ ranges from $0.4H$ to $2H$ and 20 uniform vertical layers) open at the four sides is employed. All model runs are cold started. Table 3.2 & 3.3 lists the key parameters for the simulations. S_{min} is the minimum dilution in the intermediate field as inferred from the maximum concentration computed by DESA. Fig. 3.11 shows the predicted dilution at $R = 3.6H$ from all the numerical experiments. It can be seen the computed dilutions are in good agreement with the best-fit empirical relation given by Wright *et al.* (1991) based on the data of Lee and Jirka (1981):

$$\frac{S_{min} l_Q}{H} = 0.77 \left(\frac{H}{l_M}\right)^{2/3} \tag{2.2}$$

where $l_Q = Q_o/\sqrt{M_o}$ is a length scale representing the effect of the source volume flux and $l_M = M^{3/4}/B^{1/2} = \sqrt{(\pi/4)F_o D})$ is a length scale that measures the importance of the source momentum flux M.

Fig. 3.12 - 3.17 show the velocity fields and the tracer concentration distributions at the surface and in a vertical section across the discharge point. For vertical discharge in a stagnant water, the near field simulation can be terminated either when plume hits the water surface (stopping criterion A) or when the plume is less than the plume radius below the water surface (stopping criterion B).

As shown in Fig. 3.18, the computed cumulative entrainment flows $Q_e(z)$ from the bottom in the far field model at $0.2H$ from the discharge point by the latter approach are smaller than the former one and closer to those computed by JETLAG, but the difference becomes smaller with greater F_o (Fig. 3.19). With the introduction of the source/sink terms, vertical flows are induced and cause the differences in the entrainment flows into the grid cells and prescribed source/sink terms. The q_e at $0.2H$ for both approaches are greater than those computed by JETLAG and pure plume/jet (by $S_p Q_o = 0.163 B_o^{1/3} z^{5/3}$ and $S_j Q_o = 0.29 M_o^{1/2} z$) below the bottom of the outflowing layer and again the differences are smaller with increase in F_o. In Table 3.2, Q_t is the estimated outgoing flow in the spreading layer across the cross-section (approximately circular in the rectangular grid) at different radial location R from the discharge point. It can be seen that the total entrainment flows Q_t at $0.2H$ are in general smaller than those for the round plume at the surface, but in accordance with experiments, the total entrained flows beyond $0.6H$ can be several times that induced by the pure jet or plume - reflecting the additional mixing in the transition from near to intermediate/far field (see Kuang and Lee 2006) and the computed dilutions agree well with the laboratory data (Fig. 3.11).

Table 3.2: Key parameters for vertical round buoyant jet in stagnant uniform water and computed flows in the surface spreading layer (prototype scale)

Q_o m^3/s	g' m^3/s	F_o	l_M/H	S_pQ_o m^3/s	S_jQ_o m^3/s	Q_t at $0.2H$ (1 grid) m^3/s	Q_t at $0.6H$ (2 grids) m^3/s	Q_t at $3.6H$ (4 grids) m^3/s	$S_{min}Q_o$ at $3.6H$
0.003	0.218	2.59	0.012	1.999	0.191	1.441	3.132	12.049	9.677
0.006	0.218	5.17	0.024	2.519	0.383	1.865	4.758	14.372	10.714
0.006	0.145	6.34	0.030	2.200	0.382	1.811	3.642	9.195	9.091
0.006	0.073	8.96	0.042	1.746	0.382	1.656	3.857	10.770	10.169
0.012	0.218	10.34	0.049	3.174	0.766	2.442	5.7124	12.132	10.619
0.018	0.218	15.51	0.073	3.633	1.149	2.919	5.998	13.331	13.139
0.024	0.218	20.69	0.097	3.999	1.531	3.280	6.948	14.640	14.035
0.030	0.218	25.86	0.122	4.308	1.914	3.593	7.870	16.188	16.129
0.060	0.218	51.72	0.243	5.427	3.829	5.069	10.437	22.472	21.818
0.060	0.145	63.38	0.298	4.739	3.829	4.586	9.458	20.027	18.750
0.060	0.073	89.60	0.422	3.762	3.829	3.914	8.189	19.651	15.000

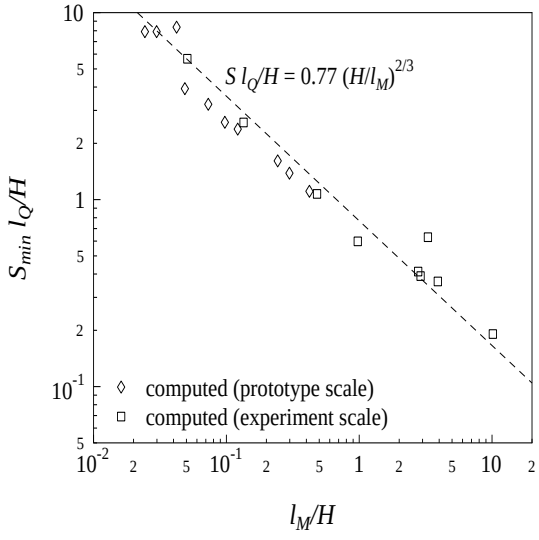

Figure 3.11: Predicted minimum surface dilution of vertical round buoyant jet in stagnant ambient ($R = 3.6H$).

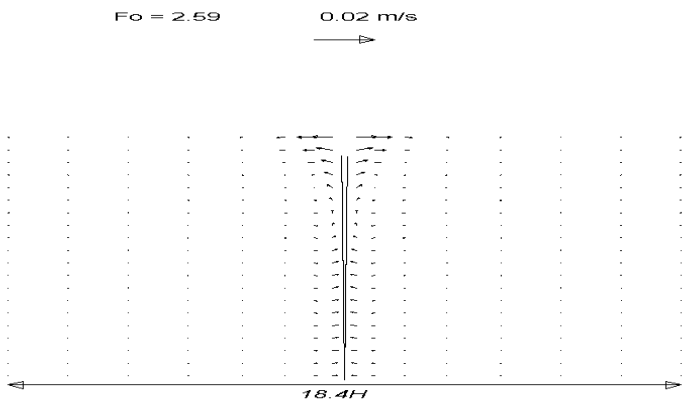

Figure 3.12: Computed velocity in a vertical section across a plume discharge ($F_o = 2.59$) at t = 120 min.

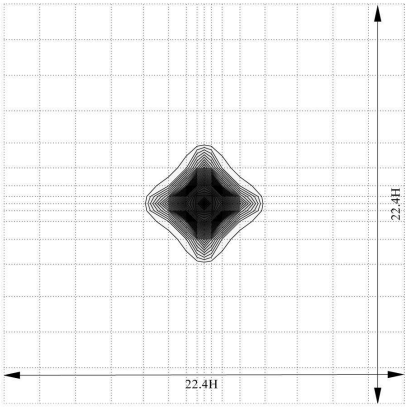

Figure 3.13: Computed surface tracer concentration for a plume discharge ($F_o = 2.59$) at t = 120 min.

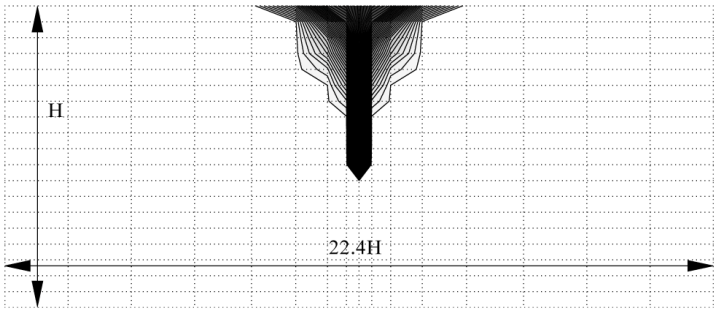

Figure 3.14: Computed tracer concentration in a vertical section across a plume discharge (F_o = 2.59) at t = 120 min.

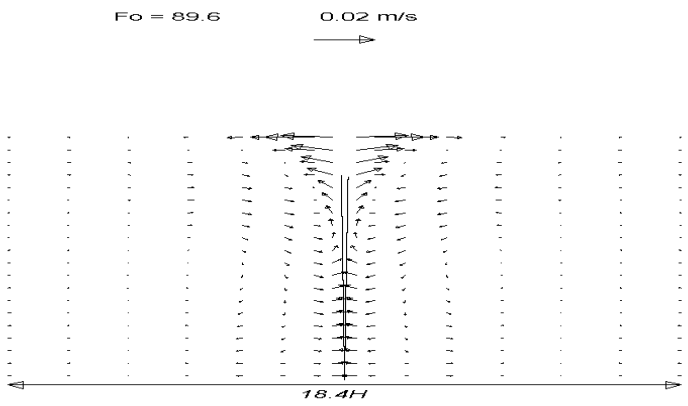

Figure 3.15: Computed velocity in a vertical section across a jet discharge ($F_o = 89.6$) at $t = 120$ min.

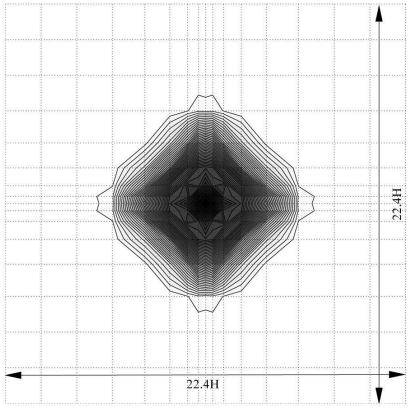

Figure 3.16: Computed surface tracer concentration for a jet discharge ($F_o = 89.6$) at $t = 120$ min.

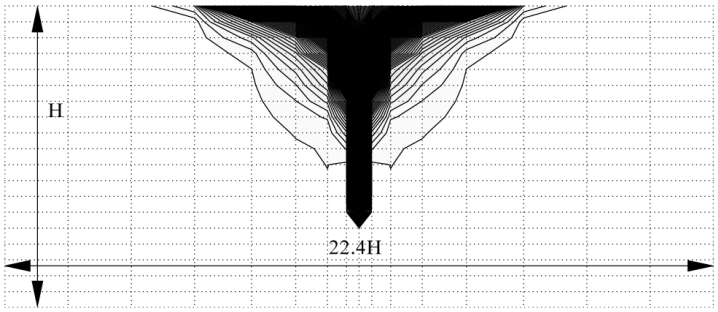

Figure 3.17: Computed tracer concentration in a vertical section across a jet discharge ($F_o = 89.6$) at $t = 120$ min.

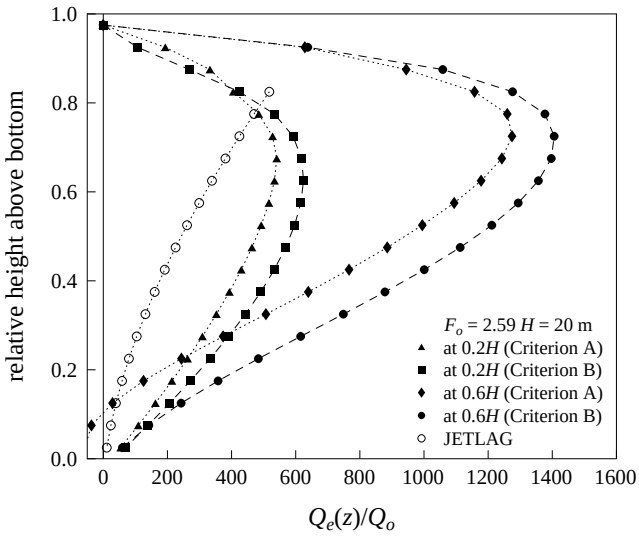

Figure 3.18: Computed entrainment flow for a plume discharge ($F_o = 2.59$).

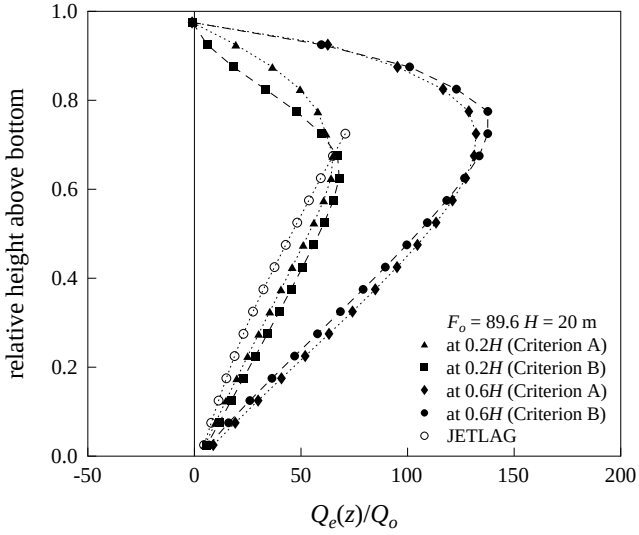

Figure 3.19: Computed entrainment flow for a jet discharge ($F_o = 89.6$).

In summary, DESA is a dynamic coupling method to be used in a 3D shallow water circulation model based on the hydrostatic approximation. The method is not expected to reproduce accurately the jet mixing details in the near field (say within a distance of the order of the depth from the source) - which must resort to a 3D calculation based on the RANS equations (see e.g. Kuang and Lee 2006). However, it is of interest to see whether the broad mixing details simulated by DESA (in particular the dilution in the intermediate field) are consistent with experimental data. The series of model simulations for a vertical round buoyant jet in uniform stagnant water (Table 3.2 & 3.3) shows a surface layer of thickness $0.1H$ to $0.2H$ for all simulated cases. Although the detailed velocity and concentration fields computed by the 3D far field model close to the source (say within $0.5H$) are not (correctly so) realistic, beyond two grid cells and a distance in the order of $1H$, the inflowing entrainment flow in the lower layer, and the outflowing buoyant surface layer are correctly reproduced. The computed dilutions near the discharge are also found to be comparable to those obtained from the RANS solution and the empirical relation described above (Fig. 3.11).

Table 3.3: Experiment parameters for vertical round buoyant jet in stagnant uniform water and computed dilution (laboratory experiment scale)

Q_o L/s	g' m^3/s	F_o	l_M/H	S_{min} at $3.6H$
0.004	0.852	3.3	0.04	390.6
0.010	0.832	8.7	0.13	178.3
0.136	0.011	26.4	3.31	5.33
0.011	0.096	28.9	0.48	68.63
0.105	0.037	38.1	2.76	6.05
0.136	0.045	44.5	3.89	4.45
0.280	0.018	46.2	2.90	6.60
0.024	0.096	61.5	0.07	40.83
0.141	0.044	260.9	10.2	5.19

3.4 Inclined dense jet

Roberts *et al.* (1997) performed experiments on inclined turbulent dense jets discharged upwards at an angle of 60° into stagnant environment (Fig. 3.20). The experiments were conducted in a channel 6.1 m long, 0.91 m wide and 0.61 m deep for different nozzle diameter D, ambient density ρ_a, effluent density ρ_o and effluent flowrate Q_o (Table 3.4). The height of the nozzle tip was 35 mm above the bottom. A 33 x 17 x 20 model grid with closed boundaries at four sides, a horizontal grid size of 19.7 cm by 6.07 cm and 20 uniform vertical layers is employed. The model is run from cold start and the time step of 0.025 sec. is used (with $Cr = 0.76$). Simulations using DESA and AS are carried out.

The initial region of the dense jet is similar to an upwards-inclined momentum jet; the negative buoyancy however causes the jet to reach a terminal rise height before it falls back to the bottom. It then spreads as a density current. For an inclined jet, the spreading layer will be asymmetric. Fig. 3.21 shows the trajectory of the dense jet predicted by the near field model and the corresponding sources and sinks in the far field model for the DESA approach. From Fig. 3.22, it can be seen that DESA is able to simulate the initial rise and fall of the jet as well as the spreading layer along the bottom, while AS cannot model the rise and fall of the jet and only a symmetric spreading layer is formed at the bottom (Fig. 3.23). To compare the results quantitatively, the dilution and the thickness of the bottom layer at the location of "ultimate minimum dilution" (or length of mixing zone) as defined in Roberts *et al.* (1997) are taken as the minimum dilution S_m and the thickness of the spreading layer y_L. As shown in Fig. 3.24, the predicted spreading layer thickness by AS is much smaller than those observed from the experiment, while those obtained by DESA agree well with experiments. Also, Fig. 3.25 shows the computed dilutions by DESA are very close to that deduced from the experiment, while those obtained by AS are highly varying and can be significantly smaller.

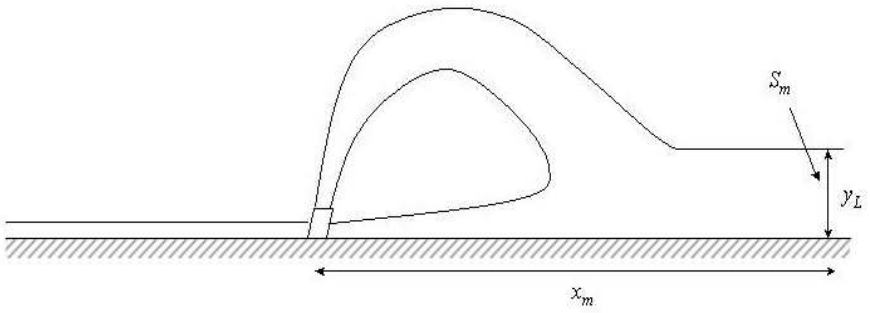

Figure 3.20: Inclined dense jet.

Table 3.4: Summary of experimental conditions for inclined dense jet in stagnant water

Nozzle diameter D (mm)	Ambient density ρ_a (g/L)	Effluent density ρ_o (g/L)	Effluent flowrate Q_o (L/s)	Jet densimetric Froude number F_j
4.29	0.9974	1.0324	10.4	18.7
4.29	0.9974	1.0300	14.2	26.4
4.29	0.9982	1.0157	9.5	24.0
2.97	0.9982	1.0204	6.3	35.7

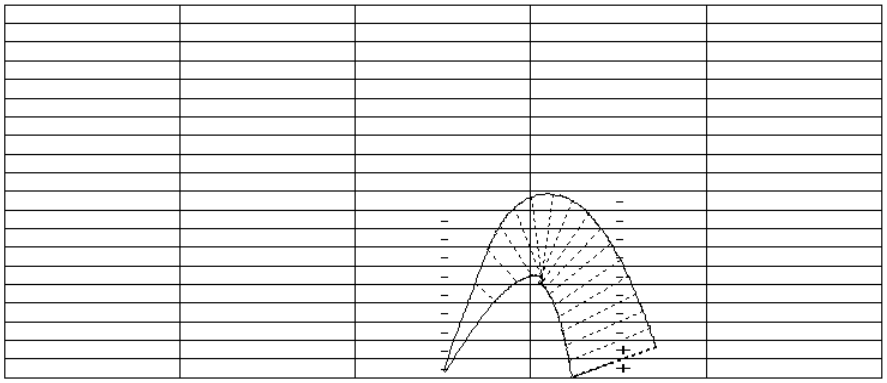

Figure 3.21: The computed plume and source (+) / sink (−) terms in the far field model for inclined dense jet.

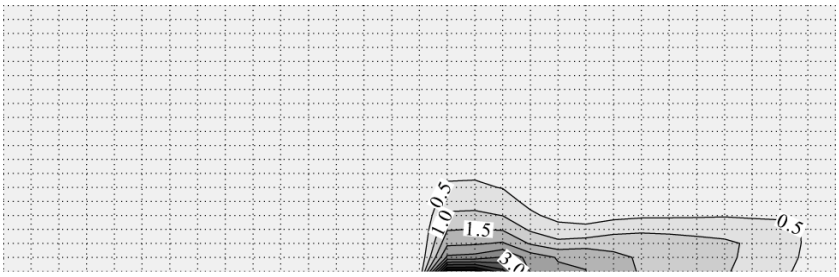

a) DESA

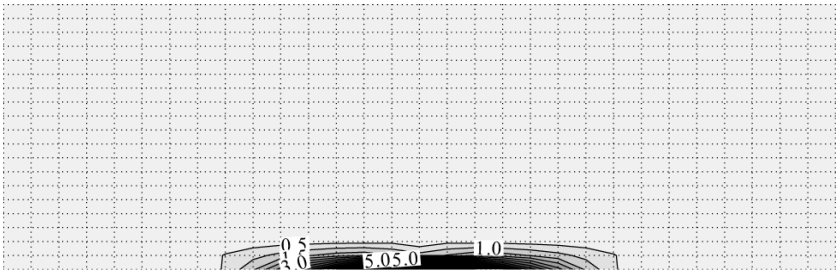

b) AS

Figure 3.22: Computed tracer concentration field for a vertical section across the discharge point for inclined dense jet with $F_j = 18.7$ (concentration in $0.01C_o$).

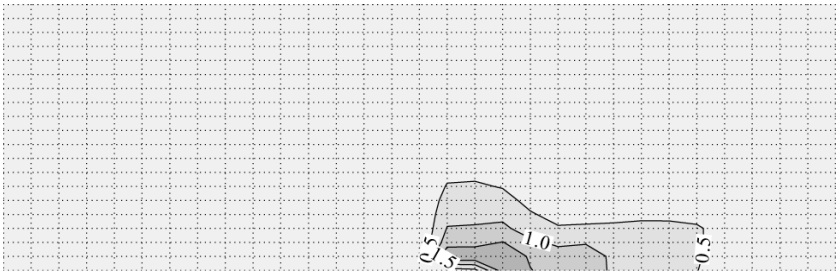

a) DESA

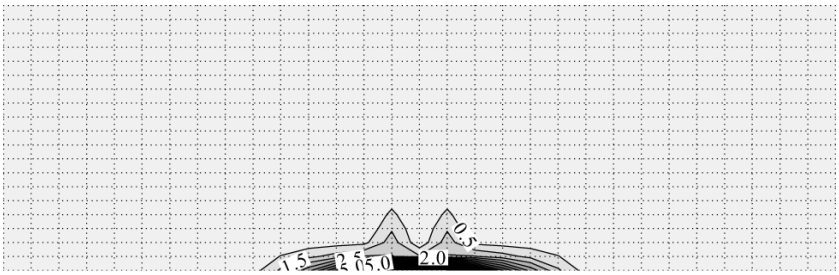

b) AS

Figure 3.23: Computed tracer concentration field for a vertical section across the discharge point for inclined dense jet with $F_j = 35.7$ (concentration in $0.01C_o$).

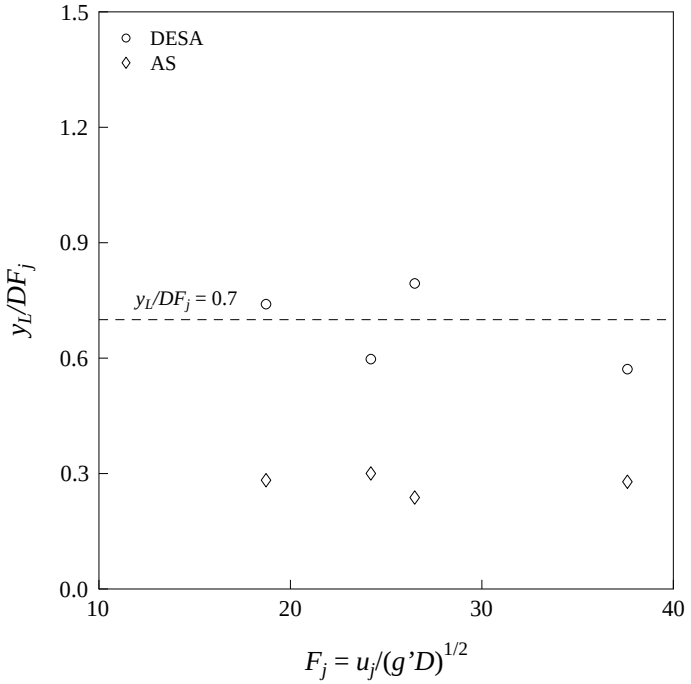

Figure 3.24: Predicted thickness of bottom layer for inclined dense jet.

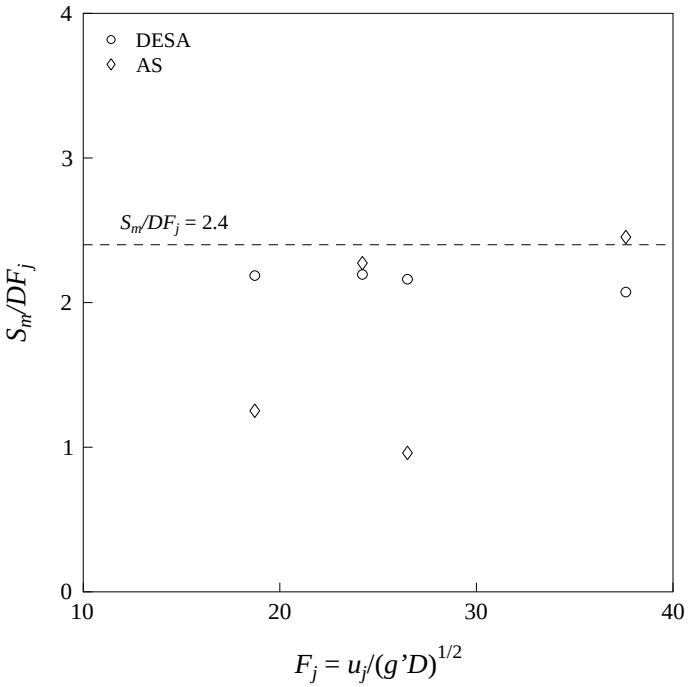

Figure 3.25: Predicted minimum dilution for inclined dense jet.

Chapter 4

Plane Buoyant Jet

4.1 Plane vertical buoyant jet in stagnant uniform water

4.1.1 Source represented by 2D jet

A series of numerical experiments is carried out to simulate the behaviour of the plane vertical buoyant jet in stagnant uniform water (Fig. 4.1). The unit discharge flow (per unit width) q_o ranges from 0.1 to 1.0 m^2/s, while the initial relative density difference

$$\Delta\rho^* = \frac{\rho_a - \rho_o}{\rho_a}$$

varies from 0.0075 to 0.029. Two water depths H = 12 m and 25 m, are examined. For all cases, a 29 x 1 x 20 non-uniform model grid (with Δx from 10 m to 50 m or $0.4H$ to $4H$, Δy = 10 m or $0.4H$ to $0.9H$ and 20 uniform vertical layers) is employed (Fig. 4.2), with open boundaries at two ends. The slot diffuser is modelled by a plane buoyant jet model based on the following governing equations (see e.g. Lee and Cheung 1986) and solved by a Lagrangian approach tracking the evolution of an elemental volume.

$$\frac{dq}{ds} = 2\sqrt{2}\alpha\frac{m}{q}$$

$$\frac{dm_y}{ds} = \sqrt{2}\lambda bq\sin\theta$$

$$\frac{db}{ds} = -\sqrt{\frac{1+\lambda^2}{\lambda^2}}\epsilon q\sin\theta$$

$$\alpha = 0.055 + 0.16875b\left(\frac{q}{m}\right)^3$$

where q, m and b are the unit-width volume, momentum and buoyancy fluxes respectively, $m_y = (m\sin\theta)^2$ is the square of vertical momentum, α is the entrainment coefficient, $\lambda = 1.35$ and $\epsilon = -\frac{g}{\rho_{ao}}\frac{d\rho_a}{dz}$ is the stratification parameter.

Thirty-two simulations have been carried out with the initial unit buoyancy flux $b_o = q_o\Delta\rho^* g$ = 0.003 - 0.131 m^3/s^3 and initial momentum flux $m_o = q_o u_o$ = 0.01 - 0.1 m^3/s^2 (Table 4.1). A time step of 1 sec. (with maximum Courant no. $Cr \approx 1.57$) is applied for all cases.

As expected, when the diluted buoyant effluent reaches the water surface, the flow becomes nearly horizontal and spreads out nearly uniformly; hence a two-layer circulation in the vertical

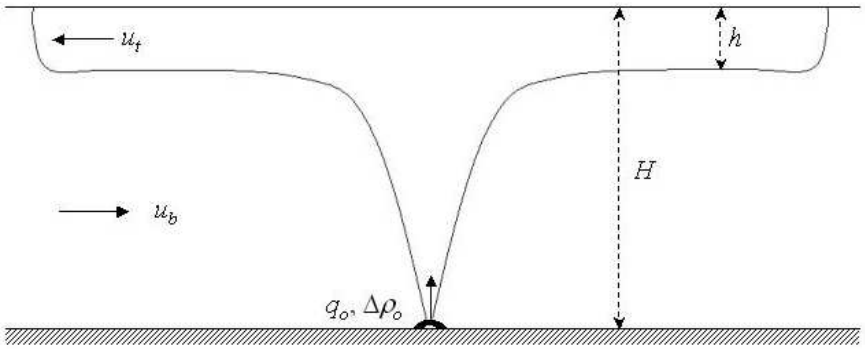

Figure 4.1: Plane vertical buoyant jet discharging into stagnant water.

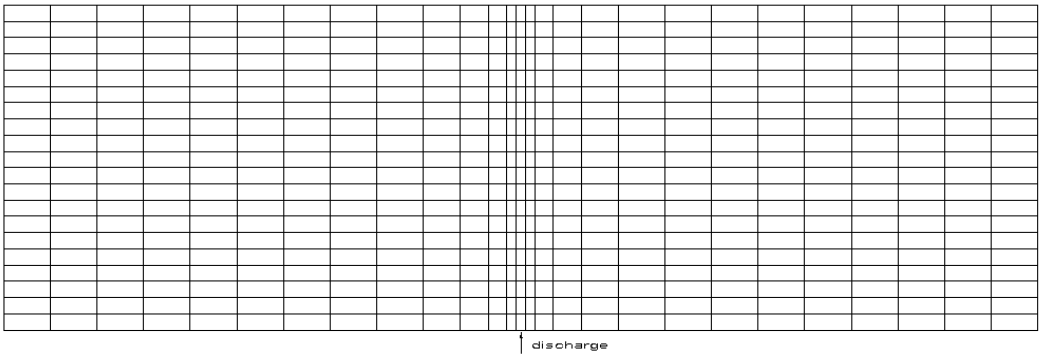

Figure 4.2: Non-uniform grid for a plane vertical buoyant jet into stagnant uniform water.

direction is formed (Fig. 4.3). From the model results, the layer-averaged velocity of the flow moving away from the source in the spreading layer, u_t, (relative to a stationary observer) and the layer-averaged opposing undercurrent velocity of the entrainment flow, u_b, moving towards the source can be computed. The velocity of advance of the spreading layer relative to the otherwise stagnant water, $u^* = u_t + u_b$, is then determined. As shown in Fig. 4.4a, u^* is found to be linearly proportional to the cubic root of the initial buoyancy flux, i.e. $b_o^{1/3}$, with a ratio of $\beta = 0.9$. It is quite close to the theoretical value of unity obtained by Chen (1980) using a similarity solution, and is greater than $\beta = 0.83$ given in Koh (1983). It is also found that the velocity in the spreading layer u_t is linearly proportional to $b_o^{1/3}$ and the coefficient of proportionality is 0.6 that is consistent with that obtained from the experiments of Roberts (1977) (Fig. 4.4b).

There are various ways to determine the thickness of the spread layer, h; it can be obtained based on the location of the plane of zero velocity. Alternatively, h can be found from the conservation of the volumetric flux across the vertical section, and is computed from the equation

$$h = \frac{u_b d + 0.5 q_o}{u^*}$$

It is found that the relative thickness of the spreading layer, h/H can be considered to be a constant for different initial buoyancy flux b_o (Fig. 4.5). For "plume-like" discharge with

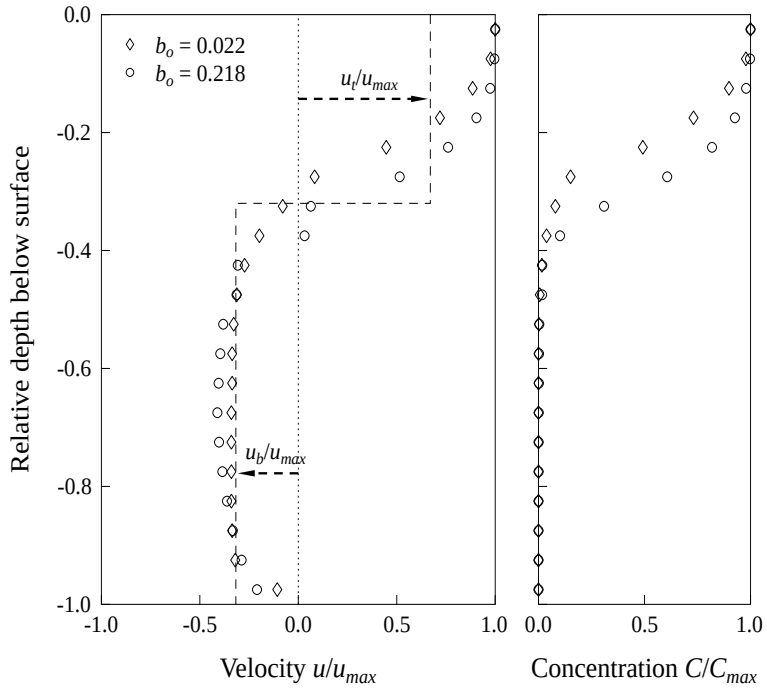

Figure 4.3: Vertical profiles of horizontal velocity and tracer concentration near the front of the spreading layer.

$l_m/H < 1$, where $l_m = m_o/b_o^{2/3}$ is a momentum length scale, the computed values are about 0.32 which is consistent with the experiments of Roberts (1977) and Chen (1980). Unlike the previous model of Koh (1983), the present approach is generally applicable to any buoyant jet, and is not limited to only pure plumes (Fig. 4.5). It is found that the almost constant relative thickness of the spreading layer is also applicable to "jet-like" buoyant jet with $l_m/H > 1.7$ and is about 0.43. With the computed velocities, the average dilution $S = u_t h/q_o$ can be calculated and is found to be equal to 0.56 $b_o^{1/3}$ $(H$ - $h)/q_o$ (Fig 4.6).

As mentioned above, the thickness of the spreading layer determined from the flow field is almost a constant for both "plume-like" and "jet-like" buoyant jets (Fig. 4.7). The corresponding spreading layer marked by the tracer concentration follows a similar pattern with the exception that the thickness for "jet-like" are much thicker indicating the difference in the vertical diffusion of momentum and tracer mass (Fig. 4.8). For the "plume-like" buoyant jet, the relative thickness of the tracer spreading layer is still around 0.32, but for the "jet-like" buoyant jet, it is increased from about 0.43 up to about 0.53. As shown in Fig. 4.9 and 4.10, the difference in the layer spreading thickness can easily be observed from the vertical profiles of the horizontal velocity and tracer concentration. Detailed examination of the results also shows that the spreading layer is fully established at about 4 grid cells or $3H$ from the source. The vertical circulation induced by the sources and sinks is restricted to the column containing the discharge point and its immediately neighbouring cells.

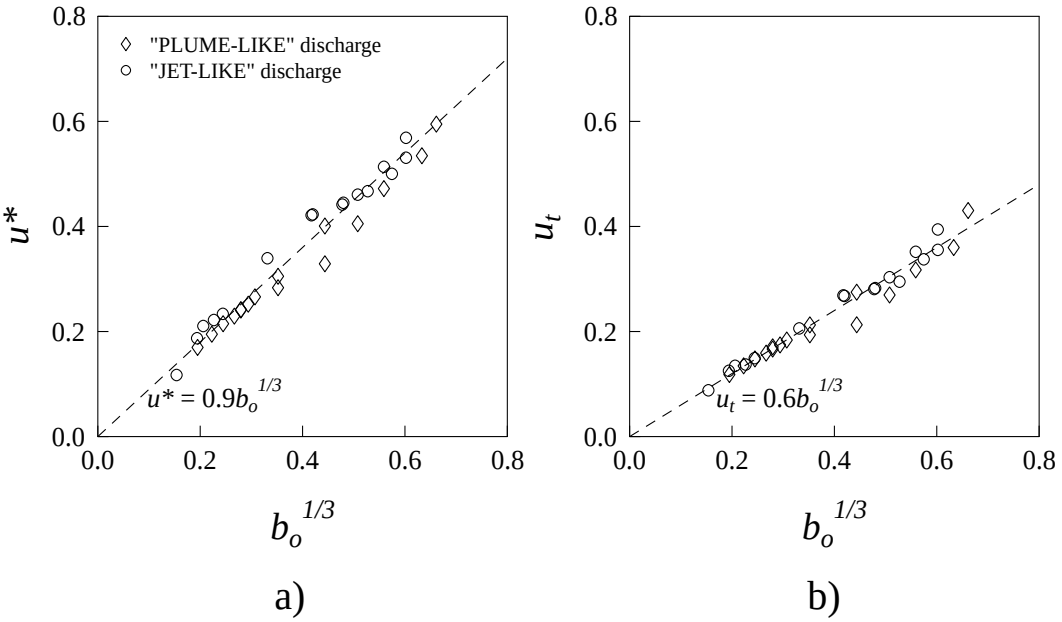

Figure 4.4: Computed advancing velocity of the spreading layer: (a) relative to stagnant fluid; and (b) relative to stationary observer.

Table 4.1: Experimental parameters for plane vertical buoyant jet in stagnant uniform water

q_o (m^2/s)	$g' = g\Delta\rho^*$ (m/s^2)	H (m)	m_o (m^3/s^2)	b_o (m^3/s^3)	$l_m/H = (m_o/b_o^{2/3})/H$
1.0	0.00364	25	10.0	0.00362	16.903
1.0	0.00728	25	10.0	0.00728	10.658
0.1	0.07400	25	0.1	0.00740	0.105
0.6	0.01456	25	3.6	0.00874	3.395
0.1	0.11046	25	0.1	0.01105	0.081
0.8	0.01456	25	6.4	0.01165	4.982
1.0	0.01456	25	10.0	0.01456	6.708
0.1	0.14660	25	0.1	0.01466	0.067
0.1	0.18967	25	0.1	0.01897	0.056
0.1	0.21821	25	0.1	0.02182	0.051
0.1	0.21821	12	0.1	0.02182	0.107
0.1	0.25375	25	0.1	0.02538	0.046
0.1	0.28918	25	0.1	0.02892	0.042
1.0	0.03637	25	10.0	0.03637	3.644
0.2	0.21821	25	0.4	0.04364	0.129
0.2	0.21821	12	0.4	0.04364	0.269
1.0	0.07269	25	10.0	0.07269	2.297
1.0	0.07400	25	10.0	0.07400	2.269
0.4	0.21821	25	1.6	0.08728	0.325
0.4	0.21821	12	1.6	0.08728	0.678
1.0	0.10898	25	10.0	0.10898	1.753
1.0	0.11046	25	10.0	0.11046	1.738
0.6	0.21821	25	3.6	0.13092	0.558
0.6	0.21821	12	3.6	0.13092	1.164
1.0	0.14660	25	10.0	0.14660	1.439
0.8	0.21801	25	6.4	0.17456	0.820
0.8	0.21801	12	6.4	0.17456	1.708
1.0	0.18967	25	10.0	0.18967	1.212
1.0	0.21821	25	10.0	0.21821	1.104
1.0	0.21821	12	10.0	0.21821	2.299
1.0	0.25375	25	10.0	0.25375	0.998
1.0	0.28918	25	10.0	0.28918	0.914

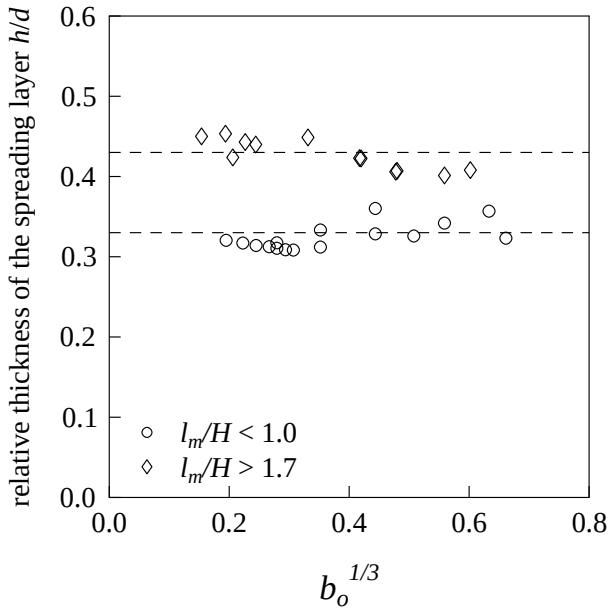

Figure 4.5: Relative thickness of the spreading layer vs. b_o.

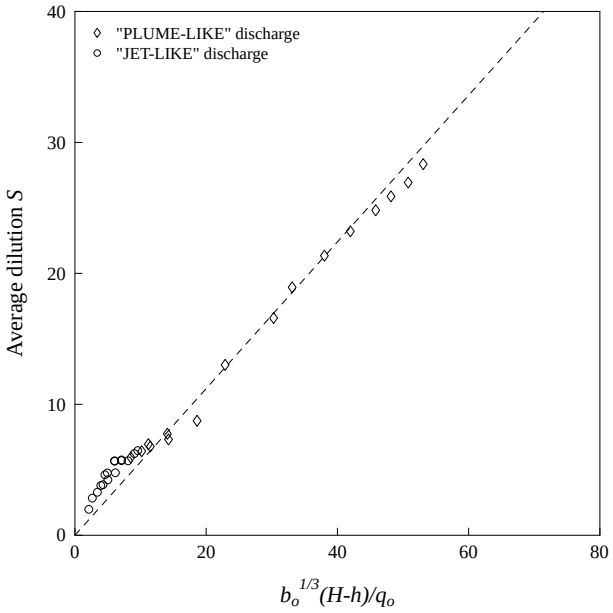

Figure 4.6: Computed average dilution in the spreading layer.

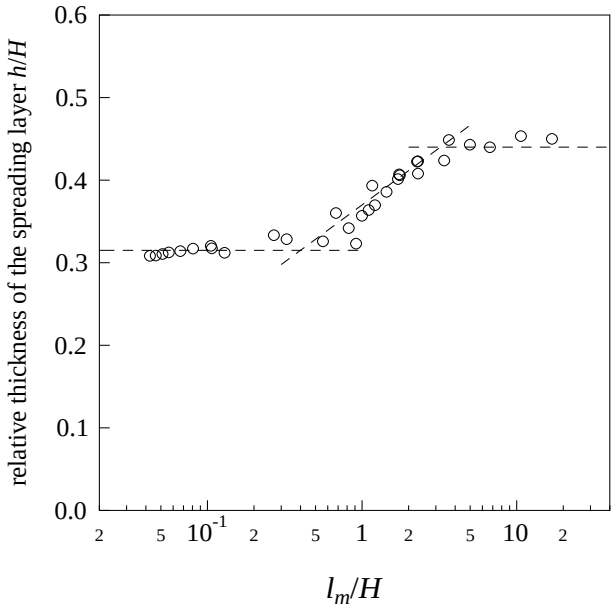

Figure 4.7: Relative thickness of the velocity spreading layer vs. l_m/H.

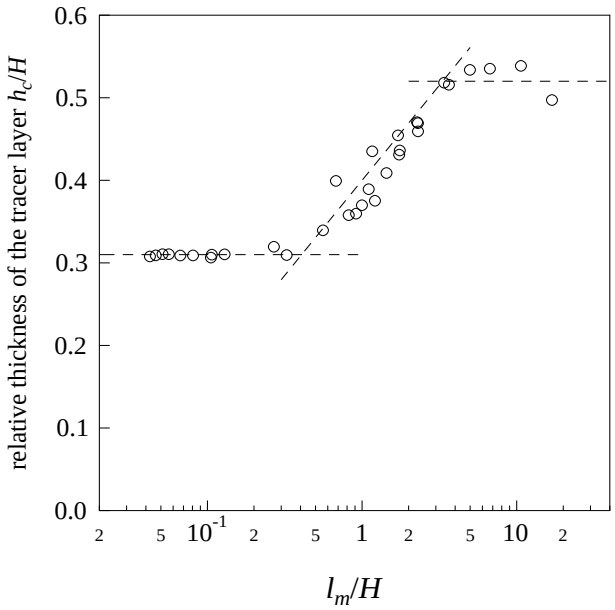

Figure 4.8: Relative thickness of the tracer spreading layer vs. l_m/H.

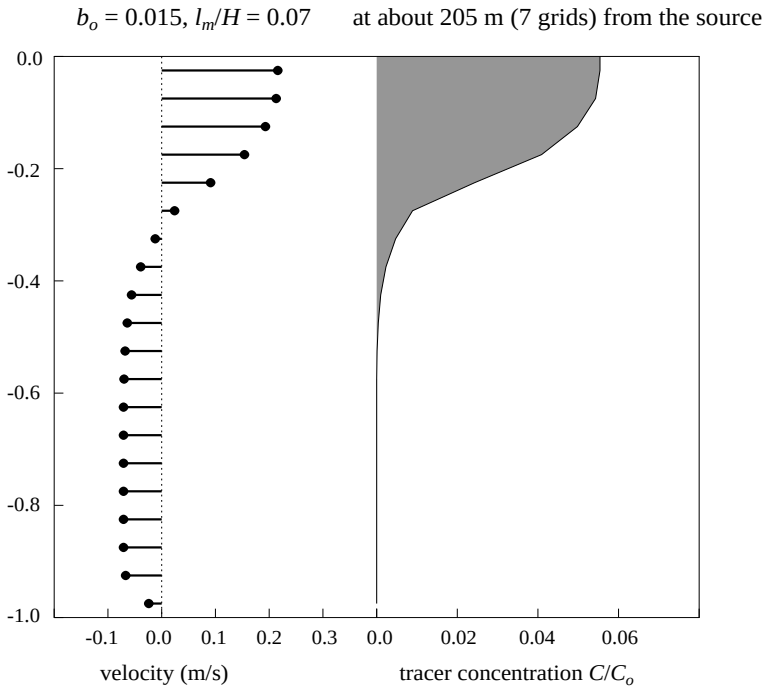

Figure 4.9: Velocities and tracer concentration profiles in the vertical section across the discharge point for a plane vertical "plume-like" buoyant jet in uniform water.

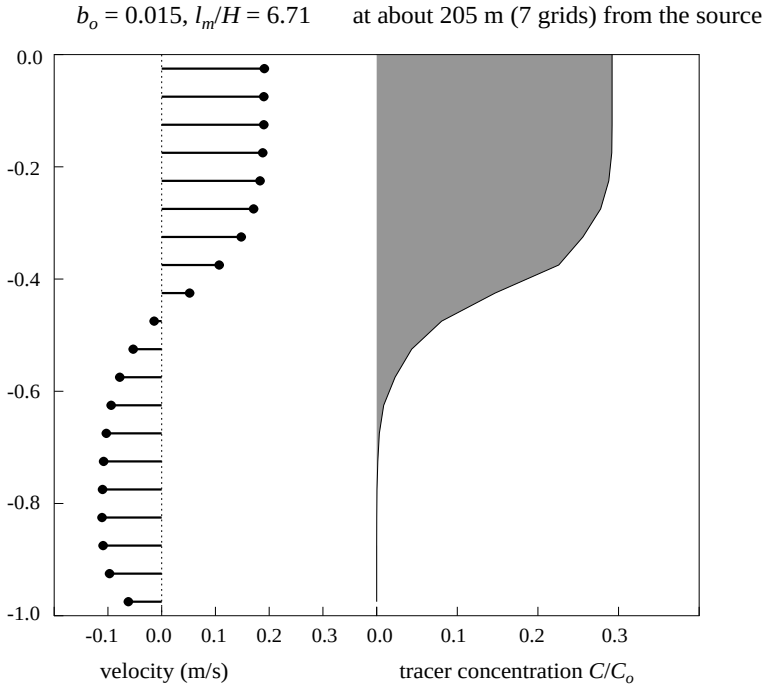

Figure 4.10: Velocities and tracer concentration profiles in the vertical section across the discharge point for a plane vertical "jet-like" buoyant jet in uniform water.

4.1.2 Source represented by 3D buoyant jets

A series of numerical experiments is also carried out to simulate the behaviours of the plane vertical buoyant jet in stagnant uniform water with the source represented by two equivalent non-interfering 3D (round) jets instead. The unit discharge flow (per unit width) q_o ranges from 0.1 to 1.0 m^2/s, while the relative initial density difference $\Delta\rho^*$ from 0.0075 to 0.029. Two water depths $H = 12$ m and 25 m, are examined. For all cases, the same model grid as described in Section 3.1.1 is employed (Fig. 4.2). The slot diffuser is represented by two non-interfering round jets with equivalent initial volume, momentum and buoyancy fluxes. Thirty-two simulations are carried out with the initial unit buoyancy flux $b_o = 0.022$ - 0.218 m^3/s^3 and initial momentum flux $m_o = 0.01$ - 0.1 m^3/s^2 (Table 4.2). A time step of 1 sec. (with maximum Courant no. $Cr \approx 1.57$) is applied for all cases.

From the model results, the layer-averaged velocity of the flow moving away from the source in the spreading layer, u_t, (relative to a stationary observer) and the layer-averaged opposing undercurrent velocity of the entrainment flow, u_b, moving towards the source can be computed. The velocity of advance of the spreading layer relative to the otherwise stagnant water, u^*, is then determined. As shown in Fig. 4.11a, u^* is found to be linearly proportional to the cubic root of the initial buoyancy flux, i.e. $b_o^{1/3}$, with a ratio of $\beta = 0.974$. This agrees well with the theoretical value of unity obtained by Chen (1980) using a similarity solution. The velocity in the spreading layer u_t is also linearly proportional to $b_o^{1/3}$ and the coefficient of proportionality is 0.652 that is consistent with that obtained from the experiments of Roberts (1977) (Fig. 4.11b). Both coefficients are greater than those obtained from representing the source by a 2D jet by about 10 percent.

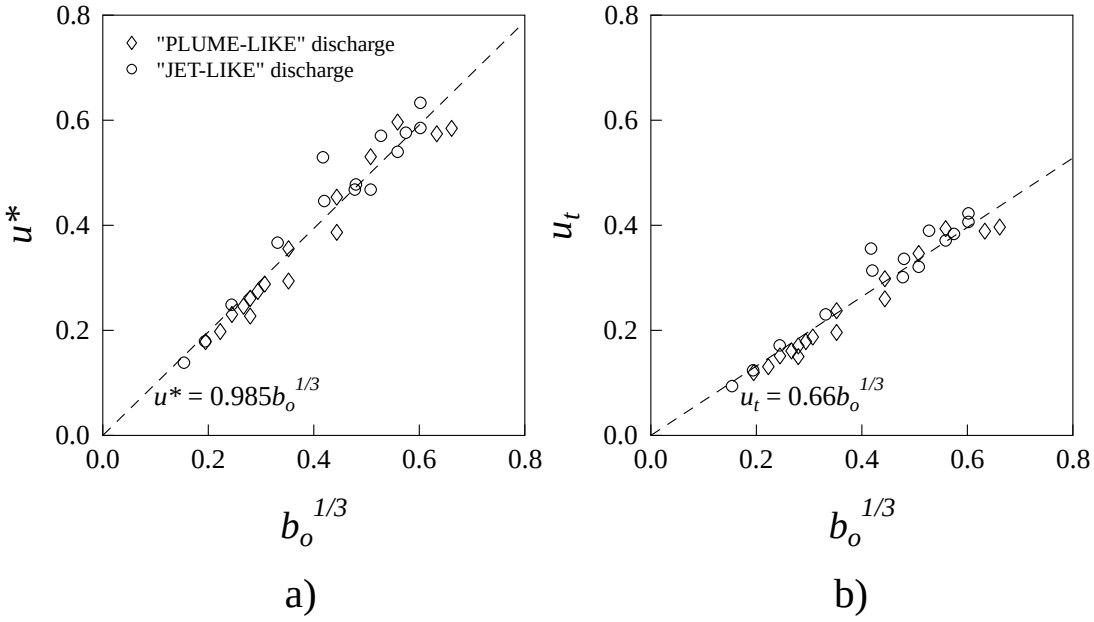

Figure 4.11: Computed advancing velocity of the spreading layer: (a) relative to stagnant fluid; and (b) relative to stationary observer.

It is found that the relative thickness of the spreading layer, h/H, can be considered to be a constant for different initial buoyancy flux b_o (Fig. 4.12). The computed values are about 0.36 which is consistent with the experiments of Roberts (1977) and Chen (1980). Unlike the

previous section, the thickness of the spreading layer is the same for both the "plume-like" and the "jet-like" discharge (Fig. 4.13). With the computed velocities, the average dilution $S = u_t h/q_o$ can be calculated and is found to be equal to 0.669 $b_o^{1/3}$ $(H - h)/q_o$ (Fig 4.14). It is about 1.2 times greater than that obtained using 2D jet as source, but is consistent with the experiments reported in Wright (1985).

As mentioned above, the thickness of the velocity spreading layer determined from the

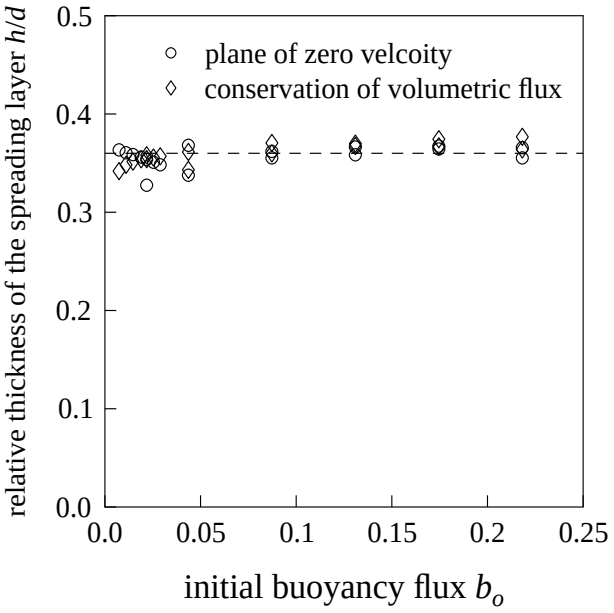

Figure 4.12: Relative thickness of the spreading layer vs. b_o.

flow field is similar for both "plume-like" and "jet-like" buoyant jets, but the corresponding spreading layer marked by the tracer concentration is quite different for the two types of buoyant jets. As shown in Fig. 4.19 and 4.20, the relative thickness of the tracer spreading layer for the "plume-like" buoyant jet is still around 0.36, that for the "jet-like" buoyant jet is much thicker and is up to about 0.5.

As shown in Table 4.3, it is confirmed the dilution of the buoyant jet is due to the entrainment flow in the counterflow bottom layer, which is consistent with that computed by the near field JETLAG model. Compared to the results obtained from running the standalone version of JETLAG, the small difference can be related to the additional mixing in the transition from the buoyant jet to beyond the near field (see e.g. Jirka and Harleman 1979), and also the difference between minimum and average dilution.

It should be pointed out that using the computed relations for the layer-averaged velocities u_t and u_b in the inviscid model of Koh (1983) would have resulted in a surface layer thickness of h/d = 0.24 - at odds with the experiments. It is believed that this discrepancy is related to the questionable validity of the assumption of an energy-conserving buoyant surface layer of uniform density. Further detailed experiments to resolve this issue would be most worthwhile.

Besides the bulk characteristics, the coupled model simulates the evolution process of the gravitational spreading and provides the detailed time-varying flow field and density distribution (Fig. 4.15 - Fig. 4.18).

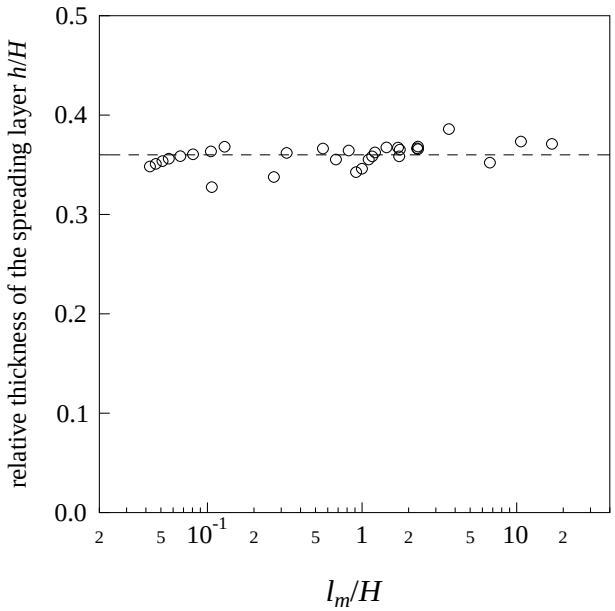

Figure 4.13: Relative thickness of the spreading layer vs. l_m/H.

Finally, to examine the difference between the source representation by 2D and 3D buoyant jet, the computed entrained flows are compared (Fig. 4.21). It can be seen that the computed entrained flows using the two kinds of source representation are not significantly different. However, for the "jet-like" case, the differences are greater especially when closer to the discharge point (Fig. 4.22). Also, it can be seen that the computed entrained flows computed by DESA are found to be much smaller than the entrainment flows computed from PLANEJET (and VISJET). It may indicate that the momentum effect of the discharge has not been properly represented by DESA.

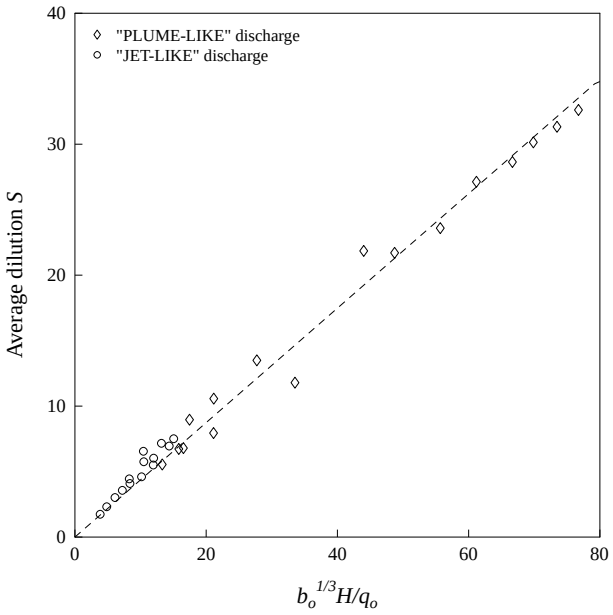

Figure 4.14: Computed average dilution in the spreading layer.

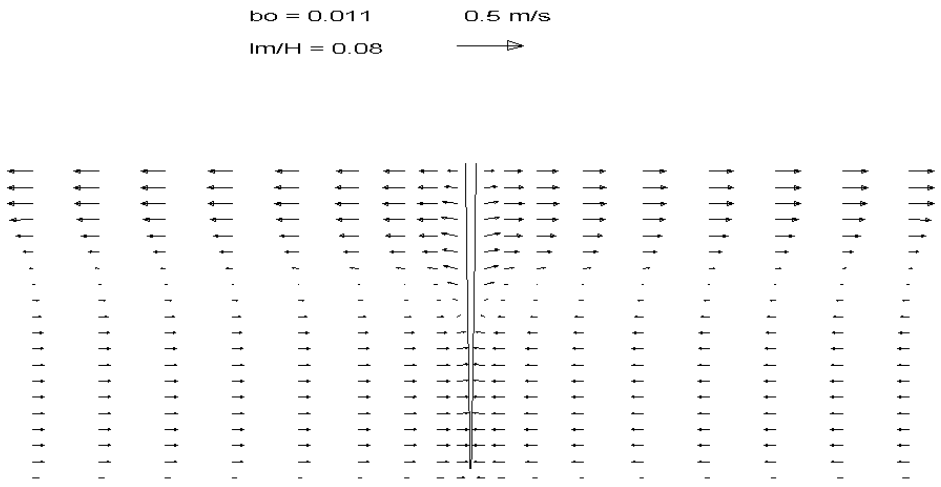

Figure 4.15: Computed velocities in the vertical section across the discharge point for a plane vertical "plume-like" buoyant jet in uniform ambient.

Table 4.2: Experimental parameters for plane vertical buoyant jet in stagnant uniform water

q_o (m^2/s)	$g' = g\Delta\rho^*$ (m/s^2)	H (m)	m_o (m^3/s^2)	b_o (m^3/s^3)	$l_m/H = (m_o/b_o^{2/3})/H$
1.0	0.00364	25	10.0	0.00362	16.903
1.0	0.00728	25	10.0	0.00728	10.658
0.1	0.07400	25	0.1	0.00740	0.105
0.6	0.01456	25	3.6	0.00874	3.395
0.1	0.11046	25	0.1	0.01105	0.081
0.8	0.01456	25	6.4	0.01165	4.982
1.0	0.01456	25	10.0	0.01456	6.708
0.1	0.14660	25	0.1	0.01466	0.067
0.1	0.18967	25	0.1	0.01897	0.056
0.1	0.21821	25	0.1	0.02182	0.051
0.1	0.21821	12	0.1	0.02182	0.107
0.1	0.25375	25	0.1	0.02538	0.046
0.1	0.28918	25	0.1	0.02892	0.042
1.0	0.03637	25	10.0	0.03637	3.644
0.2	0.21821	25	0.4	0.04364	0.129
0.2	0.21821	12	0.4	0.04364	0.269
1.0	0.07269	25	10.0	0.07269	2.297
1.0	0.07400	25	10.0	0.07400	2.269
0.4	0.21821	25	1.6	0.08728	0.325
0.4	0.21821	12	1.6	0.08728	0.678
1.0	0.10898	25	10.0	0.10898	1.753
1.0	0.11046	25	10.0	0.11046	1.738
0.6	0.21821	25	3.6	0.13092	0.558
0.6	0.21821	12	3.6	0.13092	1.164
1.0	0.14660	25	10.0	0.14660	1.439
0.8	0.21801	25	6.4	0.17456	0.820
0.8	0.21801	12	6.4	0.17456	1.708
1.0	0.18967	25	10.0	0.18967	1.212
1.0	0.21821	25	10.0	0.21821	1.104
1.0	0.21821	12	10.0	0.21821	2.299
1.0	0.25375	25	10.0	0.25375	0.998
1.0	0.28918	25	10.0	0.28918	0.914

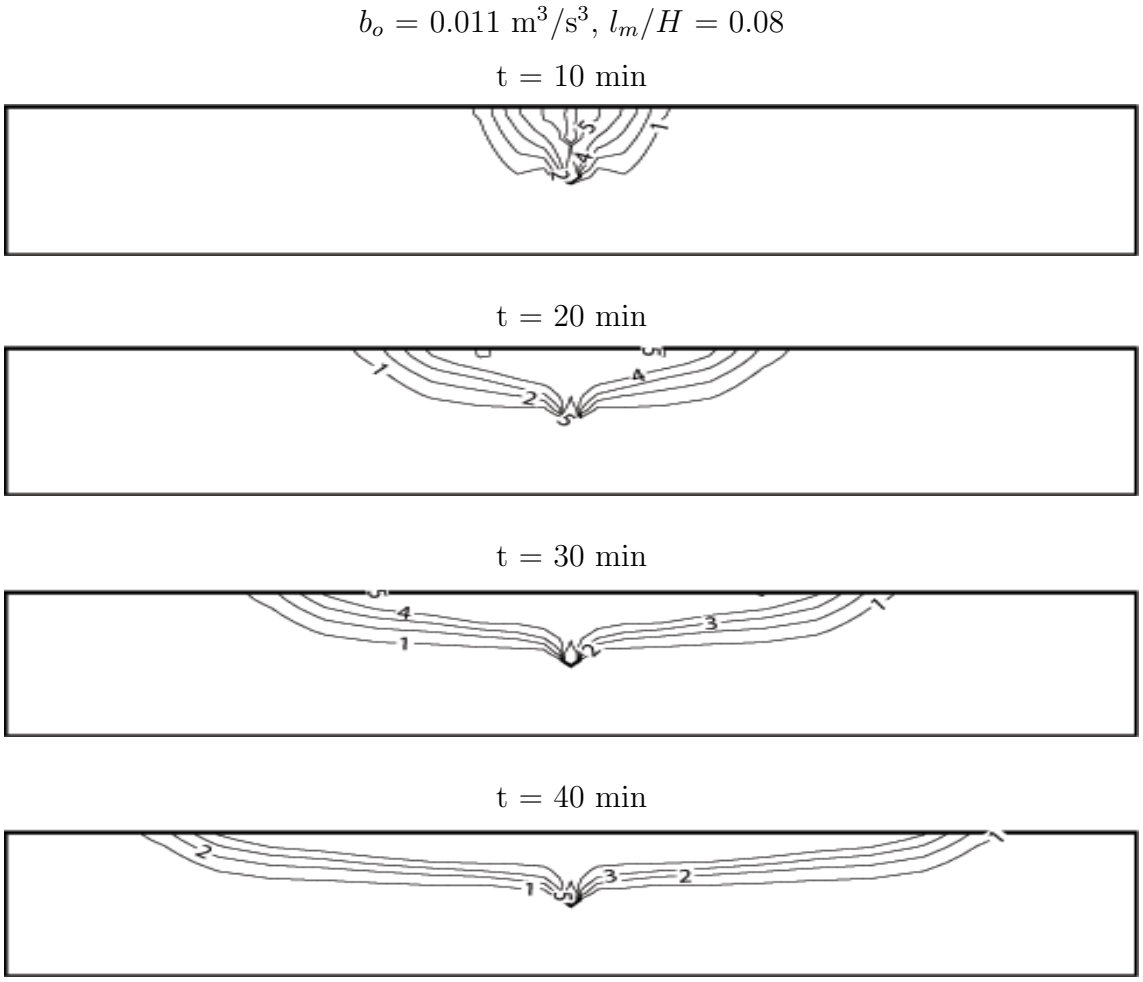

Figure 4.16: Computed tracer concentration distribution in the vertical section across the discharge point for a plane vertical "plume-like" buoyant jet in uniform ambient at selected times (contour in $0.01C_o$).

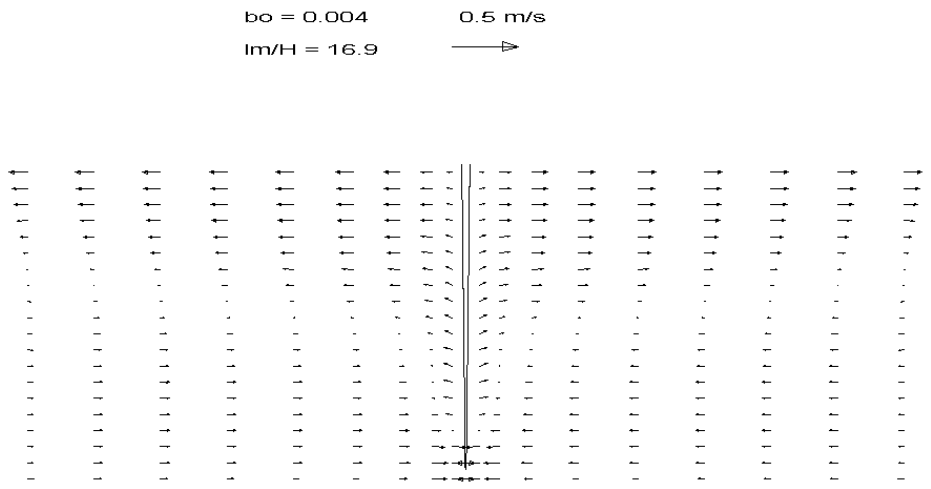

Figure 4.17: Computed velocities in the vertical section across the discharge point for a plane vertical "jet-like" buoyant jet in uniform ambient.

Table 4.3: Entrainment flows and dilutions obtained from different methods

b_o (m^3/s^3)	$Q_o = q_o \Delta y$ (m^3/s)	$(S - 1)Q_o$ with $S = 2u_t\ h/q_o$ (m^3/s)	Entrainment flow up to bottom of the spreading layer computed by JETLAG (m^3/s)	Entrainment flow in the bottom layer (far field model) at $x = 4\Delta x$ (m^3/s)	Computed minimum dilution S	Average dilution at bottom of spreading layer (standalone JETLAG)	Average dilution at water surface (standalone JETLAG)
0.022	1.0	29.17	29.63	30.36	30.17	27.65	34.62
0.044	2.0	38.73	37.60	37.77	20.36	18.86	23.61
0.087	4.0	49.68	49.88	49.77	13.42	13.33	16.59
0.131	6.0	58.04	59.00	58.54	10.67	11.42	13.95
0.175	8.0	64.22	64.05	62.92	9.03	10.56	12.73
0.218	10.0	66.91	67.65	66.49	7.69	10.11	12.07

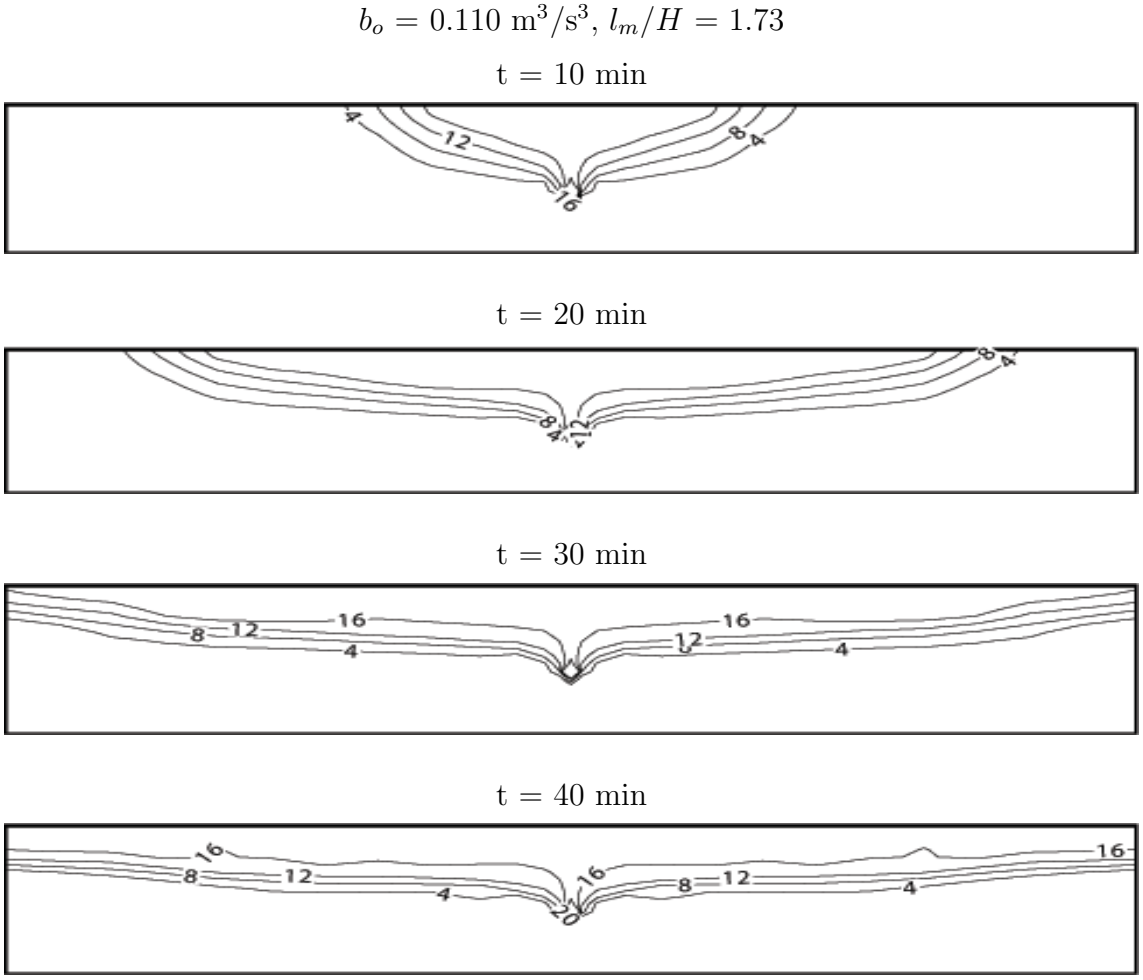

Figure 4.18: Computed tracer concentration distribution in the vertical section across the discharge point for a plane vertical "jet-like" buoyant jet in uniform ambient at selected times (contour in $0.01C_o$).

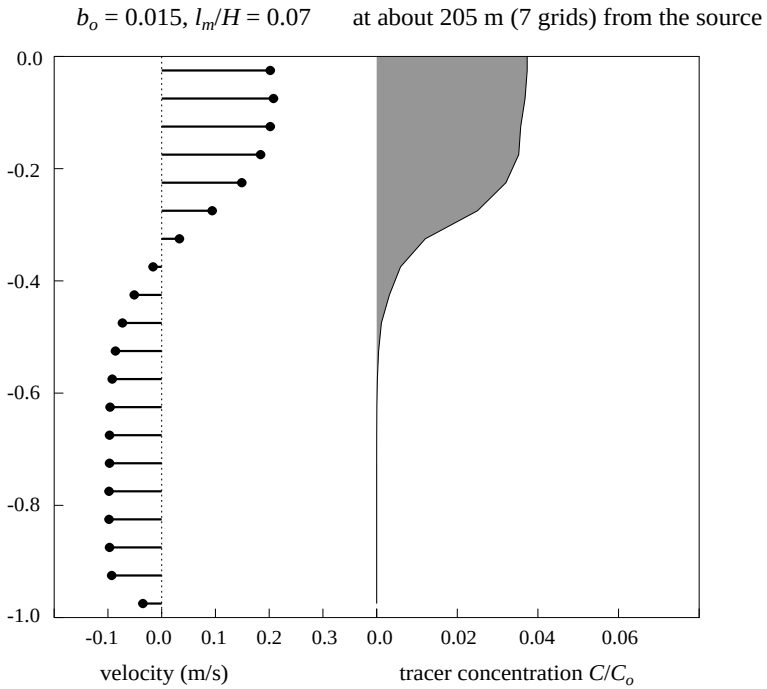

Figure 4.19: Velocities and tracer concentration profiles in the vertical section across the discharge point for a plane vertical "plume-like" buoyant jet in uniform water.

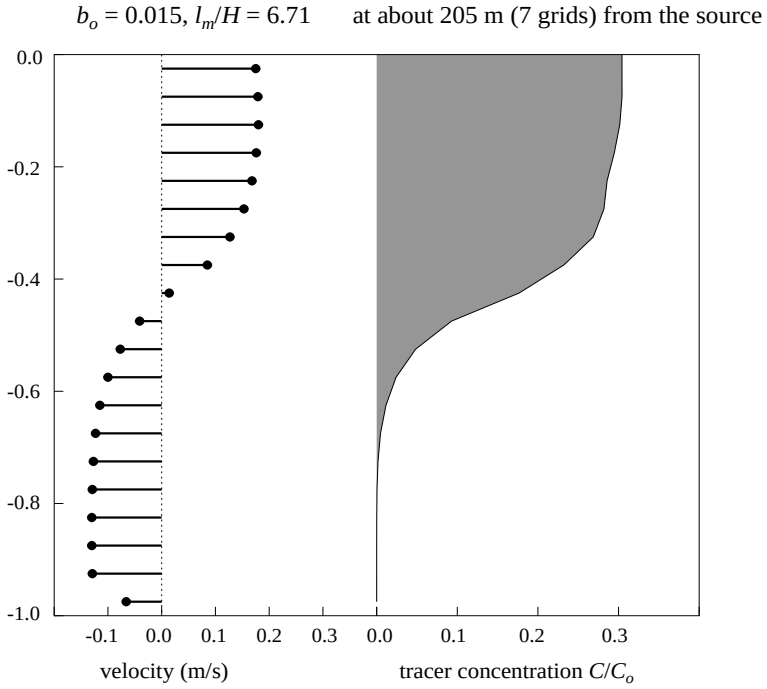

Figure 4.20: Velocities and tracer concentration profiles in the vertical section across the discharge point for a plane vertical "jet-like" buoyant jet in uniform water.

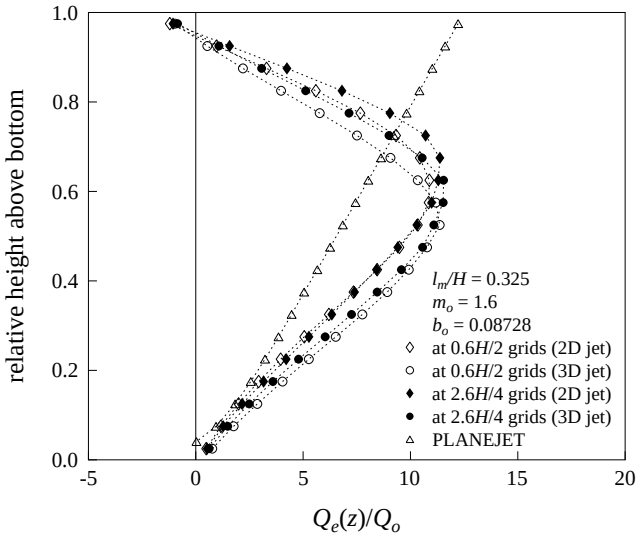

Figure 4.21: Computed entrainment flow for a "plume-like" discharge ($l_m/H = 0.325$).

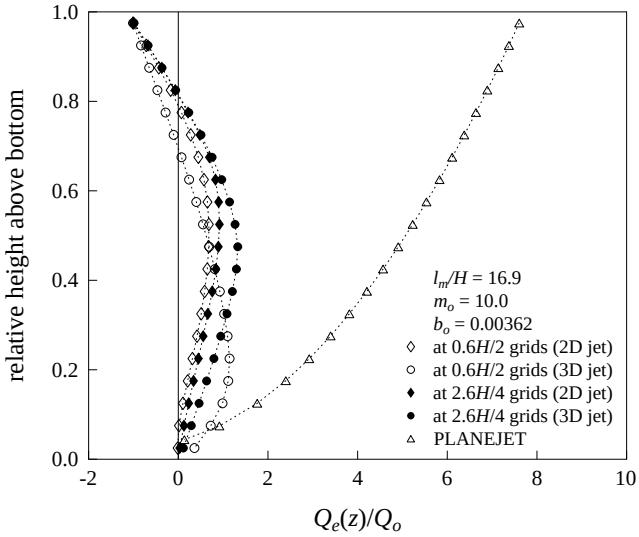

Figure 4.22: Computed entrainment flow for a "jet-like" discharge ($l_m/H = 16.9$).

4.2 Plane buoyant jet in linearly stratified water

4.2.1 Vertical plane buoyant jet in linearly stratified fluid

A series of nine numerical experiments is carried out to simulate the behaviours of the plane vertical buoyant jet in linearly stratified water based on the experiments carried out by Wallace and Wright (1984). The unit discharge flow (per unit width) q_o ranges from 5.46 to 9.70 cm^2/s, while the relative initial density difference $\Delta\rho^*$ varies from 0.060 to 1.846. The water depth H for all cases is 0.92 m and the stratification parameter

$$\epsilon = -\frac{g}{\rho_{ao}}\frac{d\rho_a}{dz}$$

ranges from 0.047 to 0.156. A 13 x 1 x 20 non-uniform model grid. The slot diffuser is represented either by a 2D plane jet (PLANEJET) or two non-interfering 3D round jets (JETLAG) with equivalent initial volume, momentum and buoyancy fluxes. The initial unit buoyancy flux b_o = 5.52 - 175.57 cm^3/s^3 and initial momentum flux m_o = 34.3 - 325 cm^3/s^2 (Table 4.4). Time step used is 0.05 sec. (with maximum Courant no. Cr about 0.48). $l_m = m_o/b_o^{2/3}$ and $l'_b = b_o^{1/3}/\epsilon^{1/2}$ are two key length scales of concern in the study.

Table 4.4: Experimental parameters for plane vertical buoyant jet in linearly stratified water

q_o (cm^2/s)	g' (cm/s^2)	ϵ (s^{-2})	m_o (cm^3/s^2)	b_o (cm^3/s^3)	l_m (m)	l'_b (m)	l_m/l'_b
5.46	12.7	0.0660	34.3	69.34	0.0203	0.1599	0.13
9.70	18.1	0.1560	108.0	175.57	0.0345	0.1418	0.24
5.56	4.85	0.0475	35.9	26.97	0.0400	0.1376	0.29
5.49	4.54	0.0613	34.6	24.93	0.0406	0.1180	0.34
5.52	3.72	0.0561	35.0	20.53	0.0467	0.1156	0.40
5.61	1.75	0.0705	36.2	9.82	0.0789	0.0806	0.98
5.49	1.58	0.1230	215.0	8.67	0.5100	0.0586	8.70
9.54	0.59	0.0470	325.0	5.63	1.0272	0.0821	12.52
9.36	0.59	0.0820	283.0	5.52	0.9046	0.0617	14.65

Unlike the case for the buoyant jet in uniform ambient water, the induced velocity field by the buoyant jet in a linearly stratified water is more complicated, and there may exist more than one plane of zero velocity (Fig. 4.23 - 4.24). Therefore, the tracer concentration contour of $0.01C_o$ is used to define the boundary of the trapped spreading layer (Fig. 4.25 - 4.26).

Fig. 4.27 - 4.28 show the computed maximum height of rise Z_M and the minimum dilution at the spreading layer S_M (obtained from the maximum concentration in the spreading layer at a distance about Z_M from the discharge point), plotted against l_m/l'_b. As the experimental tank has a finite length, the spreading layer can only grow to the two ends of the tank before it will be thickened, therefore, the dilution is determined before the edge of spreading layer ($0.01C_o$ contour) reaches the ends of the tank. For buoyancy-dominated jets or plumes, $l_m/l'_b \ll 1$, the computed maximum height of rise Z_M/l'_b is approximately constant and slightly greater than 3.6. For momentum-dominated jets, a 1/3 power dependence is confirmed; the predicted

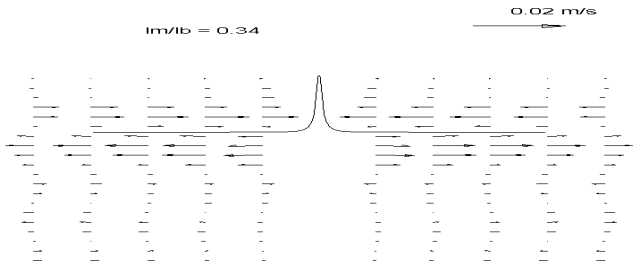

Figure 4.23: Computed velocities in the vertical section across the discharge point for a plane vertical "plume-like" (negatively) buoyant jet in linearly stratified water.

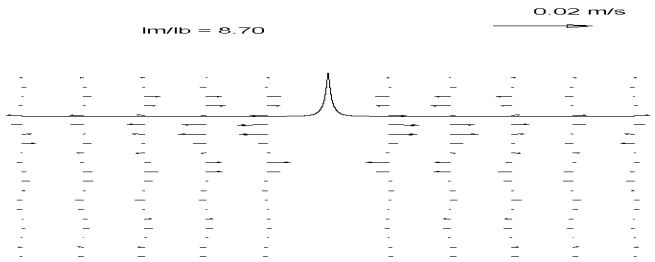

Figure 4.24: Computed velocities in the vertical section across the discharge point for a plane vertical "jet-like" (negatively) buoyant jet in linearly stratified water.

maximum rise is somewhat higher than the observations. The computed dimensionless minimum dilution in the spreading layer $S_M q_o / {b_o}^{1/3} l'_b$ is found to agree well with the experimental data of Wallace and Wright (1984). For a plume, it is found to be around 0.88, while the 2/3 power dependence is confirmed for momentum jets ($S_M q_o / {b_o}^{1/3} l'_b = 0.59 (l_m / l'_b)^{2/3}$). It should be pointed out the exact time and x-location at which the reported maximum height of rise and minimum dilution are measured are not known. This precludes a detailed comparison of the computed spreading layer characteristics with the data (as the ambient stratification undergoes continuous change with time in the laboratory tank of limited size - see later discussion).

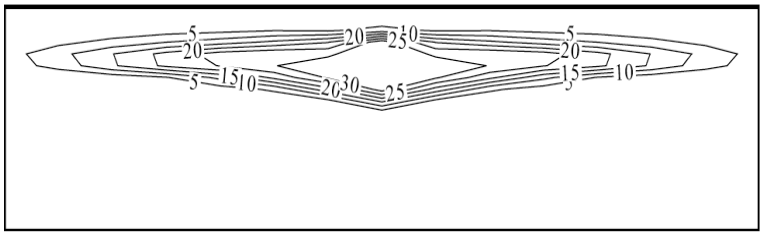

Figure 4.25: Computed tracer concentrations in the vertical section across the discharge point for a plane vertical "plume-like" (negatively) buoyant jet in linearly stratified water.

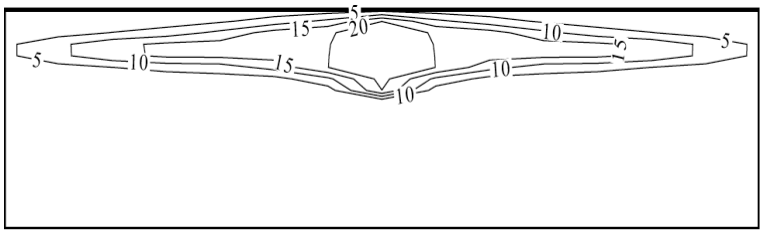

Figure 4.26: Computed tracer concentrations in the vertical section across the discharge point for a plane vertical "jet-like" (negatively) buoyant jet in linearly stratified water.

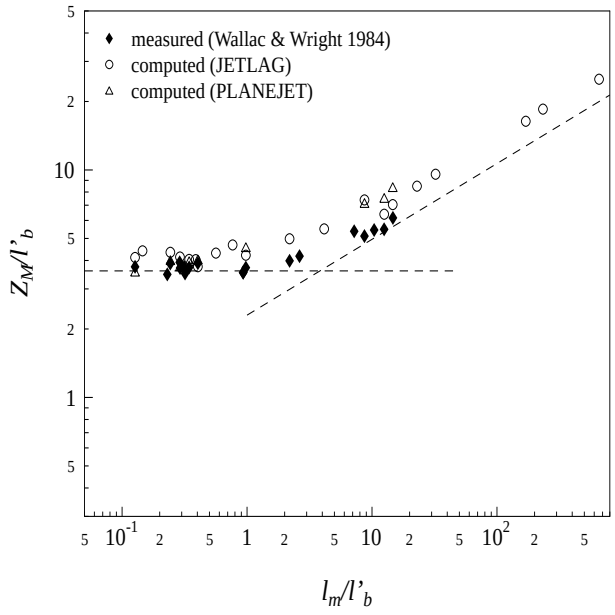

Figure 4.27: Dimensionless maximum height of rise Z_m in spreading layer for plane buoyant discharge into a linearly stratified fluid as function of l_m/l'_b.

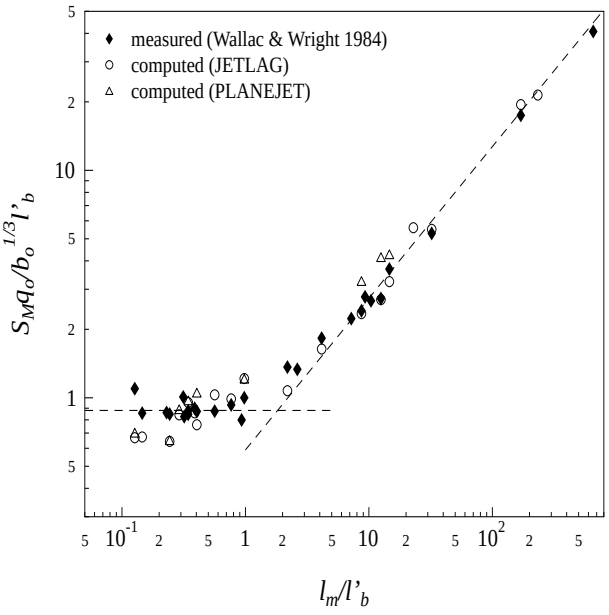

Figure 4.28: Dimensionless maximum height of rise S_M in spreading layer for plane buoyant discharge into a linearly stratified fluid as function of l_m/l'_b.

4.2.2 Inclined plane buoyant jet in linearly stratified fluid

Lee and Cheung (1986) studied the mixing of a negatively buoyant slot jet in a linearly stratified fluid in a laboratory tank of 3 m long, 0.328 m wide by 0.76 m deep (Fig. 4.29). A wooden partition was installed in the middle along the length of the tank to create an effective section with length of 6 m and width of 0.152 m. In addition to the maximum height of rise and the tracer concentration distribution in the spreading layer, the change in the ambient stratification caused by the jet discharge in the finite tank was also measured in the experiments (Lee and Cheung, unpublished). A 21 x 3 x 20 model grid with closed boundaries at four sides is employed. The horizontal grid sizes are non-uniform in the y-direction to account for the existence of the partition. The model is cold started with a time step of 0.05 sec. (with maximum $Cr \approx 0.88$) and run for a duration of 5 minutes, similar to the length of experiment.

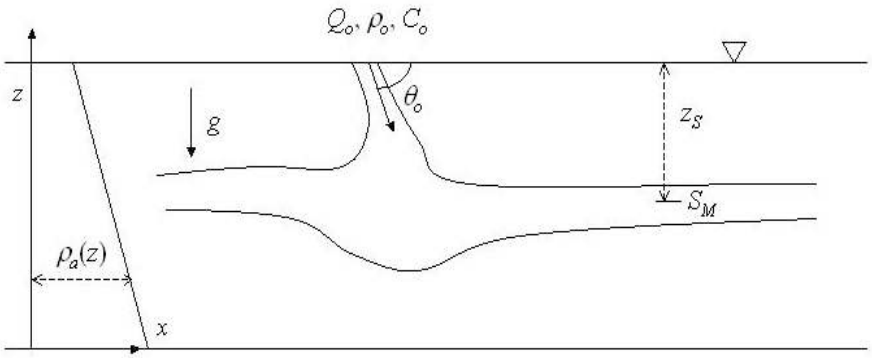

Figure 4.29: Inclined plane negatively buoyant jet in linearly stratified fluid.

Fig. 4.30 - 4.33 shows the predicted change in ambient density profiles are in good agreement with the experimental data for different kinds of discharges. Fig. 4.34 shows the predicted minimum dilution S_M in the spreading layer of a plane buoyant jet with different initial momentum and buoyancy fluxes. The predicted dimensionless dilutions as a function of l_m/l'_b, where $l_m = m_o/b_o^{2/3}$ and $l'_b = b_o^{1/3}/\epsilon^{1/2}$ are in good agreement with the experimental data. Again the dimensionless minimum dilution is roughly a constant for "plume-like" discharge, $l_m/l'_b < 1$, with a characteristic 2/3 power dependence for "jet-like" discharges, $l_m/l'_b \gg 1$. As a comparison, the AS method generally predicts lower plume trapping levels and hence lower dilution S_M.

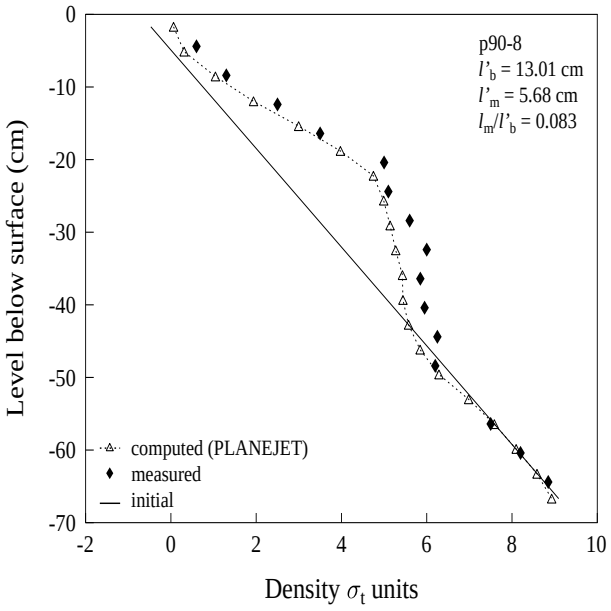

Figure 4.30: Ambient density profiles before and after a vertical "plume-like" discharge into a linearly stratified fluid.

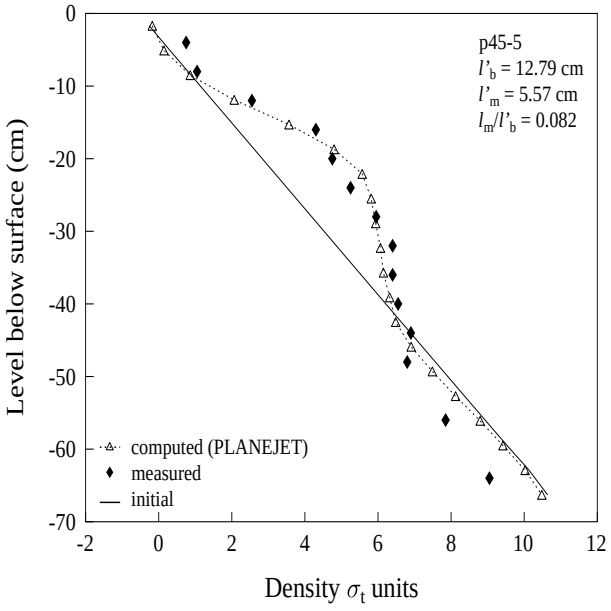

Figure 4.31: Ambient density profiles before and after a 45° "plume-like" discharge into a linearly stratified fluid.

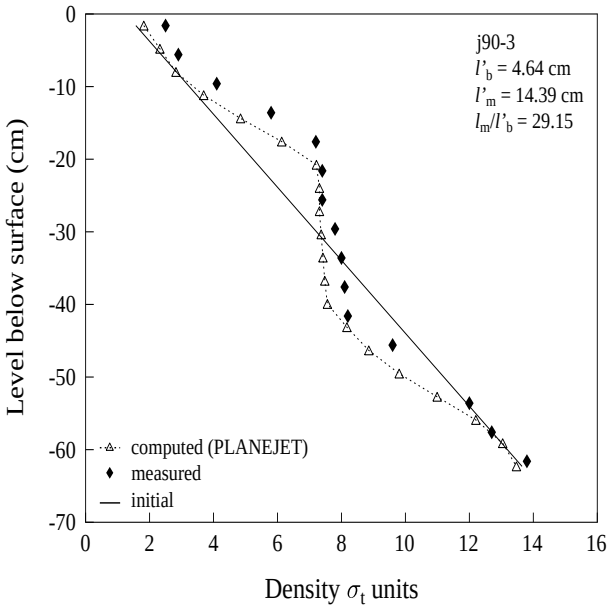

Figure 4.32: Ambient density profiles before and after a vertical "jet-like" discharge into a linearly stratified fluid.

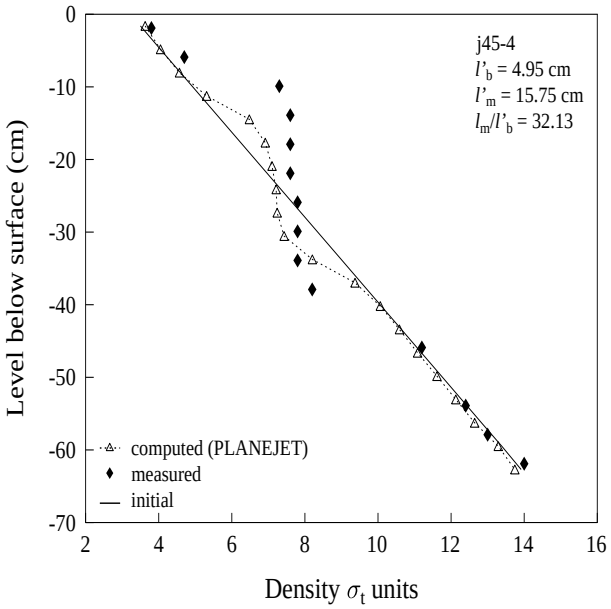

Figure 4.33: Ambient density profiles before and after a 45° "jet-like" discharge into a linearly stratified fluid.

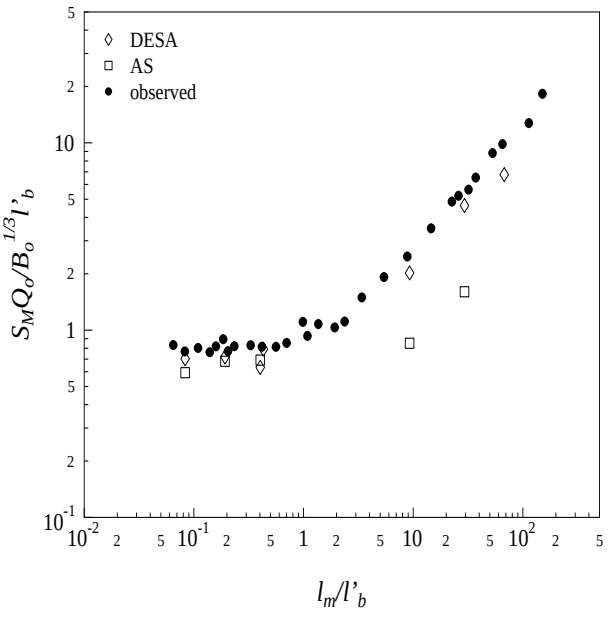

Figure 4.34: Comparison of computed and measured minimum dilution S_M in spreading layer for vertical plane buoyant jet in linearly stratified fluid.

Chapter 5

Discharges in Crossflow

5.1 Line plume in uniform crossflow

Roberts (1977, 1979) performed experiments in a 6.1 m wide by 11.0 m long rectangular basin with a slot diffuser discharge in a steady current (Fig. 5.1). Experiments were carried out for a wide range of current speed U_a and discharge buoyancy flux b per unit length. Experiments were carried out for a wide range of current speed U_a and discharge buoyancy flux b per unit length. The experiments show that the near field dilution is governed by a cross flow Froude number, $F = U_a^3/b$, representing the ratio of ambient velocity to buoyancy-induced velocity. Small values of F indicate a buoyancy-dominated flow, resulting in the formation of a buoyant surface wedge with an initial width greater than the diffuser length. On the other hand, high values of F represent a flow dominated by the ambient current. For this case, a 23 x 17 x 20 model grid with open boundaries at two ends, a horizontal grid size of 43.5 cm by 30.5cm and 20 uniform vertical layers is employed. The model is run to generate a steady state current field first before the line plume is applied and the time step ranges from 0.01 sec. to 0.05 sec. (with maximum $Cr \approx 0.15$). Small time step is found to be needed to ensure that $w\Delta t/\Delta z \leq 1$ (w = vertical velocity) for the cases with source/sink terms introduced to multiple neighbouring water columns. The finite line plume of length $L = 0.61$ m is represented by a number (n) of equivalent non-interfering round plumes (preserving the same volume, momentum, and buoyancy fluxes per unit diffuser length). The number can be determined from the jet simulations, and $n = 4$ to 6 are required for the present case.

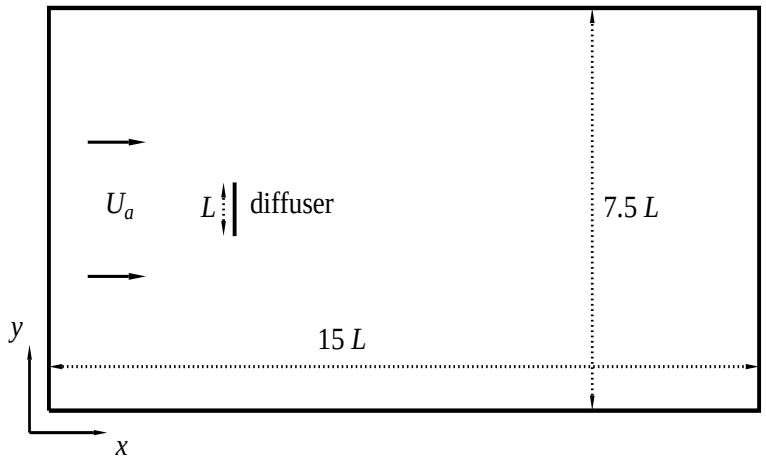

Figure 5.1: The schematic setup of the finite line plume in a perpendicular crossflow experiment.

In Fig. 5.2, the observed surface waste-field pattern is compared with the predicted surface concentration contours for three representative flow situations, with $F \approx 0.13$, 1.3, and 11.4 (corresponding respectively to experiment H5, H4, and H3 in Roberts 1977). Fig. 5.3 shows the corresponding computed concentration field in a vertical section in the centreline plane of symmetry. The DESA predictions are very similar to the experimental observations: (i) With $F \sim 0.1$, the mixed effluent has a plume-like pattern, with a surface buoyant layer and significant lateral spread. The surface width at the diffuser is larger than the diffuser length; both the extent of the upstream intrusion and the lateral width are well-supported by the observations. (ii) As F increases, the surface buoyant layer is swept downstream; the lower surface concentrations for $F \geq 1$ indicates bottom attachment of the effluent field. (iii) For $F \sim 10$ the flow is advection-dominated and the lateral spread of the surface field is very limited.

Fig. 5.4 shows the predicted dimensionless minimum surface dilution $S_M q/U_a H$ (inferred from the maximum concentrations in the surface layer) for three diffuser orientations to the current: $\theta = 90°$ (perpendicular alignment), 45° and 0° (parallel alignment). It can be seen that the predicted dilution (computed using averaging method (i)) agrees well with the asymptotic dilution equation (best fit of data) given by Roberts (1979), where $q_o = Q_o/L$ is the unit discharge. On the other hand, the actual source method (for the perpendicular alignment) is seen to over-predict initial dilution. In addition, similar results are obtained with the ambient concentrations computed by (i) averaging values in all the surrounding cells as indicated in Fig. 2.5 and (ii) averaging only those in the "upwind" cells Fig. 5.5).

The different features of the waste-field pattern corresponding to different F can also be observed from the vertical sections downstream to the diffuser (Fig. 5.6, 5.7, 5.8). Overall, the predicted flow features agree well with the observations in Roberts (1977); the computed length of bottom attachment is also broadly similar to the reported values. The predicted shape of surface field by the AS method is similar to that of DESA; however the AS method cannot reproduce the buoyant layer close to the near field.

The lateral spreading characteristics have also been studied quantitatively. the buoyant surface spreading rate, $\Delta W/L(= (W - L)/L)$ can be shown to grow as a function of x/L. Roberts (1977) has found that the surface width follows different growth rates for different downstream regimes: linear, 2/3 power and 1/5 power law with increasing distance downstream. Taking the $0.01C_o$ contour line as the plume boundary, the plume width W can be determined from the computed results. The results indicate clearly that for $F \sim 0.1$, the computed slope for both DESA and AS is 1/5 as predicted (Fig. 5.9). For $F \sim 1$, the slope obtained by DESA is about 2/3, which agrees with the theoretical value (Roberts 1977), while that obtained by AS is much smaller (only about 0.42). With $F \sim 10$, the computed surface width growth rates computed by DESA follows the theoretical rates of 1 (linear), 2/3 and 1/5 slope quite well, whereas the AS method uniformly underpredicts the lateral spreading rate for this current-dominated case.

In Fig. 5.10 - 5.12, the normalized vertical profile of tracer concentration along the centerline, $CU_a H/q_o$, is compared with data at different downstream locations. It can be seen that the DESA method predicts the tracer concentration field in the spreading layer quite well, while the AS method tends to predict exaggerated vertical mixing.

To test the effect of different source representation, simulations with a model grid with refined grid cells (halving the grid size in both x- and y-direction) around the line diffuser have been performed. The results (not shown) reveal that there is no significant difference between the

two cases except in the intermediate neighbourhood of the discharge.

To study the effect of using different near field models, simulations using the PLANEJET instead of JETLAG are also carried out. Line source covering two grid cells are employed. As shown in Fig. 5.13, it is found that this approach works satisfactorily for cases with $F \leq 0.1$ but under-predicts the dilution for cases with greater F. In general, the results suggest the use of a number of equivalent non-interfering round plumes to simulate the finite line plume.

Further simulations are then conducted with different source representations by distributing the 3D or 2D jets non-uniformly over three grid cells (whilst keeping the same diffuser length L) instead of uniformly over two grid cells. It is found that the results are rather similar and no significant difference is found.

To test that the DESA method will work equally well for prototype scale. It is used to simulate three field study cases described in Roberts (1977). As limited results are provided, so only the minimum surface dilution S_M is compared. For the three cases, the ambient current is approximately perpendicular to the line diffuser and the ambient density is assumed to be uniform initially. As shown in Table 5.1, the dilutions predicted by the DESA method compare quite well with the field measurements for all three cases, while the AS method significantly over-predicts the dilution for the two cases for the outfall at Samoa, California.

Table 5.1: Experiment results from field experiments on surface plumes given in Table 6.2 of Roberts (1977)

Location	Q_o (m^3/s)	H (m)	L (m)	U_a (m/s)	F	S_M (field)	S_M (DESA)	S_M (AS)
Gardiner, OR	0.632	7.6	55.5	0.08	0.20	45	32.6	38.3
Samoa, CA	1.172	9.1	152.4	0.14	1.52	56	50.6	114.8
Samoa, CA	1.042	9.1	152.4	0.15	2.36	56	51.4	131.8

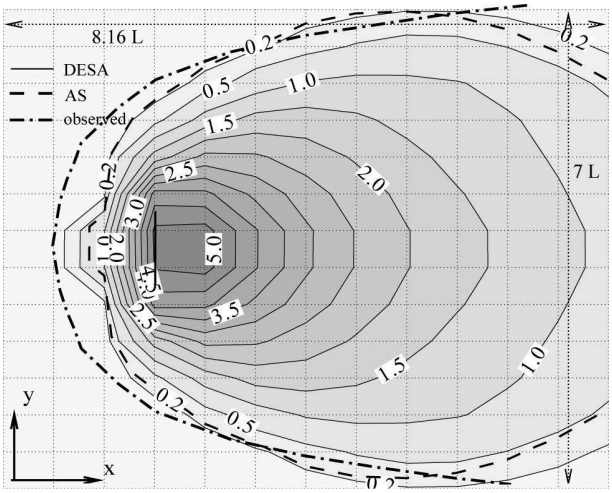

a) $F \sim 0.1$

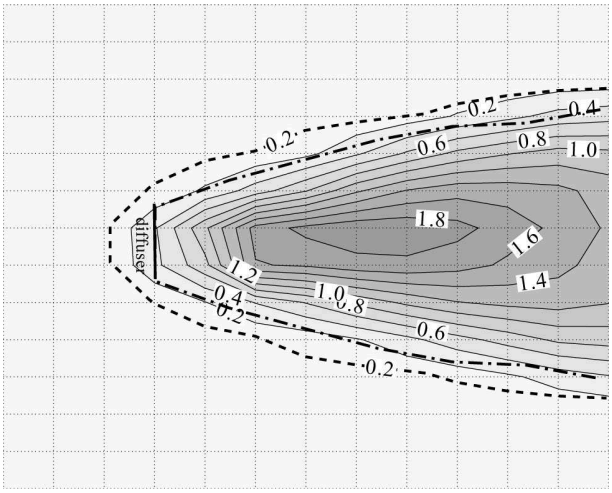

b) $F \sim 1.0$

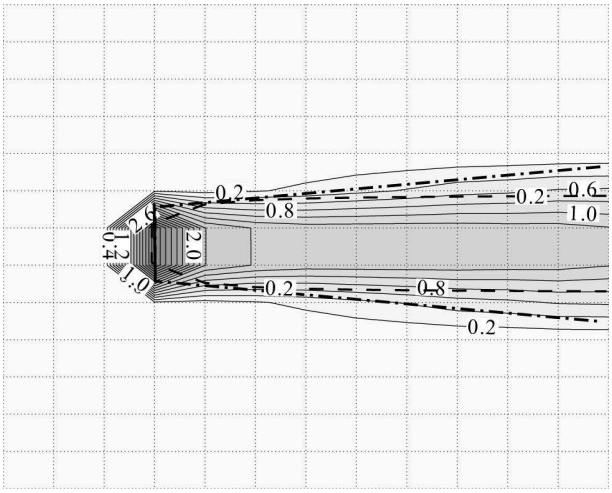

c) $F \sim 10.0$

Figure 5.2: Computed surface tracer concentration field (in units of $0.01C_o$) and observed surface field for a finite line plume in a perpendicular crossflow.

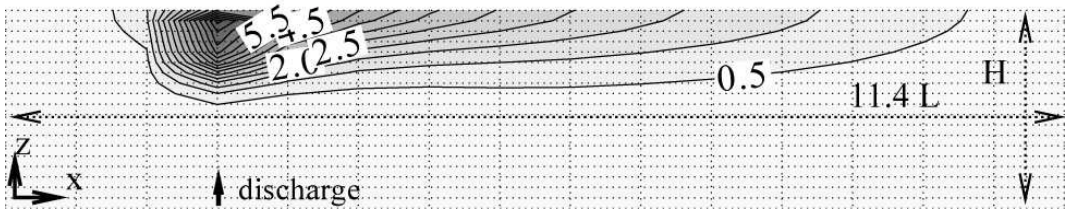

a) $F \sim 0.1$

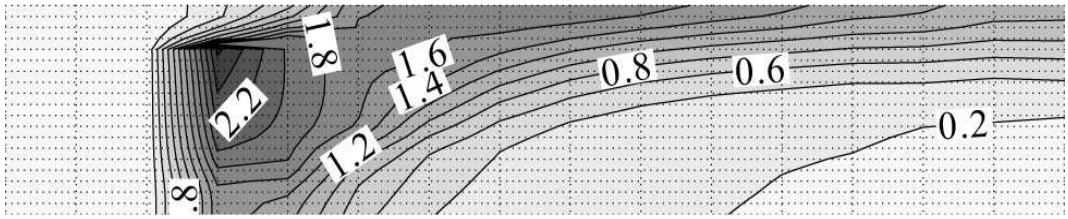

b) $F \sim 1.0$

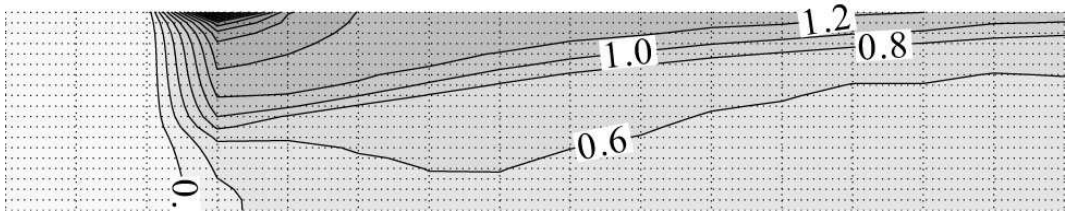

c) $F \sim 10.0$

Figure 5.3: Computed tracer concentration field for a vertical section in the plane of symmetry for finite line plume in a perpendicular crossflow (concentration in $0.01C_o$).

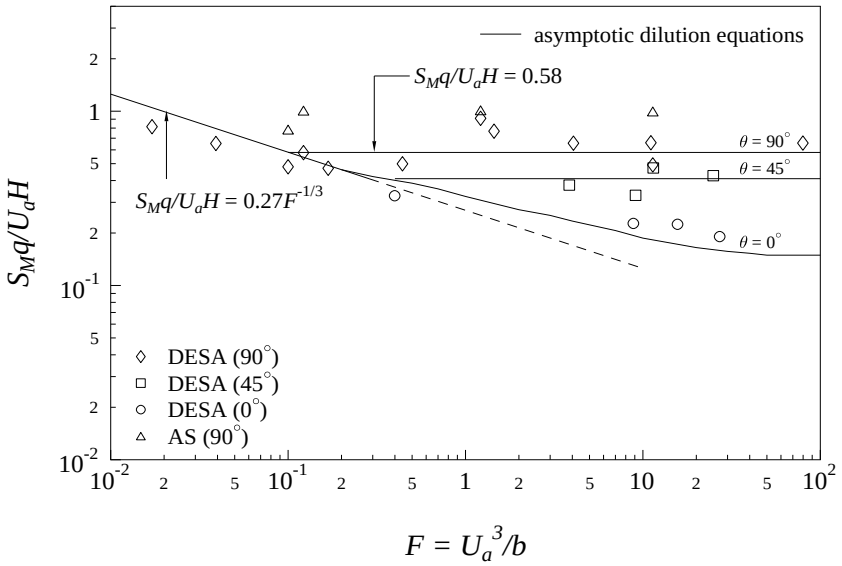

Figure 5.4: Computed minimum surface dilution as a function of crossflow Froude number F (symbols with coupling method indicated). Best fit of experimental data shown as asymptotic dilution equation (solid line).

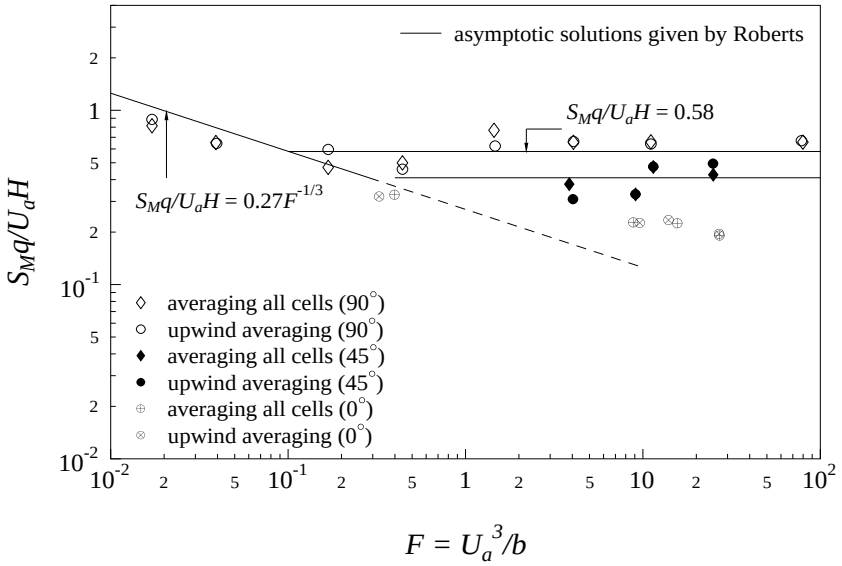

Figure 5.5: Computed minimum surface dilution as a function of crossflow Froude number F (symbols with ambient concentration computing methods indicated). Best fit of experimental data shown as asymptotic dilution equation (solid line).

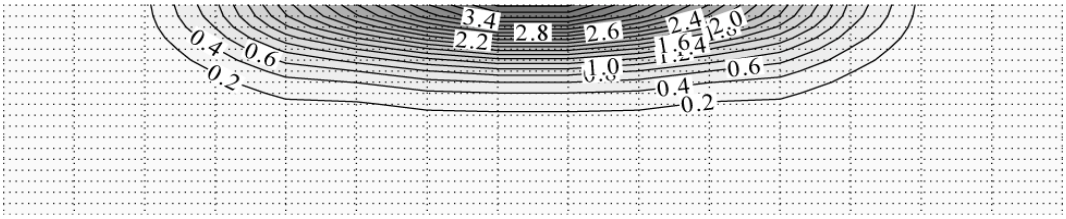

a) $x = 1.4L$

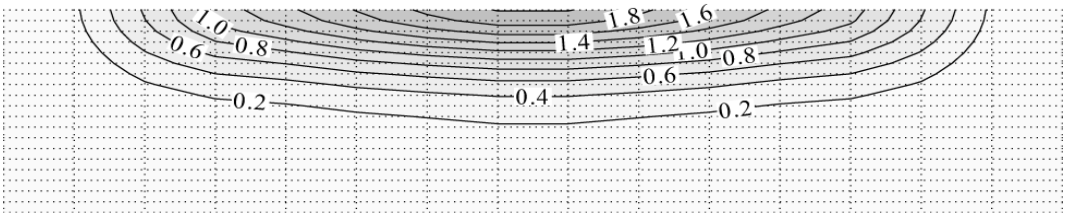

b) $x = 3.6L$

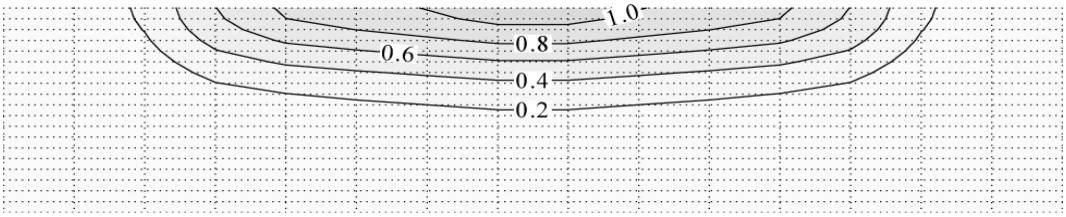

c) $x = 5.7L$

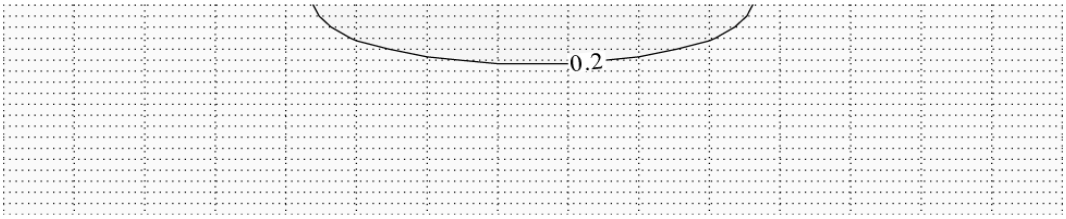

d) $x = 7.8L$

Figure 5.6: Computed tracer concentration field for vertical sections parallel to the line source in a perpendicular crossflow for $F \approx 0.13$ using DESA (concentration in $0.01C_o$).

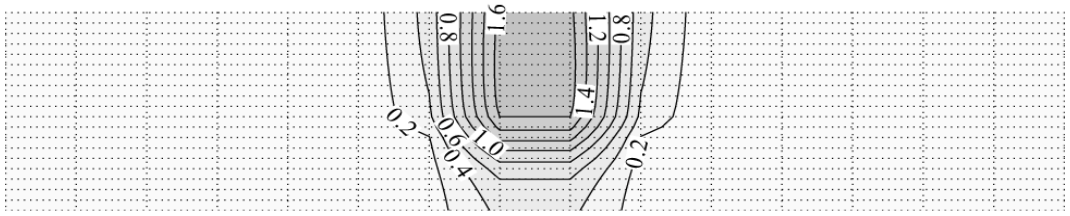

a) $x = 1.4L$

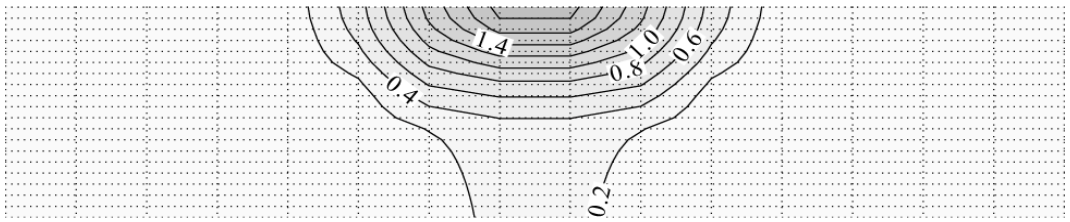

b) $x = 3.6L$

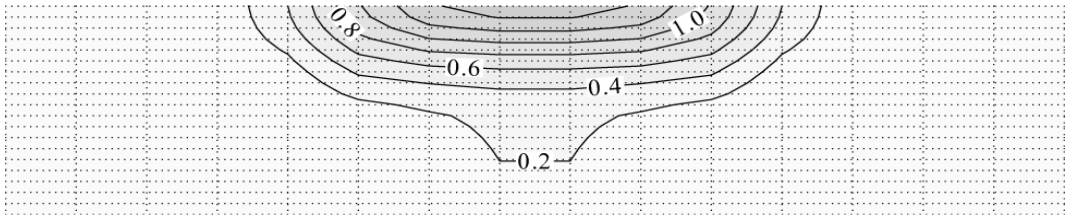

c) $x = 5.7L$

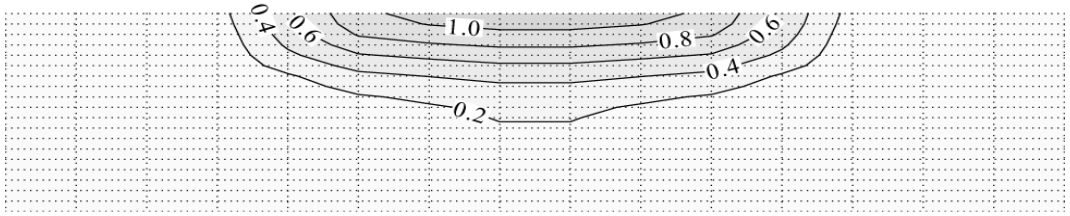

d) $x = 7.8L$

Figure 5.7: Computed tracer concentration field for vertical sections parallel to the line source in a perpendicular crossflow for $F \approx 1.3$ using DESA (concentration in $0.01C_o$).

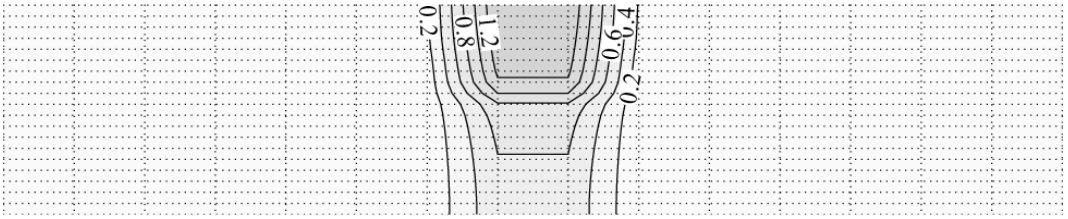

a) $x = 1.4L$

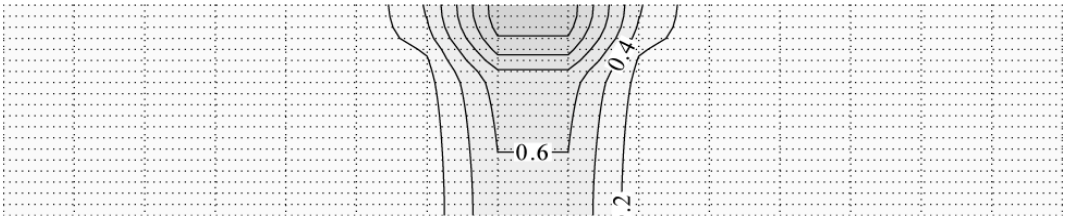

b) $x = 3.6L$

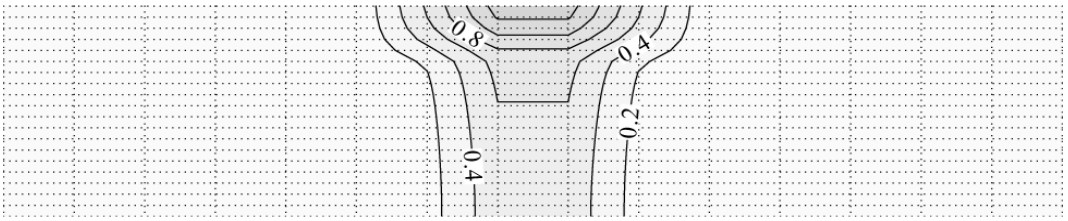

c) $x = 5.7L$

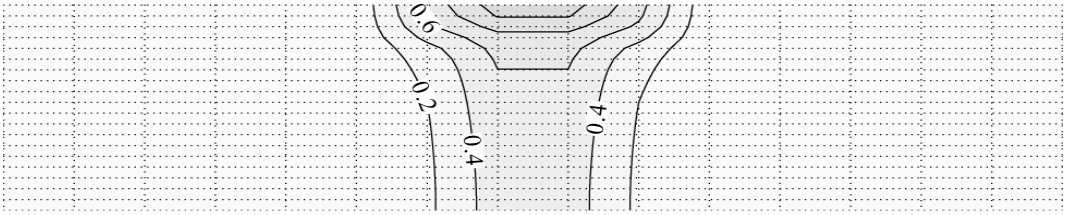

d) $x = 7.8L$

Figure 5.8: Computed tracer concentration field for vertical sections parallel to the line source in a perpendicular crossflow for $F \approx 11.4$ using DESA (concentration in $0.01C_o$).

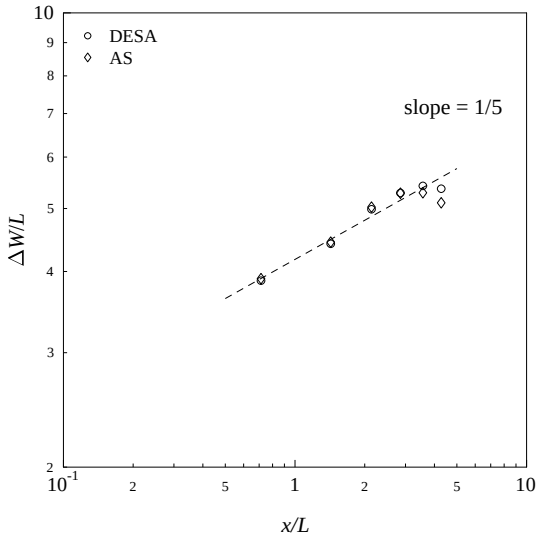

a) $F \sim 0.1$

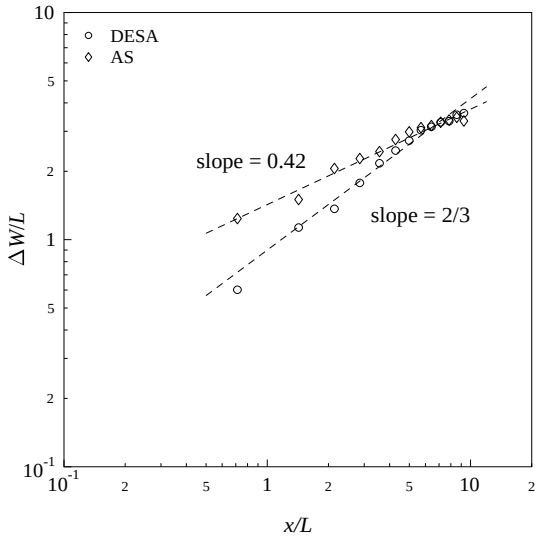

b) $F \sim 1.0$

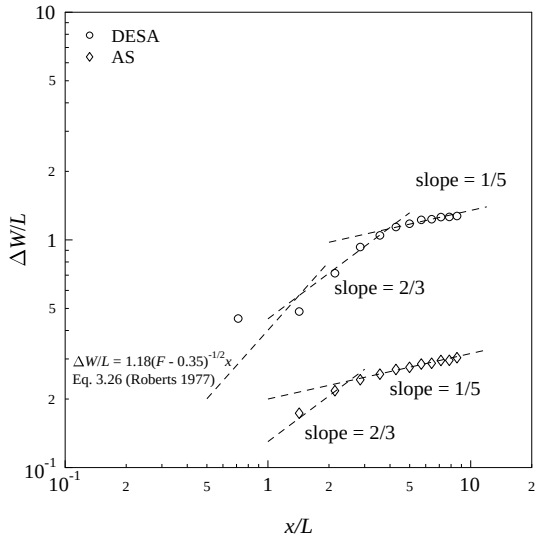

c) $F \sim 10.0$

Figure 5.9: Growth of surface field downstram for a finite line plume in a perpendicular cross-flow.

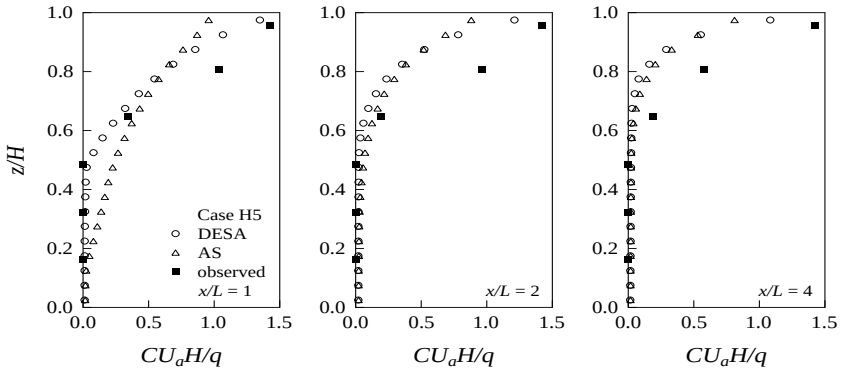

Figure 5.10: Normalized vertical profiles of tracer concentration (C) along centreline for perpendicular flow alignment, for $F = 0.13$ (Case H5 in Roberts 1977).

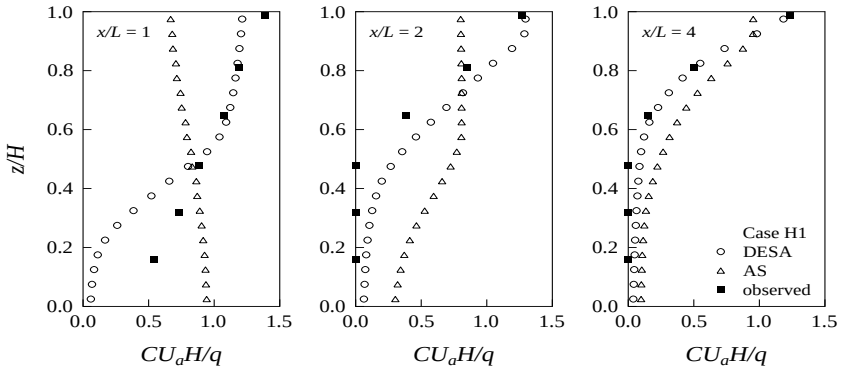

Figure 5.11: Normalized vertical profiles of tracer concentration (C) along centreline for perpendicular flow alignment, for $F = 1.26$ (Case H1 in Roberts 1977).

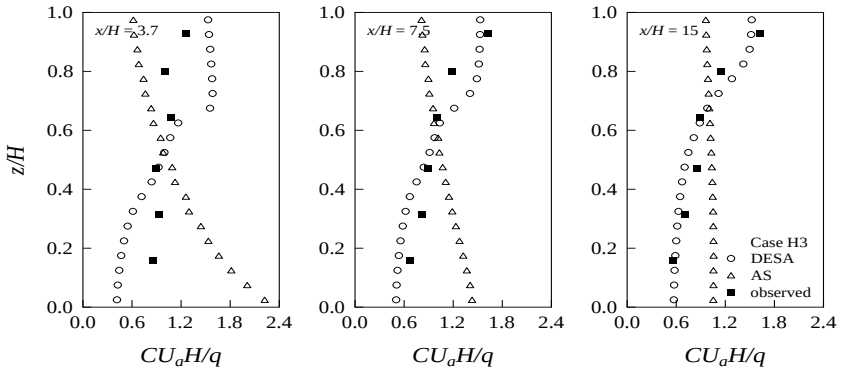

Figure 5.12: Normalized vertical profiles of tracer concentration (C) along centreline for perpendicular flow alignment, for $F = 11.8$ (Case H3 in Roberts 1977).

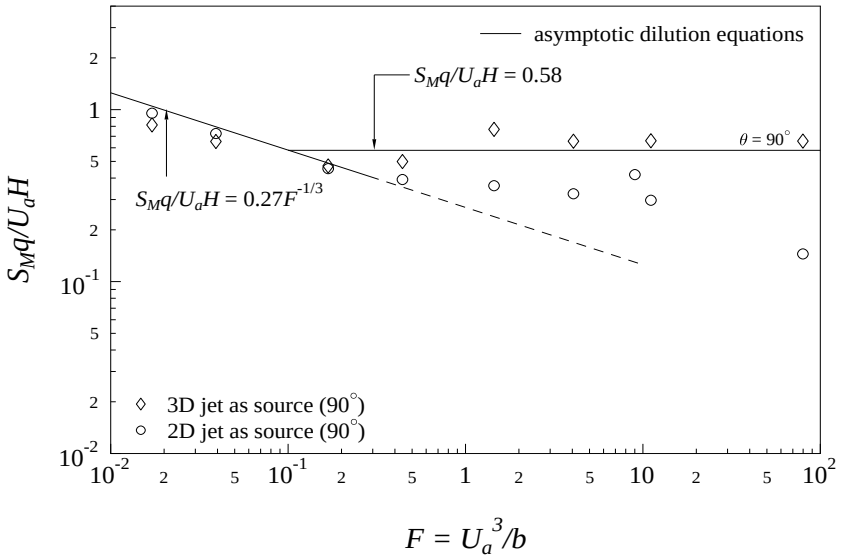

Figure 5.13: Computed minimum surface dilution as a function of crossflow Froude number F (symbols with source representation method indicated). Best fit of experimental data shown as asymptotic dilution equation (solid line).

5.2 Line plume in stratified crossflow

Roberts *et al.* (1989a) conducted experiments in a stratified towing tank 1.2 m deep, 2.4 m wide and 25.0 m long. A constant linear stratification with nominal buoyancy frequency, $N = \left(-\frac{g}{\rho_a}\frac{d\rho}{dz}\right)^{1/2}$, of 0.3 $sec.^{-1}$ and a 1.2 m long multi-port diffuser were used in all experiments. For this case, a 41 x 8 x 20 model grid with open boundaries at two ends, a horizontal grid size of 60.0 cm by 30.0 cm and 20 uniform vertical layers is employed. The model is run to generate a steady state current field first before the line plume is applied and the time step used is 0.025 sec. (with $Cr \approx 0.29$).

Fig. 5.14 shows the normalised vertical profiles of the tracer concentration on the centreline, it can seen that the simulated plumes by AS method are trapped in a lower level than that by the DESA method. The predicted level of minimum dilution and minimum dilution (maximum concentration in spreading layer) are shown in Fig. 5.17 and Fig. 5.17. The calculations show that the AS method predicts exaggerated mixing, and hence a much lower trapping level than that predicted by the DESA method. For the cases with $F = {U_a}^3/b \geq 1$, the simulated plumes (by AS) remain in more or less the same level. Fig. 5.15 and Fig. 5.16 show several vertical sections parallel to the line diffuser downstream of the discharge point for $F = 0.1$. It can be seen that besides the plume predicted by DESA is trapped in a higher level than that by AS, the spreading layer is thinner and wider.

Roberts *et al.* (1989a) reported for $F = 0.1$, the rise height (the level of minimum dilution), z_m, is about $2l'_b$ and followed an $F^{1/6}$ power law for $F \geq 5$ given by:

$$\frac{z_m}{l'_b} = 1.5F^{-1/6} \tag{4.1}$$

where $l'_b = b_o^{1/3}/N$. A semi-empirical equation is also obtained for the minimum dilution at the trapped level for the range $0.1 < F < 100$:

$$\frac{S_m q N}{b_o^{2/3}} = 2.19F^{1/6} - 0.52 \tag{4.2}$$

As shown in Fig. 5.17, the DESA predicted minimum dilution and rise height (level of minimum dilution) agree well with the experimental best-fit (Eqn. 4.1 and 4.2) even for smaller F down to about 0.1. It can also be seen that the AS method over-predicts the dilution and hence underpredicts the trap level, especially for smaller F (Fig. 5.18). Additional analysis (not shown) also reveal that the DESA predicted plume width as a function of distance downstream is in good agreement with the observations (Roberts *et al.* 1989b).

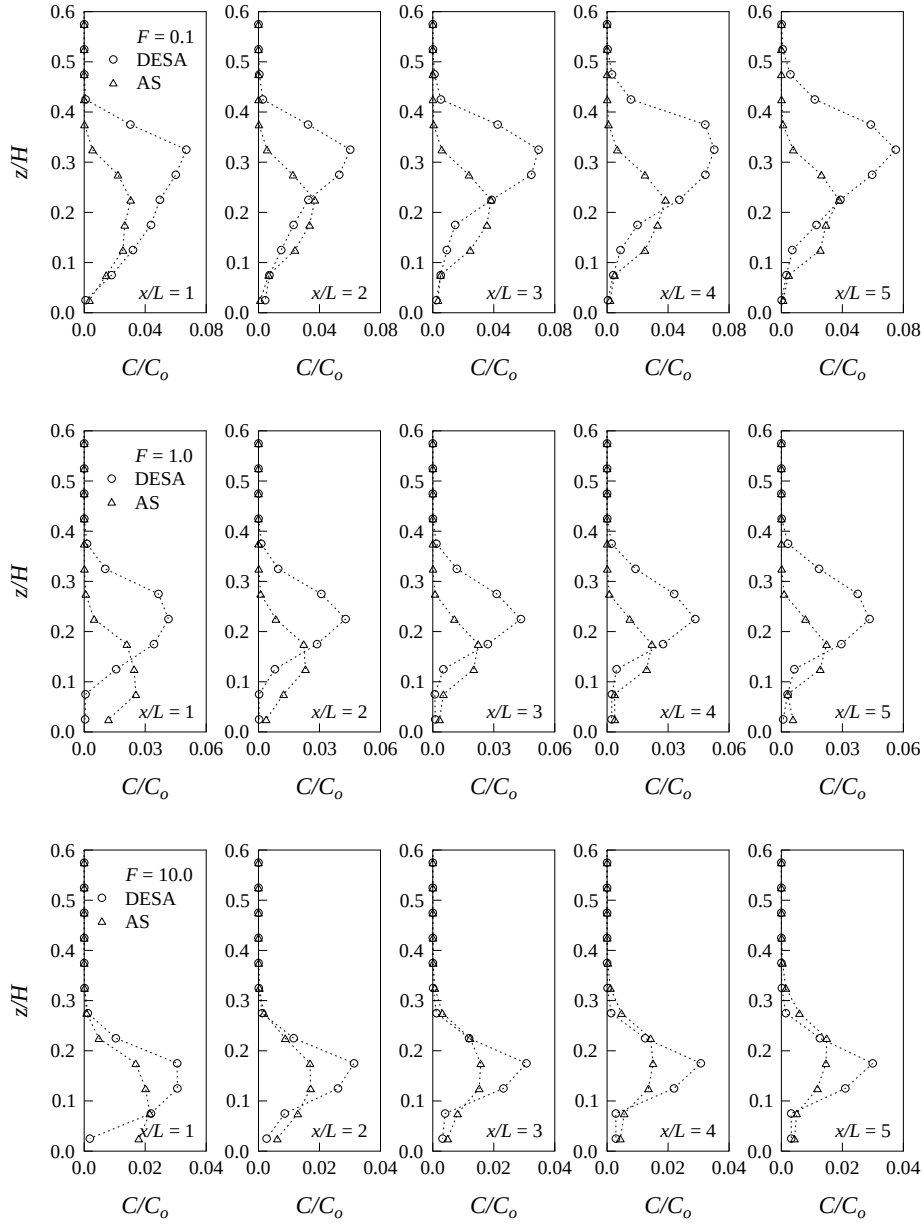

Figure 5.14: Normalized vertical profiles of tracer concentration, C, on the centreline for line plume in stratified crossflow.

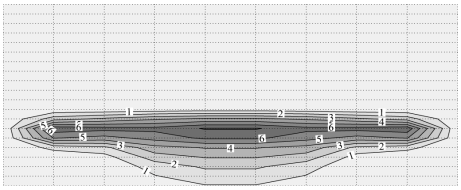

a) $x = L$

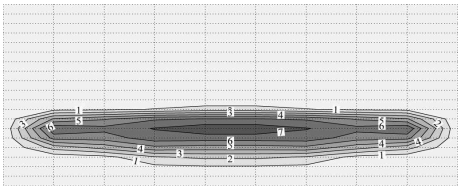

b) $x = 3L$

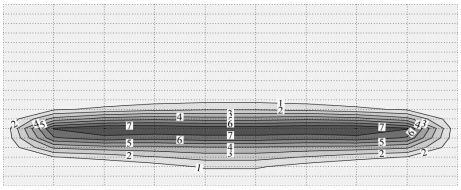

c) $x = 5L$

Figure 5.15: Computed tracer concentration field for vertical sections parallel to the line source in a perpendicular stratified crossflow for $F = 0.1$ using DESA (concentration in $0.01C_o$).

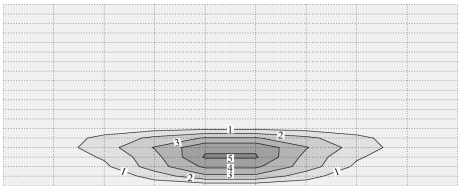

a) $x = L$

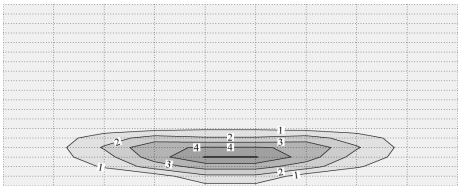

b) $x = 3L$

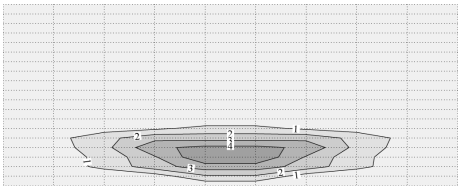

c) $x = 5L$

Figure 5.16: Computed tracer concentration field for vertical sections parallel to the line source in a perpendicular stratified crossflow for $F = 0.1$ using AS (concentration in $0.01C_o$).

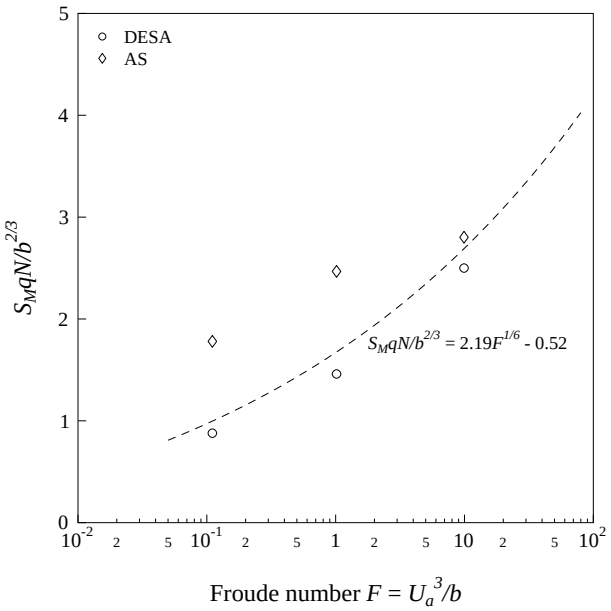

Figure 5.17: Predicted minimum dilution at trapping level (symbols) for line plume in stratified crossflow.

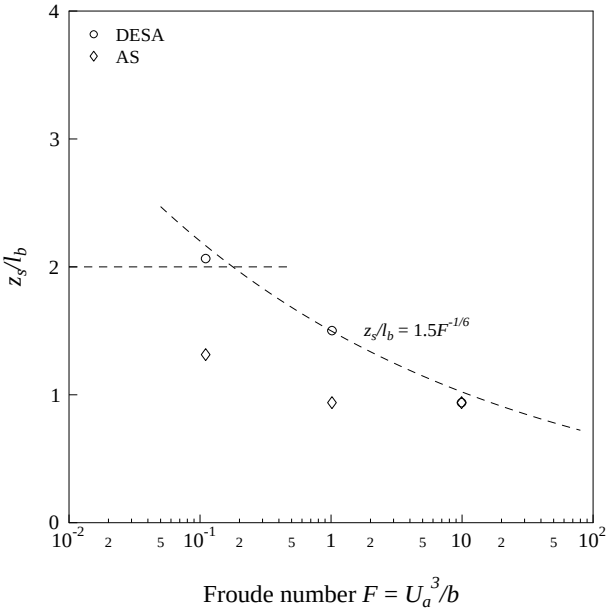

Figure 5.18: Predicted level of minimum dilution (symbols) for line plume in stratified crossflow.

5.3 Round jet in uniform crossflow

A field example of round jet in crossflow is described in Akar and Jirka (1994). The Orange County Outfall of South California discharges a sewage flow of 5.26 m^3/s through a single submerged vertical port of diameter 1.98 m. The ambient water is 16.8 m deep and has a current velocity of about 0.175 m/s. There is no ambient stratification and the discharge can be assumed to be fresh water. A model grid with open boundaries at two ends, a horizontal grid size of 48 m ($\sim 2.9d$) by 48 m and 20 uniform vertical layers is employed. As shown in Fig. 5.19, with an ambient current of 0.178 m/s, the computed surface plume is wider than the observed one. By increasing the ambient current to 0.256 m/s, the computed surface plume can be made to agree much better with the observed one (Fig. 5.20). Assuming that wind induced current is about 3% of the wind speed, this surface current corresponds to a wind speed of 2.6 m/s, which is however much smaller than the average wind speed 7.1 m/s for that site. Similar to the case for round jet in stagnant water, a very thin surface layer (about $0.1H$) is formed (Fig. 5.21) which is quite similar to that CORMIX predictions given in Fig. 9 of Akar and Jirka (1994) for wind speed equal to zero or 7 m/s.

As there is no quantitative information for the case of Orange County sewage outfall in

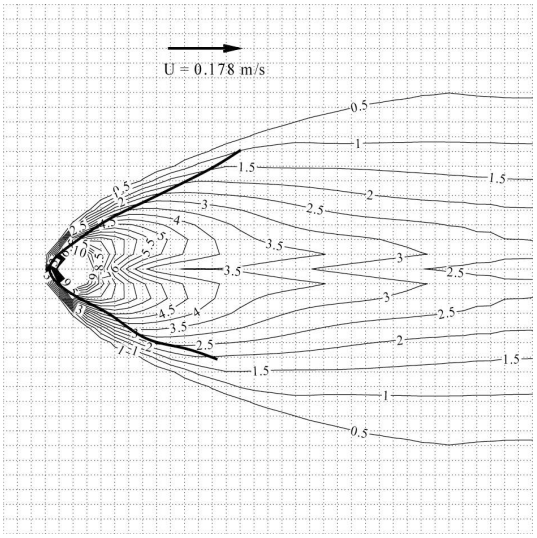

Figure 5.19: Computed of computed surface plume with field observation, Orange County Outfall, $U_a = 0.178$ m/s.

the vertical direction for comparison, we have performed a laboratory experiment of a vertical round buoyant jet in a crossflow in a laboratory flume, at a densimetric Froude model scale of about 1:198. The discharge port has a diameter of 1 cm and discharges a flow of 9.54 cm^3/s. The ambient water is 8.5 cm deep and has a current velocity of about 1.6 cm/s. There is no ambient stratification and the discharge can be assumed to be fresh water. A model grid with open boundaries at two ends, a horizontal grid size of 6.4 cm ($\sim 1.3d$) by 6.4 cm and 20 uniform vertical layers is employed. A step time size used is 0.2 sec ($Cr \approx 2.85$). As shown in Fig. 5.22, the predicted vertical concentration profiles agree well with the observations beyond a distance of around $2H$ from the discharge point.

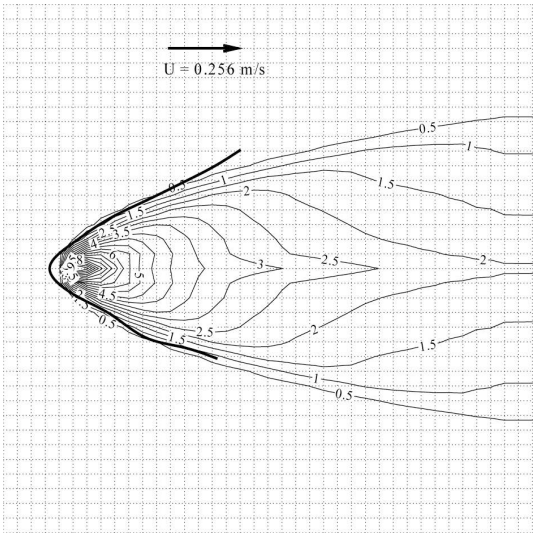

Figure 5.20: Comparison of computed surface plume with field observation, Orange County Outfall, $U_a = 0.256$ m/s.

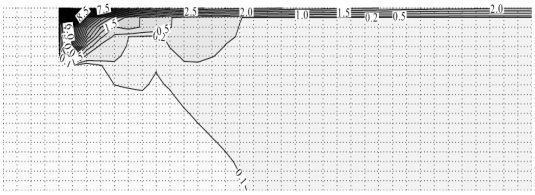

Figure 5.21: Section view of computed plume, Orange County Outfall, $U_a = 0.256$ m/s.

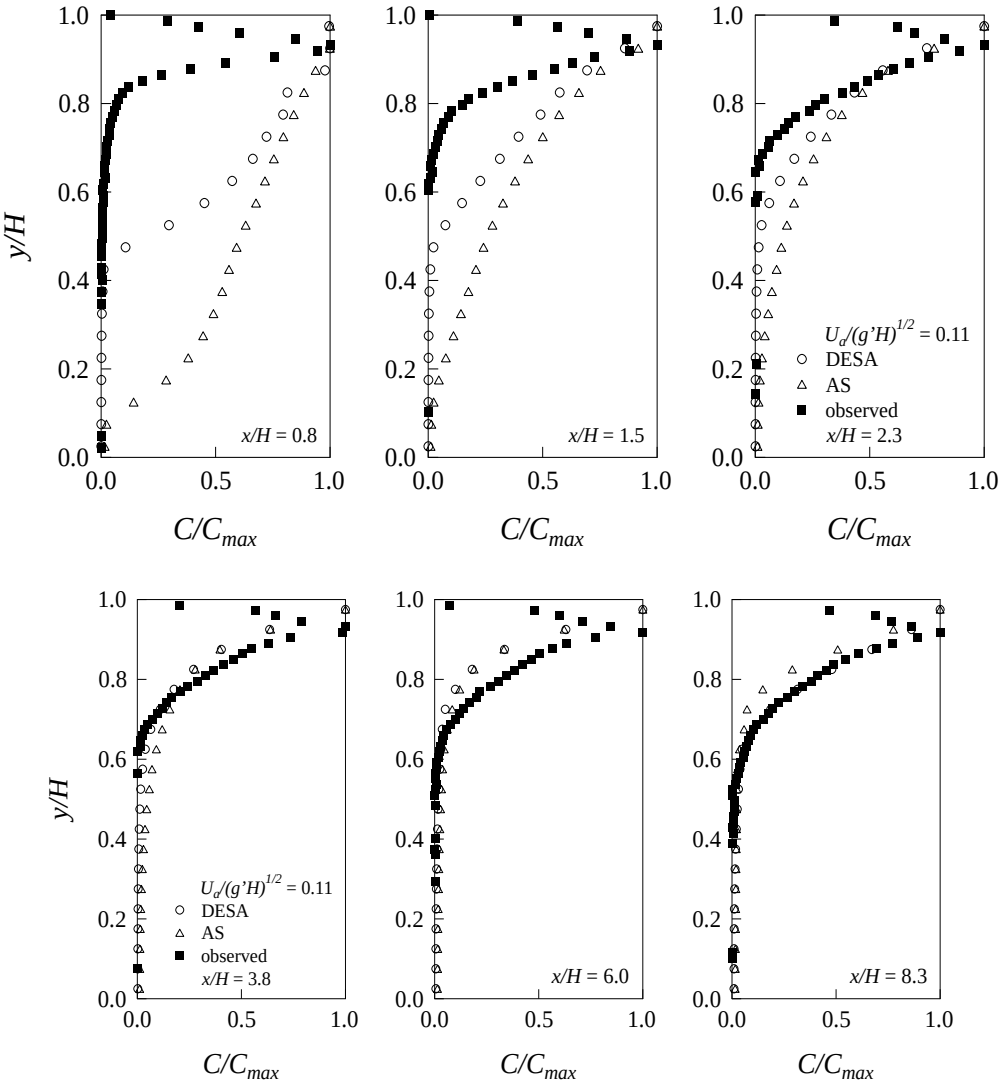

Figure 5.22: Normalized vertical profiles of effluent concentration, C, on centreline for a round plume in current flow with $U_a/(g'H)^{1/2} = 0.11$

Chapter 6

Far Field Model Grid and Source Representation

6.1 Introduction

A series of sensitivity tests has been carried out to assess the effects of model grid sizes, model parameters and source representations upon the DESA model predictions.

6.2 Smargorinsky constant

As described in Section 1.3, the horizontal diffusion in the far field EFDC model is represented by the Smagorinsky diffusivity. A constant coefficient C is a dimensionless number and has found to work well in the range, 0.10 to 0.20 for the far field modelling applications. As shown in Fig. 6.1 and 6.2, the model results are not sensitive to the changes in the value of C within this usual range. Hence, the selection of the value for C can be based on the far field model calibration independent of DESA.

6.3 Time step

Fig. 6.3 and 6.4 show that the convergence of the model results with different time steps. From the model tests that have been carried out, it is found the model works well with $Cr = \sqrt{gH}\Delta t/\Delta x$ around 4.0 or less and $U\Delta t/\Delta x$ less than 1.0. We note these stability constraints also apply to the far field flow simulation with EFDC which models the advection terms explicitly.

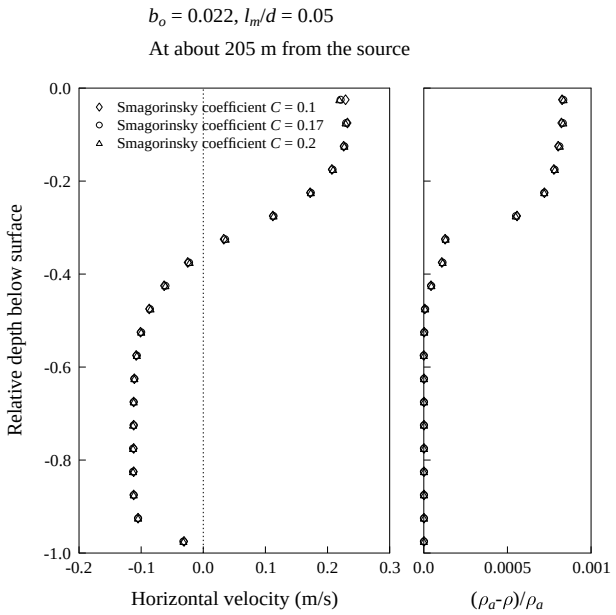

Figure 6.1: Velocity and density deficit profiles across the spreading layer generated by a plane vertical buoyant jet into stagnant uniform water with different horizontal diffusivities.

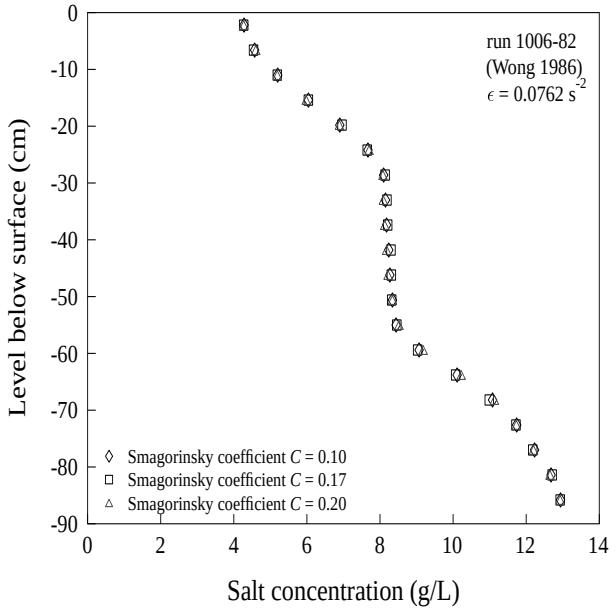

Figure 6.2: Ambient density profiles before and after a slot "plume-like" discharge into a linearly stratified fluid with different horizontal diffusitivites.

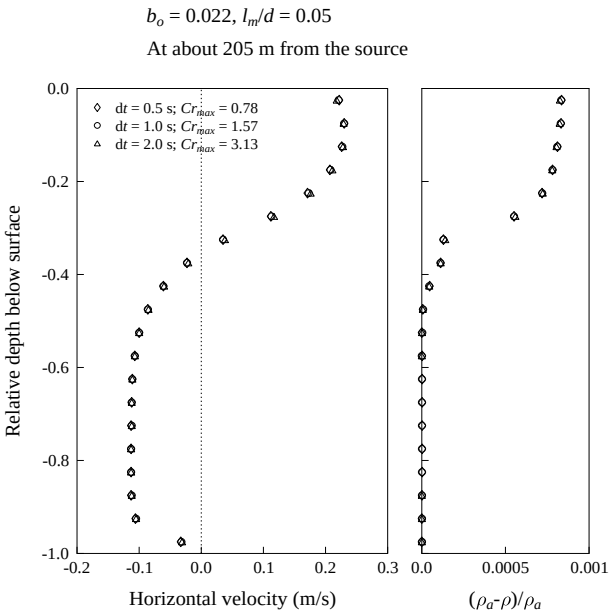

Figure 6.3: Velocity and density deficit profiles across the spreading layer generated by a plane vertical buoyant jet into stagnant uniform water with different time steps.

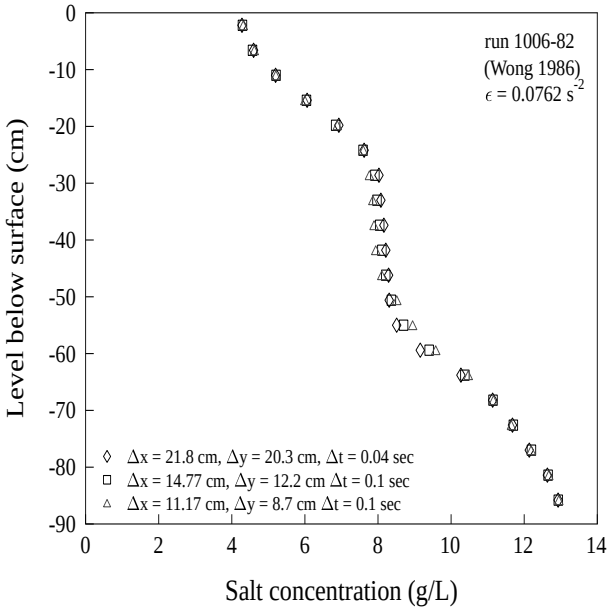

Figure 6.4: Ambient salinity profiles before and after a vertical round buoyant jet in stagnant linearly density-stratified ambient fluid with different time steps and model grid sizes.

6.4 Horizontal grid

The main purpose of the new coupling method is to represent the near field jet entrainment effects of the environmental discharges in the far field model. As such the DESA method is not intended to model the details of the buoyant jet mixing. The horizontal grid size should be large enough to embed the whole horizontal projection of the plume elements at the terminal level of the jet. Of course, in the vicinity of the discharge, the grid size should be small enough to provide the necessary resolution for simulating the intermediate field effects.

Both Fig. 6.4 and 6.5 show the result of sensitivity tests carried out with different far field model grid sizes, and very close results are obtained from all cases except for the case with 10 vertical layers, probably due to the insufficient vertical resolution (see next section).

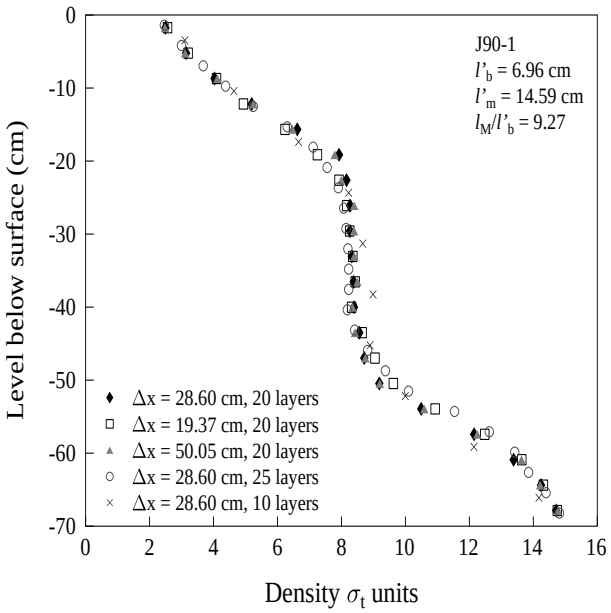

Figure 6.5: Ambient density profiles before and after a slot "plume-like" discharge into a linearly stratified fluid with different far field model grid sizes.

Fig. 6.6 shows the comparison between the results obtained from a uniform grid ($\Delta x = 50$ m) to a non-uniform grid with grid refinement (Δx varies from 10 m to 50 m) around the discharge point (Fig. 4.2). It can be seen that results from the two grids are very similar at a distance not too far from the discharge point (about $8H$ from the source).

6.5 Vertical discretization

For smaller vertical grid size, we will have smaller entrainment sinks at each grid cell (as less number of plume elements are included in each cell) and a larger diluted flow source up to the full predicted diluted flow (as less entrainment flow being reduced from the source). The greater difference (or gradient) between the source and sink terms will cause greater vertical flows in the water column containing the discharge point, and leads to mixing between more vertical layers. As shown in Fig. 6.7, the vertical profiles are very similar with 10, 20 and 40 uniform

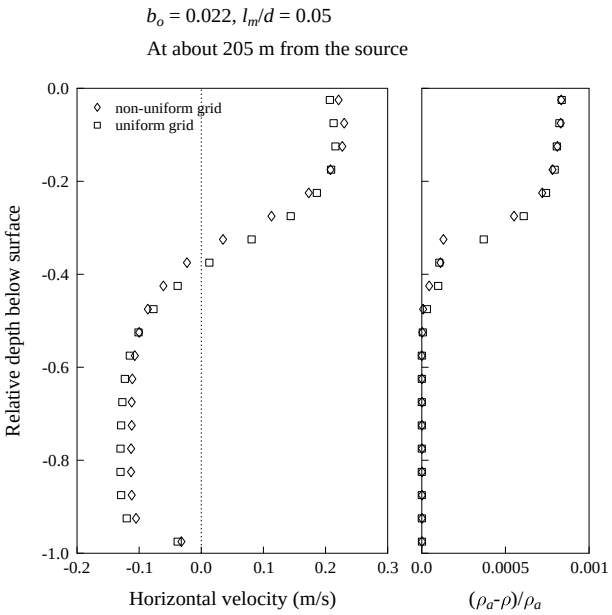

Figure 6.6: Velocity and density deficit profiles across the spreading layer generated by a plane vertical buoyant jet into stagnant uniform water with different model grids.

vertical layers. Both Fig. 6.5 and 6.7 indicates that the time-varying location of the sources and sinks due to the dynamic interaction between the near and far field models, and the vertical mixing induced by the source/sink terms can compensate for the effects of different vertical discretisation. In the next section, further examination on alternative source representation is conducted.

6.6 Source representation

The near field model JETLAG treats individual 3D round jets and does not consider the reduction in entrainment due to the merging or interacting of the jets. Hence a plane (slot) buoyant jet has to be represented by a number of equivalent non-interfering round buoyant jets (preserving the same volume, momentum, and buoyancy fluxes per unit diffuser length). To assess the performance of such source representation, alternative 2D integral plane jet models are also used as the near field model and dynamically coupled with the 3D far field model by the DESA method. As shown in Fig. 6.8, the results obtained from models using JETLAG and PLANEJET (with varying entrainment coefficient) are very close, and those from the plane plume model with constant entrainment coefficient are slightly different from the other two.

For vertical discharges, besides the *single source* (SS) approach, two alternative ways of representing the source by distributing the diluted flow into multiple vertical layers are possible. First, in the *Binomial Distributed Sources* (BDS) method, the source can be distributed around the terminal level within one visual plume diameter based on binomial distribution. This is similar to the approach adopted for the inclined plume elements that cut through more than one vertical layers. However, instead of spanning just across the vertical projection of the plume element, the sources span through the whole visual diameter of the plume element. Second, in the *Uniform Distributed Sources* (UDS) method, the source is distributed below the terminal

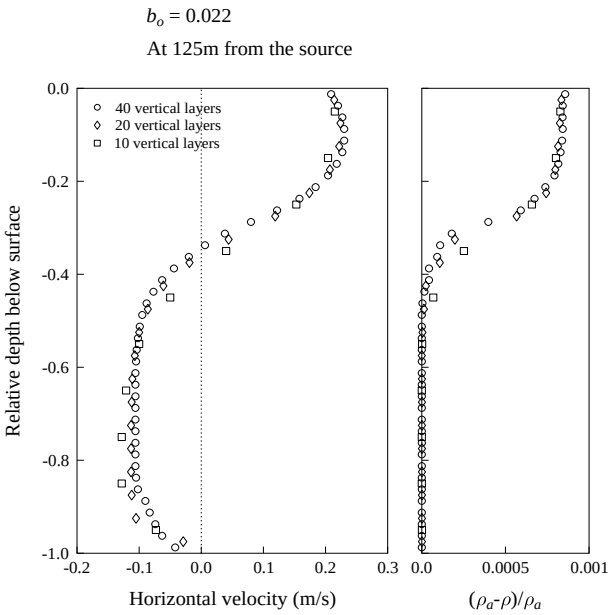

Figure 6.7: Velocity and density deficit profiles across the spreading layer generated by a plane vertical buoyant jet into stagnant uniform water with different number of vertical layers.

level (or above for negative buoyancy) within one visual plume radius based on uniform distribution. Fig. 6.9 shows a computation of a plane vertical buoyant jet in uniform water using the three methods. It is observed that the results from all three methods are very similar; only that from UDS is slightly different.

In general, our tests indicate that both SS and BDS are feasible methods for source representation; the results obtained from using either approach are not significantly different. However, artificial and arbitrary re-distributing the diluted flow sometimes may reduce the vertical transport and mixing, resulting in incorrect representation of the active mixing.

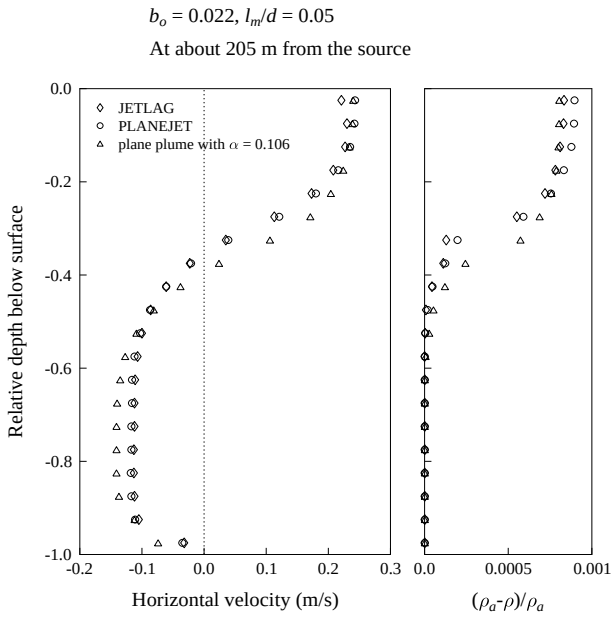

Figure 6.8: Velocity and density deficit profiles across the spreading layer generated by a plane vertical buoyant jet into stagnant uniform water with different near field models.

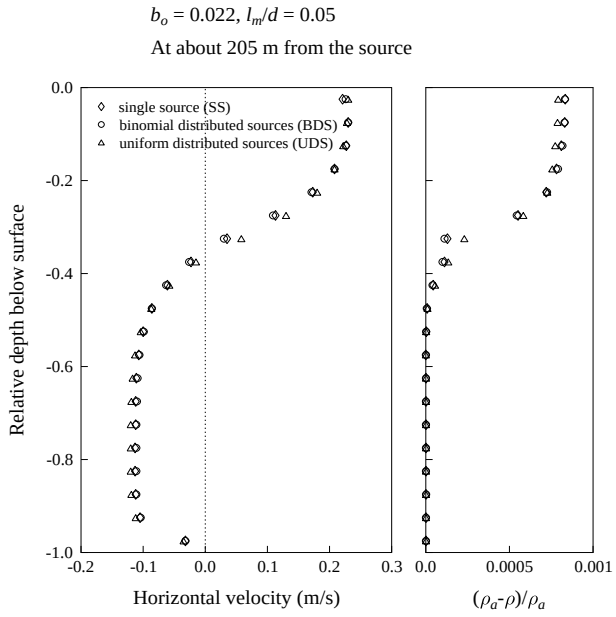

Figure 6.9: Velocity and density deficit profiles across the spreading layer generated by a plane vertical buoyant jet into stagnant uniform water with different source representation.

Chapter 7

Summary

In this report we have outlined a new method to compute mixing and transport in the intermediate field. The method, Distributed Entrainment Sink Approach (DESA), simulates the action of the jet mixing in the near field within a 3D shallow water circulation model. Genuine dynamic coupling of the near and far field models is achieved at grid cell level. The DESA method has been applied to a wide variety of complex mixing and transport problems - ranging from 2D to 3D buoyancy or momentum-dominated jets with positive or negative buoyancy, in uniform or stratified fluid, and in stagnant or flowing ambient. As with many practical problems, many of these test cases involve a close coupling of the jet flow and the spreading layer in the intermediate field. The method has been demonstrated to give mixing predictions that are well supported by basic laboratory experimental data.

The findings from the extensive test cases described can be summarized as follows:

1. The simulation results confirm that the DESA method is able to give satisfactory predictions of mixing and transport due to an effluent discharge in the intermediate field - in terms of the dilution, changes in the ambient conditions and buoyant spreading characteristics.

2. The following model implementation guidelines are suggested for DESA:

   - In general, a horizontal grid size between $0.4H$ and $3.0H$, where H is the water depth, is suitable for near and intermediate field region. Such a grid size will contain the entire plume element even in the terminal level for the near field simulation. These sizes are similar to or greater than those for the "source only" methods which need to be small enough to prevent excessive over-estimate of the initial dilution.
   - In the vertical direction, 15 to 20 layers is found adequate for resolving the vertical structure.
   - Due to the dynamic interaction between the discharge and the ambient flow field, the required time step may be smaller than that for the pure field flow simulation without the discharge. With the semi-implicit EFDC scheme, time step with $Cr = \sqrt{gH}\Delta t/\Delta x$ around 4.0 or less and $U\Delta t/\Delta x$ less than 1.0 is required. For cases with source and sink terms introduced to multiple neighbouring water columns such as line plumes in cross-flow, a smaller time step may be required to ensure that $w\Delta t/\Delta z \leq 1$ (w = vertical velocity).
   - As it will take a time T_r for the jet to rise to the terminal level, the corresponding entrainment sinks and diluted sources should remain the same during that period

of time. From the numerical experiments, it is found that it is feasible to use the same source/sink terms up to $5T_r$. Therefore, instead of updating the source/sink terms for every far field time step, the near field computation can be carried out every $[5T_r/\Delta t] + 1$ steps.

- It is found that line (2D) sources can be well-represented by an array of equivalent non-interfering round buoyant sources.

3. The DESA method has been shown to perform better than alternative near-far field coupling methods such as the Actual Source (AS) method for a wide variety of problems. All the coupling methods hitherto reported in the literature are essentially "one-way" coupling methods, without a dynamic linkage of the near field and far field model computations. Hence the mixing characteristics in the intermediate field cannot be simulated. These include changes in source-induced ambient stratification and trap level of a line plume in stratified crossflow. In some cases, e.g. dense jets, the near field details (e.g. jet orientation) can result in very different mixing behavior in the intermediate field. All these important features cannot be simulated by alternative previous coupling methods.

4. The entrainment sinks and dilution sources represent the action of the jet entrainment in the far field. They are not intended to model the detailed turbulent jet mixing in the near field. The source and sink terms may induce a local vertical circulation, which is not physically realistic, in the immediate neighbourhood of the cells containing the discharge point. This is related to the fact that vertical jet momentum effects due to the discharge are not represented in the far field model (by virtue of the hydrostatic approximation). However, the numerical experiments show that this region typically does not extend more than one grid cell on either side of the discharge point.

5. The DESA method is found to work well for buoyant discharges in a wide variety of applications. For problems where jet momentum plays an important role (e.g. jet stability), a full 3D solution of the Reynolds Averaged Navier-Stokes (RANS) equations would be required (see e.g. Kuang and Lee 2006).

Bibliography

[1] Akar, P.J. and Jirka, G.H., (1994). "Buoyant spreading processes in pollutant transport and mixing", *Journal of Hydraulic Research*, Vol. 32, No. 6, pp. 815-831.

[2] Baines, W.D. and Turner, J.S., (1969). "Turbulent buoyant convection from a source in a confined region", *Journal of Fluid Mechanics*, Vol. 37, Part 1, pp. 51-80.

[3] Bühler, J., (1986). Discussion of "Spreading layer of two-dimensional buoyant jet" by R.B. Wallace and S.J. Wright, *Journal of Hydraulic Engineering*, ASCE, Vol. 112, No. 10, pp. 992-994.

[4] Chen, J.C., (1980). *Studies on gravitational spreading currents*. W.M. Keck Laboratory of Hydraulics and Water Resources, Report KH-R-40, California Institute of Technology, Pasadena, Calif., USA.

[5] Choi, K.W. and Lee, J.H.W., (2005). "A new approach to effluent plume modelling in the intermediate field", *Proc. 31st IAHR Congress*, Seoul, Korea, September 11-16, pp. 4303-4311.

[6] Choi, K.W. and Lee, J.H.W., (2007). "Distributed entrainment sink approach for modelling mixing and transport in the intermediate field", *Journal of Hydraulic Engineering*, ASCE, Vol.133, No.7, pp.804-815.

[7] Hamrick, J.M., (1992). *A Three-dimensional Environmental Fluid Dynamics Computer Code: Theoretical and Computational Aspects*, The College of William and Mary, Virginia Institute of Marine Science, Special Report 317, Virginia, USA.

[8] Hamrick, J.M., (1996). *Users Manual for the Environmental Fluid Dynamics Computer Code: Theoretical and Computational Aspects*, The College of William and Mary, Virginia Institute of Marine Science, Special Report 331, Virginia, USA.

[9] Jirka, G.H. and Harleman, D.R.F. (1979). "Stability and mixing of a vertical plane buoyant jet in confined depth". *Journal of Fluid Mechanics*, Vol. 94, No. 9, pp. 275-304.

[10] Jirka, G.H. and Lee, J.H.W., (1994). "Waste disposal in the ocean", in *Water Quality and its Control*, *IAHR Design Guide for Hydraulic Structures*, Balkema, pp. 193-242.

[11] Koh, R.C.Y., (1983). "Wastewater field thickness and initial dilution", *Journal of Hydraulic Engineering*, ASCE, Vol. 109, No. 9, pp. 1232-1240.

[12] Kuang, C.P. and Lee, J.H.W., (2006). "Stability and mixing of a vertical axi-symmetric buoyant jet in shallow depth" , *Environmental Fluid Mechanics*, Vol.6, pp.153-180.

[13] Lee, J.H.W. and Cheung, V., (1986). "Inclined plane buoyant jet in stratified fluid". *Journal of Hydraulic Engineering*, ASCE, Vol. 112, No. 7, pp. 580-589.

[14] Lee, J.H.W. and Cheung, V., (1990). "Generalized Lagrangian model for buoyant jets in current", *Journal of Environmental Engineering*, ASCE, Vol. 116, No. 6, pp. 1085-1105.

[15] Lee, J.H.W. and Chu, V., (2003). *Turbulent Jets and Plumes V A Lagrangian Approach*. Kluwer Academic Publishers.

[16] Lee, J.H.W. and Jirka, G.H., (1981). "Vertical round buoyant jet in shallow water". *Journal of Hydraulic Engineering*, ASCE, Vol. 107, No. HY12, pp. 1651-1675.

[17] Mellor, G. L. and Yamada, T., (1982). "Development of a turbulence closure model for geophysical fluid problems", *Reviews of Geophysics and Space Physics*, Vol. 20, No. 4, pp. 851-875.

[18] Roberts, P.J.W., (1977). *Dispersion of buoyant waste water discharged from outfall diffusers of finite length*. W.M. Keck Laboratory of Hydraulics and Water Resources, Report KH-R-35, California Institute of Technology, Pasadena, Calif., USA.

[19] Roberts, P.J.W., (1979). "Line plume and ocean outfall dispersion". *Journal of Hydraulic Engineering*, ASCE, Vol. 105, No. 4, pp. 313-331.

[20] Roberts, P.J.W., Ferrier, A. and Daviero, G. (1997). "Mixing in inclined dense jets". *Journal of Hydraulic Engineering*, ASCE, Vol. 123, No. 8, pp. 693-699.

[21] Roberts, P.J.W., Snyder, W.H. and Baumgartner, D.J. (1989a). "Ocean outfalls, I: submerged wastefield formation". *Journal of Hydraulic Engineering*, ASCE, Vol. 115, No. 1, pp. 1-25.

[22] Roberts, P.J.W., Snyder, W.H. and Baumgartner, D.J. (1989b). "Ocean outfalls, II: spatial evolution of submerged wastefield". *Journal of Hydraulic Engineering*, ASCE, Vol. 115, No. 1, pp. 26-48.

[23] Roberts, P.J.W. and Toms, G. (1986). "Inclined dense jets in flowing current". *Journal of Hydraulic Engineering*, ASCE, Vol. 113, No. 3, pp. 323-341.

[24] Turner, J.S., (1973). *Buoyancy Effects in Fluids*, Cambridge University Press.

[25] Wallace, R.B. and Wright, S.J., (1984), "Spreading layer of two-dimensional buoyant jet", *Journal of Hydraulic Engineering*, ASCE, Vol. 110, No. 6, pp. 813-828.

[26] Wong, D.R., (1986). *Buoyant Jet Entrainment in Stratified Fluids*. Report No. UMCE 85-9, The University of Michigan, Michigan, USA.

[27] Wright, S.J., (1985). Discussion of "Wastewater field thickness and initial dilution", *Journal of Hydraulic Engineering*, ASCE, Vol. 111, No. 5, pp. 891-896.

[28] Wright, S.J., Roberts, P.J.W., Yan, Z.M. and Bradley, N.E., (1991), "Surface dilution of round submerged buoyant jets", *Journal of Hydraulic Research*, Vol. 29, pp. 67-89.

[29] Zhang, X.Y. and Adams, E.E., (1999). "Prediction of near field plume characteristics using far field circulation model", *Journal of Hydraulic Engineering*, ASCE, Vol. 125, No. 3, pp. 233-241.